University of Massachusetts Amherst
ScholarWorks@UMass Amherst

Doctoral Dissertations Dissertations and Theses

November 2016

Dynamic Wetting and Drag Reduction on Superhydrophobic and Liquid-Infused Surfaces

Jeong-Hyun Kim
University of Massachusetts - Amherst

Follow this and additional works at: https://scholarworks.umass.edu/dissertations_2

Part of the Other Mechanical Engineering Commons

Recommended Citation

Kim, Jeong-Hyun, "Dynamic Wetting and Drag Reduction on Superhydrophobic and Liquid-Infused Surfaces" (2016). *Doctoral Dissertations*. 724.
https://scholarworks.umass.edu/dissertations_2/724

This Open Access Dissertation is brought to you for free and open access by the Dissertations and Theses at ScholarWorks@UMass Amherst. It has been accepted for inclusion in Doctoral Dissertations by an authorized administrator of ScholarWorks@UMass Amherst. For more information, please contact scholarworks@library.umass.edu.

DYNAMIC WETTING AND DRAG REDUCTION ON SUPERHYDROPHOBIC AND LIQUID-INFUSED SURFACES

A Dissertation Presented

by

JEONG-HYUN KIM

Submitted to the Graduate School of the
University of Massachusetts Amherst in partial fulfillment
of the requirements for the degree of

DOCTOR OF PHILOSOPHY

SEPTEMBER 2016

Mechanical and Industrial Engineering

© Copyright by Jeong-Hyun Kim 2016

All rights reserved

DYNAMIC WETTING AND DRAG REDUCTION ON SUPERHYDROPHOBIC AND LIQUID-INFUSED SURFACES

A Dissertation Presented

by

JEONG-HYUN KIM

Approved as to style and content by:

Jonathan P. Rothstein, Chair

Yahya Modarres-Sadeghi, Member

Alfred Crosby, Member

Sundar Krishnamurty, Department Head
Mechanical and Industrial Engineering

ACKNOWLEDGEMENTS

I would like to thank Professor Jonathan P. Rothstein, for his guidance and assistance. He was always more than willing to help me set up the experiments and analyze the results with his witty jokes. He has spent a tremendous time and efforts on our papers as well. I would also like to thank Professor Yahya Modarres-Sadeghi and Professor Alfred Crosby for their comments and service as my committee members. Thanks to my lab members- Sunil, Anita, Sam, Zahra, Trenton, Theo, Dong, Robert, and Mike. Personally, I would like to thank to my friends in Amherst- JooHee, Minjung, Insung, Jakeun, Hyunkyu, Sangsoo, and Semyung. Also, I send special huge thanks to my wife Young-Ju, who I met and married my PhD years. She has provided me with genuine care and unlimited support both linguistically and emotionally. We are expecting our first baby this January 2017. Finally, thanks to my parents and older sister for their love and dedicated support from Korea.

ABSTRACT

DYNAMIC WETTING AND DRAG REDUCTION ON SUPERHYDROPHOBIC AND LIQUID-INFUSED SURFACES

SEPTEMBER 2016

JEONG-HYUN KIM

B.E.M.E., YEUNGNAM UNIVERSITY

M.S.M.E., YEUNGNAM UNIVERSITY

PH.D., UNIVERSITY OF MASSACHUSETTS AMHERST

Directed by: Professor Jonathan P. Rothstein

Reducing drag in fluid flow has been one of the most widely studied topics in fluid dynamics due to the significant impact on improving operational efficiencies and cutting cost in applications from the aerospace, automotive and naval industries. Over the past two decades, superhydrophobic surfaces have been in the spotlight due to their ability to reduce frictional drag on the wall surface in both laminar and turbulent flows. Despite the extensive work on superhydrophobic surfaces, there are still a number of open questions remaining. In this dissertation, we investigate how a moving contact line interacts with a superhydrophobic surface by performing the first dynamic contact angle measurements to better understand the dynamics of droplets and streams on the surfaces. Our measurements found that the dynamic advancing contact angles on a superhydrophobic surface remains constant independent on capillary number while the dynamic receding contact angles decreases with capillary number but at a rate much slower than on a smooth surface. Furthermore, we investigated the role of the air-water interface shapes on the drag reduction. A novel microfluidic device was designed to incorporate superhydrophobic pillars. The shape of the air-water interface was changed with change to the static pressure in the channel. Slip along interface trapped within the superhydrophobic surface was found to result in significant drag reduction. However, the changes in flow geometry due to changes in bubble shape dominated effects due to slip. Reducing the bubble size amplified drag reduction, while increasing bubble size reduced drag reduction and even resulted in drag enhancement.

In this dissertation, we also studies liquid-infused superhydrophobic surfaces as an alternative to the air-infused superhydrophobic surfaces. In the studies presented here, various immiscible oils were infused into the structures of precisely patterned and randomly rough superhydrophobic surfaces. A series of experiments were performed to investigate how liquid-infused surface affect drag reduction and droplet impact dynamics. The pressure drop reduction and slip length on the liquid-infused surfaces in microchannels were found to increase as the ratio between viscosity of water and the infused oil was increased. The longevity of these surfaces was also studied with the most effective surface found to be randomly rough. The effect of the viscosity ratio was also investigated on the droplet impact dynamics onto liquid-infused superhydrophobic surfaces. The increase in the viscosity ratio was found to increase a maximum diameter and a spreading/retraction rates of droplets. Taken together, the experimental research presented in this dissertation have allowed us to better understand and optimize the design of air-infused and liquid-infused superhydrophobic surfaces for drag reduction, droplet spreading and liquid mobility. With this new-found knowledge, a sense of new innovative ideas and applications has been or soon will be realized.

TABLE OF CONTENTS

Page

ACKNOWLEDGEMENTS iv

ABSTRACT v

LIST OF FIGURES ix

CHAPTER

1. INTRODUCTION 1

    1.1 Wettability of Surfaces 1
    1.2 Superhydrophobic Surfaces 5

        1.2.1 Fabrication of Superhydrophobic Surfaces 7
        1.2.2 Engineering Application in Drag Reduction 11

    1.3 Motivation 14
    1.4 Dissertation Outline 16

2. DYNAMIC CONTACT ANGLE MEASUREMENTS ON SUPERHYDROPHOBIC SURFACES 17

    2.1 Introduction 17
    2.2 Experimental Setup 22
    2.3 Results and Discussion 29
    2.4 Conclusions 41

3. DYNAMIC CONTACT ANGLE MEASUREMENTS OF VISCOELASTIC FLUIDS 44

    3.1 Introduction 44
    3.2 Experimental Setup 48

        3.2.1 Materials 48
        3.2.2 Dynamic Contact Angle Measurements 53

    3.3 Results and Discussion 55

        3.3.1 Dynamic Contact Angle Measurements 55
        3.3.2 Viscoelastic Scaling Analysis 69

3.4 Conclusions 74

4. ROLE OF INTERFACE SHAPE ON THE LAMINAR FLOW THROUGH AN ARRAY OF SUPERHYDROPHOBIC PILLARS 76

4.1 Introduction 76
4.2 Experimental Setup 79
4.3 Results and Discussion..85
4.4 Conclusions 101

5. DRAG REDUCTION ON LIQUID-INFUSED SUPERHYDROPHOBIC SURFACES...............................103

5.1 Introduction 103
5.2 Experimental Setup 106
5.3 Results and Discussion..112
5.4 Conclusions 128

6. DROPLET IMPACT DYNAMICS ON LUBRICANT-INFUSED SUPERHYDROPHOBIC SURFACES......................130

6.1 Introduction 130
6.2 Experimental Setup 133
6.3 Results and Discussion..136
6.4 Conclusions 164

7. CONCLUSIONS AND CONTRIBUTIONS 168

BIBLIOGRAPHY..171

LIST OF FIGURES

Figure Page

Figure 1: Schematic diagram for (a) the three-phase contact line and the contact angle on a flat solid surface, (b) the advancing and receding contact angles, (c) Wenzel state, and (d) Cassie state on a rough solid surface. 4

Figure 2: Self-cleaning effect of lotus leaf [16]. Image (a) shows water being sprayed on the lotus leaf which has been already contaminated by soil particles, and Image (b) shows that shortly after the water spray the soil particles are being washed away along with water droplets from the leaf surface due to the self-cleaning effect. Inset is scanning electron microscope (SEM) image for micro-nano hierarchical structures on the lotus leaf......................6

Figure 3: A series of superhydrophobic surfaces found in literature. Included are SEM images of patterned superhydrophobic surfaces containing (a) an array of micro-posts [31], (b) micro-grooves [19], and (c) reentrant micro-posts [37] and (d) randomly rough superhydrophobic PTFE surfaces sanded by 240-grit sandpaper [33] and (e) spray coated surface [21]. 10

Figure 4: Schematic diagram showing the modified Wilhelmy plate method used in these experiments...25

Figure 5: A SEM image of a superhydrophobic paint surface..26

Figure 6: A microscope image of the surface structure for a superhydrophobic PTFE surface...26

Figure 7: Dynamic contact angle as a function of capillary number. The data include: the superhydrophobic paint surface with (circle) glycerin solution and (triangle) PEO solution; (star) the superhydrophobic PTFE surface with glycerin solution; a smooth PTFE surface with (closed square) PEO solution and (closed diamond) pure water. The smooth PTFE data has an uncertainty of ±1° while the superhydrophobic data has an uncertainty of ±3°..........................31

Figure 8: Contact angle hysteresis as a function of capillary number. The data include: the superhydrophobic paint surface with (circle) glycerin solution and (triangle) PEO solution; (star) the superhydrophobic PTFE surface with glycerin solution; a smooth PTFE surface with (closed square) PEO solution and (closed diamond) pure water. The smooth PTFE data has an uncertainty of ±1° while the superhydrophobic data has an uncertainty of ±3°..........................33

Figure 9: Plot of the difference in the cube of the static receding contact angle and the cube of the dynamic receding contact angle as a function of capillary number. The data include: the superhydrophobic paint surface with (circle) glycerin solution and (triangle) PEO solution; (star) the superhydrophobic PTFE surface with glycerin solution; a smooth PTFE surface with (closed square) PEO solution and (closed diamond) pure water. The smooth PTFE data has an uncertainty of ±1° while the superhydrophobic data has an uncertainty of ±3°. The solid lines represent fits to the Cox-Voinov-Tanner law with different slip lengths. For the superhydrophobic paint surface at low Capillary numbers, both data sets are fit well by a slip length of $b=12\mu\text{m}$ while at large Capillary numbers the data are fit by a slip length of $b=78\mu\text{m}$. 37

Figure 10: Fitting of the combined model to the receding contact angle as a function of capillary number. The data include: superhydrophobic paint surface with (circle) glycerin solution and (triangle) PEO solution; (star) a superhydrophobic PTFE surface with glycerin solution. The superhydrophobic data has an uncertainty of ±3°. The parameters used are below. For superhydrophobic paint surface with (circle) glycerin solution, $\lambda=7.3nm$, $K_\omega=3.4\times10^7$, $b=78\mu m$. For superhydrophobic paint surface with (triangle) PEO solution, $\lambda=4.7nm$, $K_\omega=5.5\times10^5$, $b=78\mu m$. For a superhydrophobic PTFE surface with glycerin solution, $\lambda=1.41nm$, $K_\omega=3.1\times10^5$, $b=78\mu m$...40

Figure 11: Steady shear viscosity measurements of the test fluids as a function of shear rate. The data include: 0.01wt% PAM solution (square); 0.05wt% PAM solution (triangle); viscoelastic PEO solution (star); and Newtonian PEO solution (circle)...51

Figure 12: Storage modulus (filled symbols) and loss modulus (hollow symbols) as a function of angular frequency. The data include: 0.01wt% PAM solution (square); 0.05wt% PAM solution (triangle); and viscoelastic PEO solution (star). 52

Figure 13: Advancing contact angle as a function of capillary number. Note the shear rate dependent viscosity was used to calculate the capillary number. The data include: 0.01wt% PAM solution (square); 0.05wt% PAM solution (triangle); viscoelastic PEO solution (star); Newtonian PEO solution (circle). Inset shows the several fits to the data using a second order polynomial to illustrate the method used to determine the static contact angle...57

Figure 14: Advancing contact angle as a function of Weissenberg number. The data include: 0.01wt% PAM solution (square); 0.05wt% PAM solution (triangle); viscoelastic PEO solution (star)...60

Figure 15: The difference in the cubes of dynamic and static advancing contact angles as a function of capillary number so that the scaling trends can be observed. Note that for Tanner's law, $\theta_A{}^3 - \theta_{A,s}{}^3 \propto Ca$. The data include: 0.01wt% PAM solution (square); 0.05wt% PAM solution (triangle); viscoelastic PEO solution (star); Newtonian PEO solution (circle). 62

Figure 16: Receding contact angle as a function of capillary number. The data include: 0.01wt% PAM solution (square); 0.05wt% PAM solution (triangle); viscoelastic PEO solution (star); pure water (diamond). 65

Figure 17: The difference in the cubes of the static and dynamic receding contact angle as a function of capillary number. Note that for Tanner's law $\theta_{R,s}{}^3 - \theta_R{}^3 \propto Ca$. The data include: 0.01wt% PAM solution (square); 0.05wt% PAM solution (triangle); viscoelastic PEO solution (star); pure water (diamond). 68

Figure 18: The difference in the cubes of the static and dynamic receding contact angle as a function of plate velocity. The experimental data include (a) advancing (filled square) and receding (void square) contact angles for the 0.01wt% PAM solution and (b) advancing (filled triangle) and receding (void triangle) contact angles for 0.05wt% PAM solution. Superimposed over the data is the theoretical prediction of Equation 15. 73

Figure 19: Schematic diagram of the experimental set up. Also included are (a) schematic diagram for pressure drop measurements, (b) top-down schematic diagram of the microchannel, and optical microscope images of (c) circular pillars and (d) apple-core-shaped superhydrophobic pillars. The diameter of each post, D_0, is 150μm spaced 225μm apart. 83

Figure 20: A series of microscope images showing the initialization of the microfluidic device and formation of the air-water interface in the superhydrophobic apple-core-shaped pillars at $Ca = 6.6 \times 10^{-5}$. Included are images of superhydrophobic pillars (a) dry prior to flow initialization, (b) during the wetting process, and (c) fully initialized. The flow direction is from left to right. 86

Figure 21: Pressure drop reduction as a function of non-dimensional interface diameter for flow through a microchannel containing a regular array of superhydrophobic apple-core-shaped pillars. The data is non-dimensionalized through comparison against an array of circular pillars with diameter D_0 and includes the experimental pressure drop (circles) and linear lines fitted to the data to guide the reader's eye (solid line). 90

Figure 22: Particle image velocimetry (PIV) vector fields of flow through a regular array of (a) circular and (b) and (c) superhydrophobic apple-core-shaped pillars at $Ca = 6.6\times10^{-5}$ with vorticity overlaid as a contour map. Solid lines are overlaid on the data to indicate the position of pillars while dashed lines are used to represent the position of the air-water interface formed by the air bubble trapped against the superhydrophobic pillar. For the superhydrophobic pillar, the non-dimensional diameter was measured to be (b) D/D_0=0.88 and (c) D/D_0=1.09 from bright-field image. 93

Figure 23: Non-dimensional streamwise velocity as a function of non-dimensional channel position, x/D_0. The streamwise velocities were measured along (a) the centerline between two posts, (b) at the edge of the solid surface or air-water interface of the upper pillar, and (c) at a position 4.4µm below the edge of the upper pillar. The velocity was non-dimensionalized by the average streamwise velocity, u/U_{avg}. Inset shows the locations of the measurement slices in relation to the two pillars. The experimental data include the velocity measured in the microchannel with the circular pillars (filled circle) and the superhydrophobic apple-core-shaped pillars (square for D/D_0=0.88 and diamond for D/D_0=1.09). 99

Figure 24: Non-dimensional streamwise velocity u/U_{avg} as a function of non-dimensional channel location for velocities evaluated along x/D_0=0. The experimental data include velocity profiles for circular pillars (○) and superhydrophobic pillars (●). The slip velocity data are superimposed on the interface lines with red symbols. The vertical solid lines at $y/D_0 = \pm0.75$ represent the edge of the circular pillar while the dashed lines at $y/D_0 = \pm0.7$ represent the location of the air-water interface formed around the superhydrophobic pillar. 100

Figure 25: Schematic diagram of the experimental set up used for pressure drop measurements. Also included are (a) a scanning electron microscopy image of a PTFE surface sanded with 240-grit sandpaper (RMS roughness of 13.7µm) and optical microscope images of (b) a PDMS surface consisting of 50µm posts spaced 50µm apart, and (c) a PDMS surface containing 30µm ridges spaced 30µm apart. 108

Figure 26: Microscope images of a superhydrophobic surface patterned with 30µm spacing micro-ridges (a) before flow showing all the channels between the micro-ridges fully filled with lubricating oil and (b) after a flow of U=0.4mm/s was applied for t=120 min showing oil partially stripped from between the micro-ridges. 115

Figure 27: Pressure drop as a function of time for a series of liquid-infused superhydrophobic sanded PTFE surfaces showing the longevity of the lubricating layer. The experimental data include PTFE surfaces sanded with a series of different sandpaper with grit designation of (square) 180-grit, (circle) 240-grit, and (triangle) 320-grit for the viscosity ratio of $\mu_w / \mu_o = 9.2$. The RMS surface roughness was estimated as 15.4µm, 13.7µm, and 10.9µm for 180-, 240-, and 320-grits of sandpaper based on the literature [33]. All experiments were performed at a constant flow velocity of *U*=0.4mm/s and a constant capillary number of *Ca*=0.001. The pressure drop data have a maximum uncertainty of 14 Pa. 119

Figure 28: The lubricant pools on the PTFE surface sanded with grit designation of 240-grit (RMS roughness of 13.7µm). This 150µm long slice of the surface was taken from actual profilometry measurements. It is a representational slice of the sanded PTFE surface. Superimposed on the surface topography is a schematic diagram of the evolution of the oil-water interface which we believe help to explain the experimental results. The initial condition of the surface is shown in (a) while in (b) the long time LIS is shown with oil depleted from the surface. 123

Figure 29: Pressure drop as a function of time for the liquid-infused superhydrophobic sanded PTFE surfaces sanded with a grit designation of 240-grit (RMS roughness of 13.7µm) at *Ca*=0.001. The experimental data include the viscosity ratio of (triangle) $\mu_w / \mu_o = 0.2$, (diamond) $\mu_w / \mu_o = 5.2$ and (circle) $\mu_w / \mu_o = 9.2$. Due to the change in the viscosity of the aqueous phase, to maintain a constant capillary number, the flow velocity increase with decreasing viscosity of the aqueous phase. The pressure drop data have a maximum uncertainty of 14 Pa. 126

Figure 30: Time evolution of an aqueous glycerin drop (µ=6cP) impacting on a series of test surfaces at Weber numbers of (a) *We*=52 and (b) *We*=132. The surfaces include: SM-smooth, SHS-superhydrophobic air-infused, LIS-lubricant-infused. For the lubricant-infused surface, the viscosity of the silicone oil in cP is included following LIS. 139

Figure 31: Time evolution of the diameter of the impacting drop normalized by the initial drop diameter at a Webber number of (a) *We*=52 and (b) *We*=132. The experimental data include: lubricant-infused roughened PTFE surfaces with 5cP silicone oil (circle), 14cP silicone oil (diamond), and 100cP silicone oil (square) as well as smooth PTFE surface (triangle) and air-infused superhydrophobic PTFE surface (star)..143

Figure 32: Time evolution of the spreading (+ve) and retraction (-ve) velocities of droplet impacts on a number of different surfaces at a Weber number of (a) *We*=52 and (b) *We*=132. The experimental data include: lubricant-infused roughened PTFE surfaces with 5cP silicone oil (circle) and 100cP silicone oil (square) as well as smooth PTFE surface (triangle) and air-infused superhydrophobic PTFE surface (star). 144

Figure 33: Energy dissipation as a function of time for droplet impacts at a Webber number of (a) *We*=52 and (b) *We*=132. The experimental data include impacts on: lubricant-infused roughened PTFE surfaces with 5cP silicone oil (circle), smooth PTFE surfaces (triangle) and air-infused superhydrophobic PTFE surfaces (star)...150

Figure 34: Time delay of impacting droplets at maximum spreading diameters. Data represents difference between the time to achieve 90% D_{max} during spreading and the time to reach 90% D_{max} during retraction of droplet from D_{max}. The data includes impacts on different test surfaces at impact Weber numbers of *We*=52 (circle) and *We*=132 (square). 154

Figure 35: Dynamic contact angle measured during droplet impact on a number of different surfaces as a function of (a) time after impact and (b) the instantaneous capillary number during spreading (positive) and retraction (negative) at a Weber number of *We*=52. The experimental data include: lubricant-infused roughened PTFE surfaces with 5cP silicone oil (filled circle), 14cP silicone oil (diamond), and 100cP silicone oil (filled square) as well as smooth PTFE surface (triangle) and air-infused roughened PTFE surface (star)..155

Figure 36: A log-log plot of maximum spreading diameter of the impacting aqueous glycerin drop normalized by the initial drop diameter as a function of Weber number. The experimental data include results for: lubricant-infused roughened PTFE surfaces with 5cP silicone oil (circle), 14cP silicone oil (diamond), and 100cP silicone oil (square) as well as a smooth PTFE surface (triangle) and a superhydrophobic air-infused roughened PTFE surface (star). The solid line of the air-infused case (star) indicates a scaling of $D_{\max} / D_0 \sim We^{1/4}$ from theory while the dotted line of LIS 100 case (square) indicates a scaling of $D_{\max} / D_0 \sim We^{1/5}$. 160

Figure 37: A scaling analysis for the maximum diameter of the aqueous glycerin drop normalized by the initial drop diameter as a function of Weber number. The experimental data include sanded lubricant-infused PTFE surfaces with 5cP silicone oil (circle), 14cP silicone oil (diamond), and 100cP silicone oil (square). All the data collapse with the selection of *t*/*h*=0.12................................163

CHAPTER 1

INTRODUCTION

1.1 Wettability of Surfaces

When a liquid droplet is contact with a solid surface, it makes a certain shape depending on a wettability of the surface. A liquid-vapor interface of the droplet intercepts the solid surface and forms a three phase contact line as shown in Figure 1a. The wettability of the surface is generally characterized by a contact angle which is the angle measured through the liquid at the three phase contact line. This angle was defined by Young's law [1] as follows:

$$\theta = \cos^{-1}\left((\gamma_{SV} - \gamma_{LS}) / \gamma_{LV}\right) \tag{1}$$

Here, γ_{SV} , γ_{LV} , and γ_{LS} are solid-vapor, liquid-vapor, and liquid-solid interfacial tensions, respectively. For surfaces with contact angles less than $\theta < 90°$ the surface is considered hydrophilic while for $\theta \geq 90°$ the surface is hydrophobic.

In reality, due to the presence of surface roughness or chemical heterogeneity, the contact angle exists anywhere between advancing, θ_A, and receding, θ_R, contact angles [2]. The difference between the advancing and receding contact angles is called as a contact angle hysteresis, $\theta_H = \theta_A - \theta_R$. The schematic diagram for the advancing and receding contact angles is shown in Figure 1b. These angles are quantified by increasing or decreasing the volume of a liquid droplet on a surface [3]. As the volume of the droplet is increased, the angle reaches the maximum value right before the contact line depins and advances toward next pinning defects. This is defined as the advancing contact angle,

θ_A. On the other hand, the angle reaches the minimum value when sucking the liquid from the drop. The receding contact angle is the minimum angle measured when the contact line depins and retracts toward next pinning defects. The advancing contact angle is known to be always larger than or equal to the receding contact angle. Without an introduction of surface roughness, the advancing contact angle never exceeds 120° even if the surface has chemical hydrophobicity [4].

The influence of surface roughness was first discussed by Wenzel [5] and then by Cassie and Baxter [6]. As shown in Figure 1c, in the Wenzel state [5], water penetrates into the space between peaks of the surface roughness on the surface. In this state, the equilibrium contact angle, θ_W, has been described as follows:

$$\cos\theta_W = r\cos\theta. \tag{2}$$

Here, r is a roughness parameter which is the ratio of the actual wetted area to the projected area of the surface, and θ is Young's angle. In the Wenzel state, the contact line is pinned along the sides and corners of posts, resulting that the contact angle hysteresis is typically quite large [7].

However, as the surface hydrophobicity increases, the water does not penetrate into the gap between the protrusions of surface roughness as shown in Figure 1d. It results in the formation of an air-water interface. This state is called Cassie state [6]. The equilibrium contact angle, θ_C, in the Cassie state has been described as follows:

$$\cos\theta_C = -1 + \phi_S\left(1+\cos\theta\right). \tag{3}$$

Here, ϕ_s is fraction of solid on the surface and can be described as $\phi_s = d^2/(d+w)^2$ for a periodic array of square posts with dimensions shown in Figure 1d. In the Cassie state, the equilibrium contact angle increases with increasing the amount of air-water interface, $(1-\phi_S)$. In the limit of extremely small solid fraction, $\phi_s \to 0$, for example, the equilibrium contact angle, θ_C, reaches 180°, $\theta_C \to 180^\circ$. Furthermore, in the Cassie state, the contact line is only pinned at the solid peaks, thus enhancing drop mobility by minimizing the contact angle hysteresis. The Cassie state is the one of interest due to these large advancing contact angle and extremely low contact angle hysteresis.

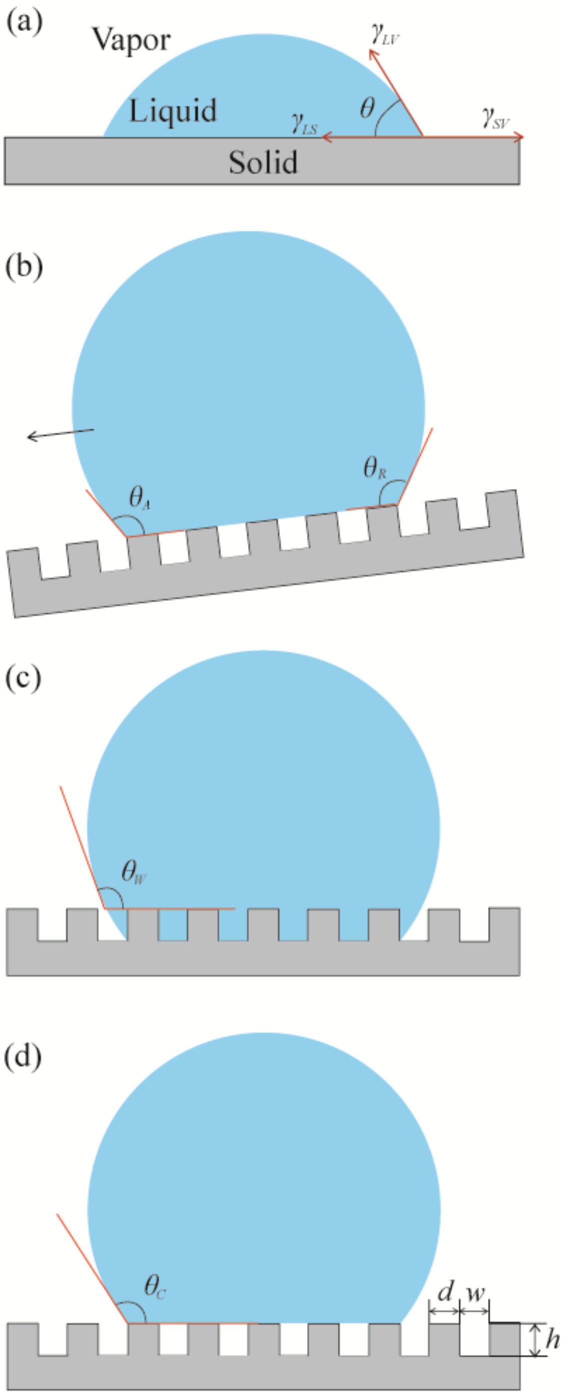
(a)
Vapor
γ_{LV}
Liquid
γ_{LS}
θ
γ_{SV}
Solid
(b)
θ_R
θ_A
(c)
θ_W
(d)
θ_C
d
w
h

Figure 1: Schematic diagram for (a) the three-phase contact line and the contact angle on a flat solid surface, (b) the advancing and receding contact angles, (c) Wenzel state, and (d) Cassie state on a rough solid surface.

1.2 Superhydrophobic Surfaces

Superhydrophobic surfaces are originally inspired by the unique water repellent characteristic of lotus leaves and have been observed in many plants and insects around the world [8-14]. They are rough hydrophobic surfaces containing micron and/or nanometer-sized surface structures. Both the chemical hydrophobicity and topological features prevent water from penetrating into the gap between the protrusions in the surface roughness. It results in the formation of an air-water interface [15]. As shown in Figure 2 [16], for example, the lotus leaf has micron and nanometer-sized hierarchical structures on which epicuticular waxes are coated. It exhibits extremely low adhesion to water droplets, resulting in so-called self-cleaning effect.

The air-water interface of superhydrophobic surfaces is known to produce large advancing contact angles, $\theta_A = 150^\circ$, and small contact angle hysteresis, $\theta_H = \theta_A - \theta_R \approx 5^\circ$ [15]. This extreme water repellency gives lotus leaves and other plants their self-cleaning properties [8, 17], enables water striders to walk or even jump on the water [10], and makes it possible for insects and spiders to breath under water [9, 12]. In addition, the superhydrophobic surfaces have been shown to reduce drag in both laminar and turbulent flow [15, 18-25] and produced anti-fouling [26, 27] and/or anti-icing effects [28, 29].

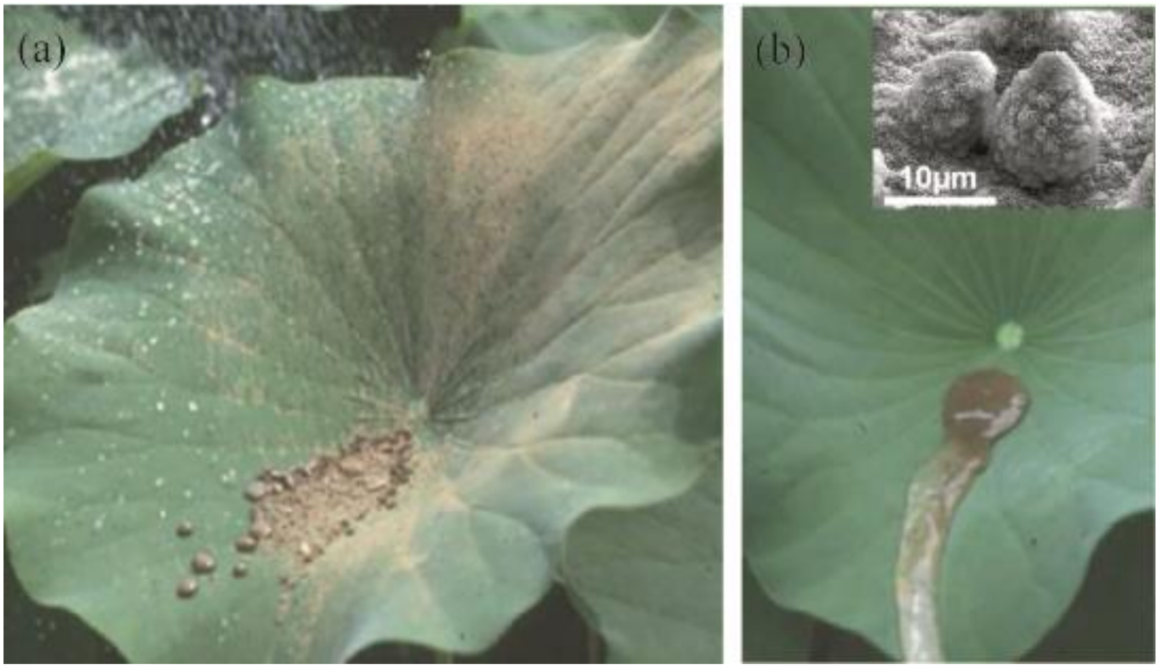

Figure 2: Self-cleaning effect of lotus leaf [16]. Image (a) shows water being sprayed on the lotus leaf which has been already contaminated by soil particles, and Image (b) shows that shortly after the water spray the soil particles are being washed away along with water droplets from the leaf surface due to the self-cleaning effect. Inset is scanning electron microscope (SEM) image for micro-nano hierarchical structures on the lotus leaf.

1.2.1 Fabrication of Superhydrophobic Surfaces

Because of the abilities of the superhydrophobic surfaces mentioned, fabricating superhydrophobic surfaces has drawn attention to a number of people over the last two decades [18, 19, 30-40]. Extensive investigations in the past have revealed that proper structure sizing and spacing between structures were required in effectively maintaining the air-water interface and controlling the wettability of the surfaces. Thereby, they could maximize performance of the superhydrophobic surfaces. There are various fabrication techniques that have been developed. We will divide the techniques for patterned and randomly rough superhydrophobic surfaces, respectively.

As for the patterned superhydrophobic surfaces, a photolithography technique is one of typical ways to create the surfaces. This technique utilizes light to transfer patterns from a mask to a photoresist layer spun onto the substrate. Then, the substrate was used as a superhydrophobic surface through an additional chemical process [18, 19, 31], or the patterns on the substrate were replicated into a flexible material by a soft lithography technique [40]. Oner and McCarthy [31] created a number of patterned superhydrophobic surfaces containing micro-posts that were prepared by a photolithography technique and hydrophobized using silanization chemistry as shown in Figure 3a. They demonstrated that contact angles were independent of surface chemistry. However, proper sizing of the posts and separations between posts were found to be critical to produce large advancing contact angles and small contact angle hysteresis. As shown in Figure 3b, Ou et al. [18, 19] created patterned superhydrophobic surfaces with micron-sized grooves and posts using a photolithography technique as well as a chemical reaction with an organosilane. Their patterned surfaces had large advancing contact angles, $130^\circ < \theta_{eq} < 174^\circ$, with small contact angle hysteresis and produced significant laminar drag reduction in the microchannel. In addition, electron (e-beam) lithography was used to fabricate micron and nanometer-sized hierarchical superhydrophobic posts on the surfaces [35]. Jucius et al. [36] created superhydrophobic polytetrafluoroethylene (PTFE) surfaces by embossing them with reusable micro-featured stamps in the form of 2D array of pits. Recently, doubly reentrant micro-posts containing nanoscale vertical overhangs were developed on silicon dioxide surfaces by micromachining them with several etching steps as shown in Figure 3c [37]. These surfaces have been spotlighted because of their super repellency for liquids with low surface tension.

A series of patterned superhydrophobic surfaces generally necessitate extensive material or facility costs. In addition, there is a limitation of creating large-area patterned superhydrophobic surfaces. In this respect, randomly rough superhydrophobic surfaces diverted people's attention away from the issue. These irregular surfaces were much more similar to the surfaces found in nature rather than the patterned surfaces.

One of the ways to create randomly superhydrophobic surfaces was developed by Nilsson et al. [33]. By sanding commercial polytetrafluoroethylene (PTFE) surfaces using different grits sandpapers as shown in Figure 3d, superhydrophobic surfaces with many kinds of contact angle hysteresis can be created. This inexpensive method enables us to produce superhydrophobic surfaces with from Wenzel to Cassie states of wetting, and thereby to carry out experiments for droplet motions and drag reductions [24, 41]. In addition, Srinivasan et al. [21, 38] fabricated irregular superhydrophobic surfaces by spray coating a 50/50 solution of Polymethyl methacrylate (PMMA)/fluorodecyl polyhedraloligomeric silsesquioxane (FPOSS) on the solid surface and stainless steel woven meshes. For drag reduction measurements, they used the surfaces as an inner rotor for turbulent Taylor-Couette flows and one of parallel plates in a rheometer. An apparent contact angle of 161° was measured on the sprayed substrates as shown in Figure 3e. In addition, randomly rough superhydrophobic surfaces have been created by spraying commercial superhydrophobic paint, Fluorothane (WX 2100), to substrates. This paint is available in an aerosol spray form and 5 microns-sized hydrophobic particles were deposited on the substrate. A high advancing contact angles, $\theta_A = 155^{\circ}$, and low contact angle hysteresis, $\theta_H = 8^{\circ}$, were measured on the surfaces that the paint was sprayed [39].

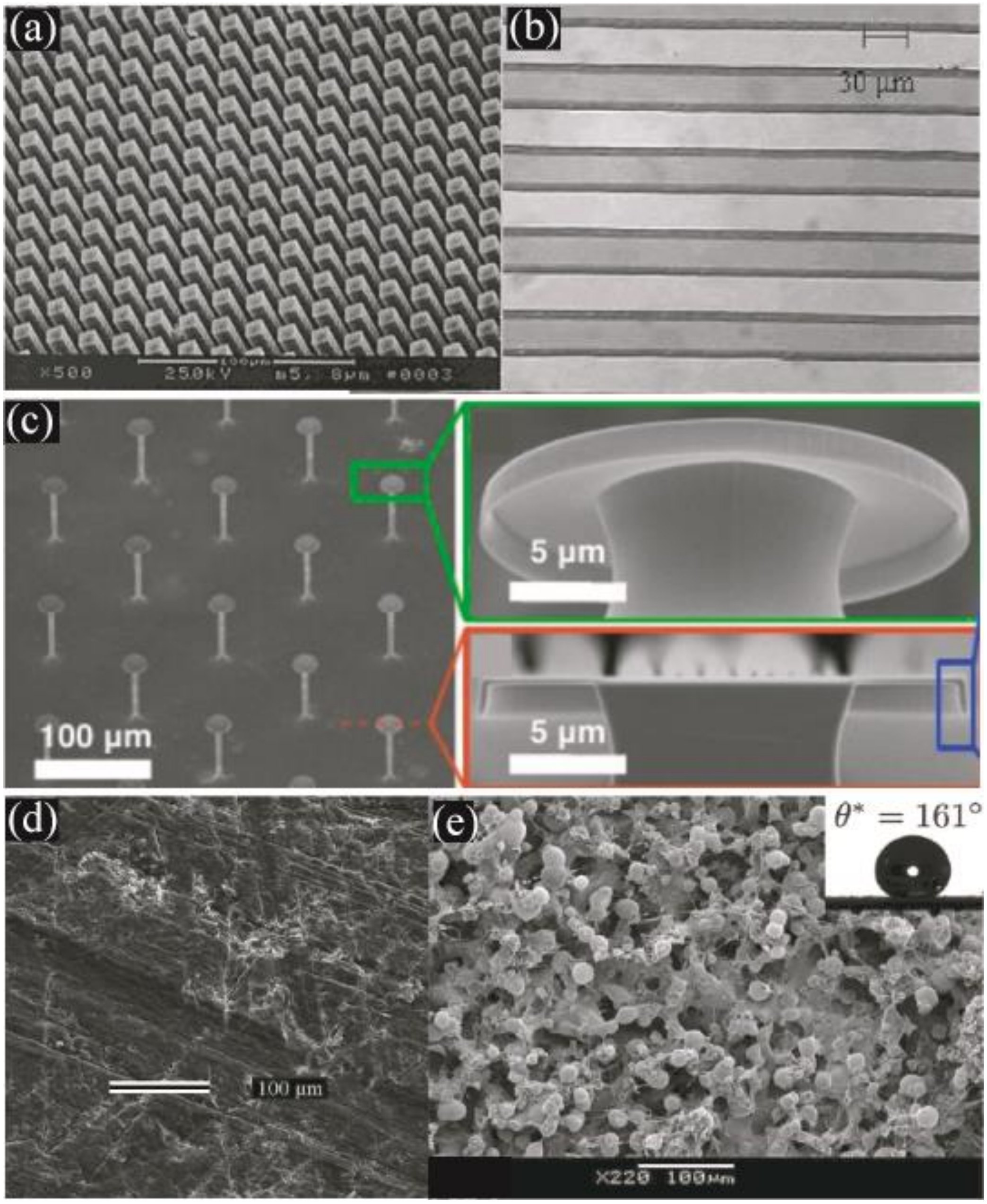
(a)
×500
100µm
25.0kV
m5, 8µm
#0003
(b)
30 µm
(c)
100 µm
5 µm
5 µm
(d)
100 µm
(e)
$\theta^* = 161°$
×220 100µm

Figure 3: A series of superhydrophobic surfaces found in literature. Included are SEM images of patterned superhydrophobic surfaces containing (a) an array of micro-posts [31], (b) micro-grooves [19], and (c) reentrant micro-posts [37] and (d) randomly rough superhydrophobic PTFE surfaces sanded by 240-grit sandpaper [33] and (e) spray coated surface [21].

1.2.2 Engineering Application in Drag Reduction

The superhydrophobic surfaces have been shown to reduce drag in laminar and turbulent flows by changing the boundary condition from a no-slip condition to a slip boundary condition [15]. Navier was the first one who proposed the slip boundary condition. In his model, the magnitude of the slip velocity, u_0, is proportional to the magnitude of the shear rate experienced by the fluid at the wall

$$u_0 = b\left|\frac{\partial u}{\partial y}\right|, \tag{4}$$

where b is the slip length. The slip length is hypothetical length to be extended to achieve slip velocity at the slip wall. For nearly all macroscopic flows of simple fluids, the slip length is very small, $b = \mathrm{O}(1\mathrm{nm})$ [42, 43] that the no-slip boundary condition can be used.

The slip length for the superhydrophobic surfaces was measured by indirect pressure drop measurements [18] and a direct measurement of micro particle image velocimetry [19, 44, 45]. In particular, Ou et al. used both measuring techniques in a microchannel with superhydrophobic surfaces containing precisely patterned micro-grooves. The slip length was measured to be 5µm from the pressure drop. This was similar to the slip length directly measured by µPIV which was 7.5µm. The slip length was also found to increase with increasing the spacing between surface structures [18]. Later, Ybert et al. developed a scaling analysis for the slip length on patterned superhydrophobic surfaces and demonstrated that the slip length should be proportional to the period of the microstructure, $b \sim d + w$.

A number of experiments have been performed to measure drag reduction on various superhydrophobic surfaces under several flow geometries [18, 20, 22, 24, 38, 46, 47]. In the laminar channel flow, Watanabe et al. [22] used millimeter-sized circular pipe consisting of a highly water-repellent wall. The maximum drag reduction of 14% was achieved in the laminar flow regime. Ou et al. [18] measured the pressure drop for the flow past superhydrophobic surfaces containing a regular array of micro-posts in the microchannel. The maximum drag reduction of 40% and corresponding apparent slip length of 20μm were measured. With changing the size of the features and the space between the features, the drag reduction was found to increase with increasing the area of the shear-free air-water interface by enlarging the gaps between the features and reducing the channel height [18]. Dong et al. [24] utilized superhydrophobic sanded PTFE surfaces and measured pressure drop in the microchannel. They showed the maximum pressure drop reduction of 27% and corresponding slip length of 20μm were obtained for the PTFE surface sanded by 240-grits sandpaper. Also, they revealed that a sanding protocol affected drag reduction on sanded PTFE surfaces. The surface sanded toward the flow direction of the microchannel reduced the pinning force; hence, enhanced drag reductions. Daniello et al. [20] used a rectangular flow cell with superhydrophobic PDMS walls with 30μm and 60μm wide micro-grooves spaced 30μm and 60μm apart, respectively. They measured the pressure drop in the cell under laminar to turbulent flows. They discovered that the drag reduction was not attained in laminar flow regime even if the air-water interface was present on the superhydrophobic micro-grooves. With increasing Reynolds number in the channel, the viscous sublayer was comparable to the feature size, resulting in drag reduction in the turbulent flow regime. The maximum drag reduction up to 50%

and corresponding slip length of 80μm were measured at the largest Reynolds number tested. In the experiment of hydrofoil under turbulent flow, Gogte et al. reported the maximum drag reduction of 18% over a hydrofoil coated with an unstructured superhydrophobic surface consisting of hydrophobically-modified sandpaper.

Drag reduction measurements have been also performed using a cone-and-plate rheometer [21, 48]. Choi and Kim [48] created a Teflon coated needle-like structure on a silicon wafer and measured the drag reduction using the rheometer. Slip lengths of $b \approx 20\mu\text{m}$ and $b \approx 50\mu\text{m}$ were observed for water and glycerin, respectively. Srinivasan et al. [21] created a randomly rough spray-coated fluorodecyl POSS-PMMA superhydrophobic surface as well as a series of spray-coated woven meshes and measured the drag reduction in a parallel plate rheometer. They reported the slip length of 39μm for the spray-coated substrate. In addition, the slip length on the spray-coated meshes was varied from 94μm to 213μm depending on the fraction of shear-free interface. Srinivasan et al. [38] also applied the same solution to the inner rotor surface of Taylor-Couette flow configuration to investigate the reduction in wall shear stress. The skin friction was reduced with growing the Reynolds number, increasing up to a value of 22% at $Re=8.0\times10^4$.

1.3 Motivation

Despite the fact that a number of techniques to fabricate superhydrophobic surfaces and corresponding static contact angle measurements have been performed through extensive research, there is no experimental evidence for the dynamic wetting on superhydrophobic surfaces. The static contact angle can be laid anywhere between static advancing and receding contact angles, meaning that solely with this limited variation of the static contact angles, the dynamics of liquid droplets, jets, or streams along the superhydrophobic surfaces cannot be fully described.

The presence of the air-water interface is crucial for enabling the capabilities of superhydrophobic surfaces. Most of the experimental and theoretical investigations on drag reduction and corresponding slip length assumed the shape of the air-water interface to be flat. In reality, this assumption does not necessarily apply to all the superhydrophobic surface cases. The air-water interface can be changed from a concave to convex shape with changing the static or dynamic pressures on the surfaces. Further studies on the effect of the interface shape on drag-reducing properties are also necessary to investigate the ways to maximize the performance of the superhydrophobic surfaces.

There are a number of inherent issues on application of superhydrophobic surfaces hindering their wide range of adaptations [15, 49]. The air trapped within the structures on the superhydrophobic surfaces can collapse under high static or dynamic pressure [50]. As seen in Figure 1d, the maximum pressure to maintain the shear-free air-water interface between the two parallel ridges relies on the spacing of the patterns, w, the interface tension between liquid and vapor, γ_{LV}, and the contact angle, θ_A. The maximum pressure difference between the water and air phase is calculated as below [15].

$$\Delta p_{\max} = p_{water} - p_{air} = -\frac{2\gamma_{LV}\cos\theta_A}{w} \tag{5}$$

Loss of the trapped air can also occur when the superhydrophobic surface is brought in contact with organic liquids or complex mixtures with low surface tension. Additionally, defects introduced during manufacturing process or mechanical damage incurred during experimentation might cause a loss of the air-water interface [3, 50]. Without the air-water interface, the attractive benefits of the superhydrophobic surfaces for drag reduction, droplet mobilization, or anti-icing cannot be manifested.

As an alternative to the conventional air-infused superhydrophobic surfaces, liquid-infused superhydrophobic surfaces have been spotlighted over the last five years [49, 51-57]. The immiscible and incompressible lubricants were infused into structures where the air that fills the gaps on the superhydrophobic surface, creating a fluid-fluid interface on the surfaces. These surfaces have been shown to resist high static pressure, exhibit extremely high liquid repellency, and restore the liquid repellency property from mechanical damages [49]. However, liquid-infused superhydrophobic surfaces can lose their benefits if the lubricant is evaporated over time or depleted under the conditions of high shear flow [49]. Therefore, several interesting questions can be raised regarding a lifetime of the lubricant under the shear flow to maintain drag-reducing property and the ways to improve the performance of the liquid repellency under certain flow conditions.

1.4 Dissertation Outline

In this dissertation, we will first study the dynamic wetting on superhydrophobic surfaces using a modified Wilhelmy technique. A series of dynamic advancing and receding contact angle measurements will give us a better way to control and optimize dynamics of droplets, jets and streams along the superhydrophobic surfaces. With the same technique, the dynamic contact angles of a series of viscoelastic fluids will be discussed. Next, we will examine the pressure drop and velocity vector fields in a microchannel containing a regular array of apple-core-shaped superhydrophobic pillars. The shapes of the air-water interface on the surfaces will be systematically changed to investigate the role of the air-water interface shapes on drag reduction. Then, we will present a series of developed liquid-infused superhydrophobic surfaces and systematic measurements of the pressure drop through microchannels. By changing flow conditions, we will examine how the viscosity ratio between water and oil phase affects drag-reducing properties and how long the lubricant will be maintained in the structures. Finally, we will discuss how the viscosity ratio between impinging droplets and the lubricant affects dynamics of the droplets in the liquid-infused superhydrophobic surfaces.

CHAPTER 2

DYNAMIC CONTACT ANGLE MEASUREMENTS ON SUPERHYDROPHOBIC SURFACES

2.1 Introduction

Superhydrophobic surfaces have been observed in many plants and insects around the world [8-14]. They are characterized by two important factors: chemical hydrophobicity and micron or nanometer sized surface roughness. The combination of low surface energy and surface roughness can trap an air layer on the surface, resulting in the formation of air-water interface between the peaks of surface roughness. The presence of the air-water interface can result in a large static advancing contact angle, $\theta_A > 150°$, and little contact angle hysteresis which is defined as the difference between advancing and receding contact angles, $\theta_A \approx \theta_R$. This extreme water repellency gives the lotus leaf and other plants their self-cleaning properties, allows water strider to walk or even jump on the water [10] and makes it possible for insects and spiders to breath under water [9, 12]. The low contact angle hysteresis also enables droplets to move easily across the surface due to the reduction of the pinning force [58-61]. In addition, superhydrophobic surfaces have been shown to reduce drag in both laminar and turbulent flow. The presence of air-water interface changes the boundary condition on the superhydrophobic surfaces from the classic no-slip condition to a partial slip condition [15, 18-20].

In the superhydrophobic surface literature, only static advancing and receding contact angles have been reported to date. However, under flow conditions, the dynamics of the three phase contact line and the resulting dynamic contact angles are known to be influenced by molecular-level adsorption/desorption phenomena and macroscopic flow-induced viscous dissipation [2, 62]. Dynamic contact angle measurements have been made for a wide variety different liquids and surfaces [62-64], yet no dynamic contact angle measurements exist for superhydrophobic surfaces. From the measurements in the literature and the predictions of theoretical calculations, the dynamic advancing contact angle has been shown to increase with increasing velocity of the three phase contact line while the dynamic receding contact angle has been found to decrease with increasing velocity. If we are to fully understand the motion of droplets, jets and streams along superhydrophobic surfaces, it is essential that measurements of the dynamic contact angle on superhydrophobic surfaces be performed.

Several techniques have been introduced to measure the dynamic contact angles. For the case of forced wetting, displacement of liquid in a capillary tube and plunging a surface into a tank are common techniques to measure the dynamic contact angles. In both experiments, the gravity and inertial effects can typically be neglected. The early experiments of Hoffman used a glass capillary tube and measured the variation of dynamic contact angles over a wide range of wetting velocities [63]. By normalizing the data with the capillary numbers, $Ca = \mu U / \gamma$, where μ is the viscosity, U is the spreading velocity and γ is the interfacial tension, Hoffman showed that all the dynamic contact angle data could be collapsed onto a single master curve [63]. The plunge tank configuration is frequently used to measure the dynamic contact angle because it provides easy access to visualize the contact line. In this experiment, the contact line is observed as the solid substrate, typically a Wilhelmy plate or a cylindrical strand of material, is immersed into an open container of liquid [65-68]. Petrov et al. showed that one advantage of the plunge-tank technique is the ability to probe both the dynamic advancing and receding contact angles and as a result the dynamic contact angle hysteresis [69].

In order to understand the origins of the dynamic contact angle, one must consider the macroscopic and molecular dynamics occurring in close proximity to the three phase contact line. If, as is conventional in continuum fluid dynamics, the no-slip boundary condition is assumed, the viscous stress in the fluid and the force applied to the solid become infinite at a moving three phase contact line [70]. This stress singularity makes solution of the Navier-Stokes equations impossible with a moving contact line. By relaxing the no-slip condition at the contact line and allowing for a small but finite slip, Voinov derived a hydrodynamic relation between the contact line speed and the contact angle of liquids as they spread across a solid surface [71]. Voinov assumed capillary number was small ($Ca \ll 1$) and that the liquid-gas interface could be considered static far from the contact line [71]. The contact angle of the drops was also assumed to be sufficiently small to allow for a lubrication analysis to be used which amongst other things allows the motion of the liquid in the drops to be treated as one-dimensional. These assumptions lead to the classic relationship between dynamic contact angle and the capillary number, $\theta_D{}^3 \propto Ca.$ The same scaling was derived for the spreading of a fully wetting drop by Tanner [72]. This result is known as the Cox-Voinov-Tanner scaling law. By matching the static or equilibrium contact angle with the hydrodynamic solution, Voinov [71] and later Cox [73] were able to obtain an exact solution for partially wetting fluids which we will call the Cox-Voinov model

$$\theta_D{}^3 = \theta_S{}^3 \pm (9\mu U/\gamma)\ln(L/b), \tag{6}$$

Here θ_S is static contact angle, L is characteristic length scale of the outer region of the flow, and b is the slip length. For most surfaces, the slip length is on the order of $b \approx 10^{-9}$m or less. Often the outer length scale is chosen to be a constant times the capillary length, $L = \alpha\kappa^{-1} = \alpha\sqrt{\gamma/\rho g}$. The value of the constant α is not universal and has been shown to be dependent on the flow geometry as well as the boundary conditions [71, 74-76]. Perhaps most interesting, the predictions of Eggers and Stone showed that α may not even be a constant at all, but instead dependent on the capillary number of the flow [75]. It is also important to note that the value of the constant, α, depends on whether the contact line is advancing or receding [74]. Eggers predicted that the form of Equation 6 holds for the dynamic receding contact angle [77], however, the value of the constant is different than that found by Hocking for dynamic advancing contact and is given by $\alpha = 2\left(\cos\theta_{plate} - \cos\theta_S\right)/3$ [76]. Here θ_{plate} is the plunge angle the plate makes with the horizontal. It is this form that we will use to fit our receding contact angle data.

At low to moderate Capillary numbers, the dynamic contact angle measurements on liquid/solid systems with complete and partial equilibrium wetting have been found to follow the Cox-Voinov-Tanner scaling law over a wide range of flow configurations [63, 66, 78, 79]. Surprisingly, the Cox-Voinov model given in Equation 6 has been shown to hold even at large contact angles. In these cases of partially wetting fluids, Snoeijer showed that the solution to the hydrodynamic model for droplet spreading can be generalized beyond the assumptions of the small contact angle and lubrication flow and did not deviate by more than a few percent from Equation 6 up to angles as large as 150°

[80]. Although it is widely accepted, the Cox-Voinov-Tanner scaling law is not universal. It has been observed to fail at extremely low capillary number regime, $Ca < 10^{-4}$, and at very large capillary numbers, $Ca > O(0.1)$, where air entrainment, complete coating and the effects of inertia have been observed [81]. In addition to the hydrodynamic models, a number of other physical and empirical models exist to describe the evolution of the dynamic contact angle with capillary number [81, 82].

Blake and Haynes developed a molecular kinetic theory in order to explain the motion of three phase contact line and the dynamic contact angle [83]. In this approach, the dependence of the dynamic contact angle on the contact line velocity is the result of molecular adsorption and desorption at the moving contact line. The dynamic contact angle is related to velocity by

$$\theta_D = \cos^{-1}[\cos\theta_S - (2k_B T / \gamma\lambda^2)\sinh^{-1}(U / 2K_\omega\lambda)] \tag{7}$$

where k_B is the Boltzmann constant, and T is the temperature. The constant λ relates to the distance between adsorption sites on the solid surface, and the constant K_ω is the equilibrium frequency of the random molecular displacements occurring within the three-phase zone. These parameters are determined by a curve fitting of experimental data and typically have approximately $10^{-9}\,\mathrm{m}$ and $10^{6}\,\mathrm{s}^{-1}$, respectively. In many cases, especially at low velocities, the molecular-kinetic model fits the experimental data well [84-86]. Unfortunately, there is no definitive way of predicting the values of the parameters K_ω and λ a priori.

There have been a large number of experimental results predicted by each wetting theory despite their fundamentally different physics and approaches. For small dynamic contact angles, the hydrodynamic and molecular kinetic model predict fundamentally different scaling laws such that ${\theta_D}^3 \propto U$ and ${\theta_D}^2 \propto U$, respectively. The applicability of these two theories has been debated in the literature. However, it is clear that both the viscous dissipation and the wetting-line friction play a role in determining the dynamic contact angle.

In this paper, we will present the first dynamic contact angle measurements on superhydrophobic surfaces. Two different superhydrophobic surfaces, one randomly rough and one precisely patterned, will be fabricated and tested with a series of different aqueous solution with different viscosities so that the dynamic contact angle can be measured over a large range of capillary numbers. The experimental results presented in this paper will demonstrate that the dynamic wetting on superhydrophobic surfaces does not follow the scaling law predicted by either the hydrodynamic or the molecular kinetic model. Instead, we will show that for superhydrophobic surfaces the dynamic contact angle has a much weaker dependence on contact line speed.

2.2 Experimental Setup

A modified Wilhelmy plate method was used to measure the dynamic advancing and receding contact angles. A schematic diagram of the Wilhelmy plate is presented in Figure 4. In this study, both hydrophobic and superhydrophobic plates were used. The hydrophobic surface was fabricated from a smooth PTFE (Teflon) sheet purchased from McMaster-Carr which has an RMS roughness measured to be 5μm [33]. The static contact angles on the smooth PTFE were measured to be $\theta_{A,s} = 100°$ and $\theta_{R,s} = 75°$, respectively.

Two different superhydrophobic surfaces were also studied; one having randomly distributed surface roughness and the other containing a regular pattern of surface roughness. The randomly rough surface consisted of an acrylic plate spray painted with a commercially-available superhydrophobic paint (WX2100, Cytonix). An SEM image of the surface is presented in Figure 5 to show the details of the resulting surface topography. The paint consists of particles approximately 5μm in diameter suspended in a hydrophobic fluorothane resin. Upon deposition, a surface with random granular features was produced as seen in Figure 5. The RMS roughness of the final surfaces was on the same order as the particle size. The static advancing and receding contact angles on the spray-painted surface were measured to be $\theta_{A,s} = 159°$ and $\theta_{R,s} = 140°$.

The regularly patterned superhydrophobic surface was fabricated by hot embossing a pattern of posts into a smooth PTFE surface. A woven stainless steel mesh with 38μm diameter wires spaced 38μm apart was used as the master and a hot press raised to 325℃ was used to drive the PTFE into the spaces between the wire mesh. A microscope image of the resulting surface topography can be seen in Figure 6. The patterned PTFE surface contains a series of elongated oval-shaped posts, measured to be roughly 40μm wide and 80μm long and 40μm tall. Due to the weave of the stainless steel mesh, the orientation of adjacent posts can be seen in Figure 6 to be rotated by 90° with respect to each other. The minimum spacing between posts is roughly 40μm. The static advancing and receding contact angles on the superhydrophobic PTFE surface were measured to be $\theta_{A,s} = 151°$ and $\theta_{R,s} = 142°$.

A series of test fluids were used with different viscosities so that the capillary number could be systematically varied. The initial test fluid was water. In addition, a series of high viscosity aqueous solutions were used. The first solution consisted of 20wt% of a low molecular weight polyethylene oxide (PEO) (Mw = 20,000g/mol) in water. The second solution was 83% glycerin in water. Both solutions were gently mixed for at least 24 hours to ensure complete dissolution. Both the aqueous PEO and glycerin in water solutions had a constant viscosity of $\mu = 0.063 \mathrm{Pa \cdot s}$ and surface tensions of $\gamma = 60\ \mathrm{mN/m}$.

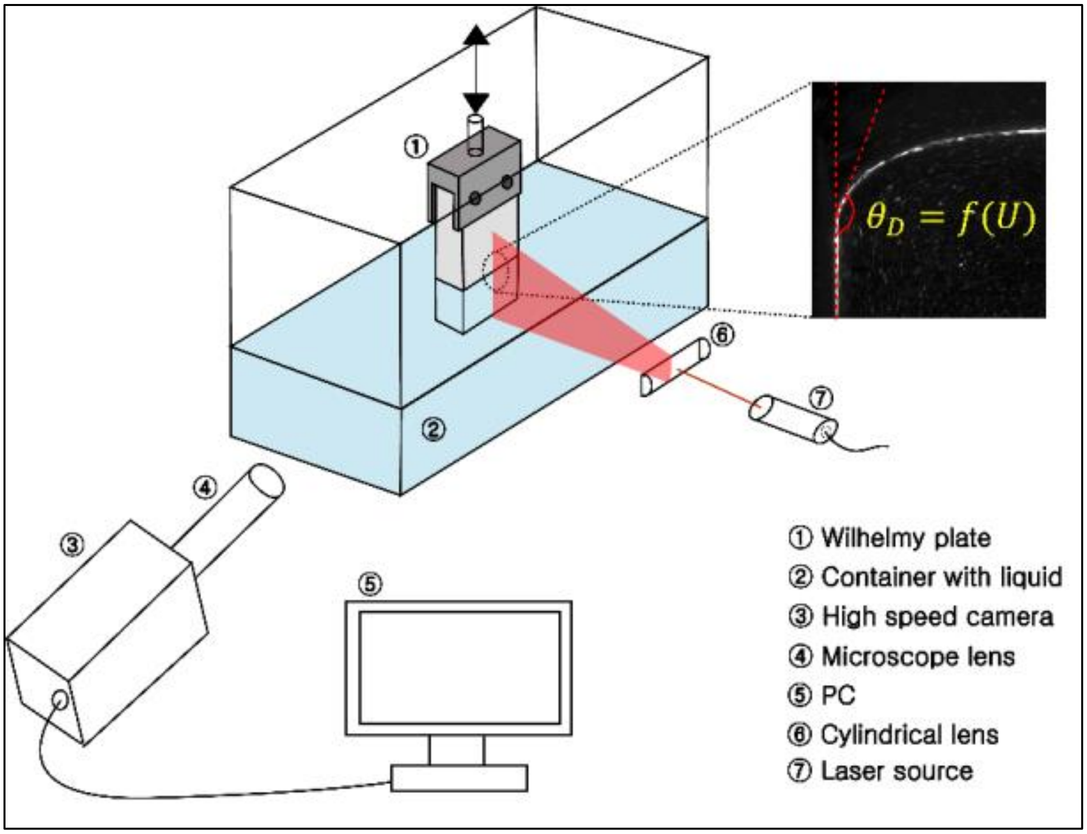
①
⑥
⑦
②
④
③
⑤
$\theta_D = f(U)$
① Wilhelmy plate
② Container with liquid
③ High speed camera
④ Microscope lens
⑤ PC
⑥ Cylindrical lens
⑦ Laser source

Figure 4: Schematic diagram showing the modified Wilhelmy plate method used in these experiments.

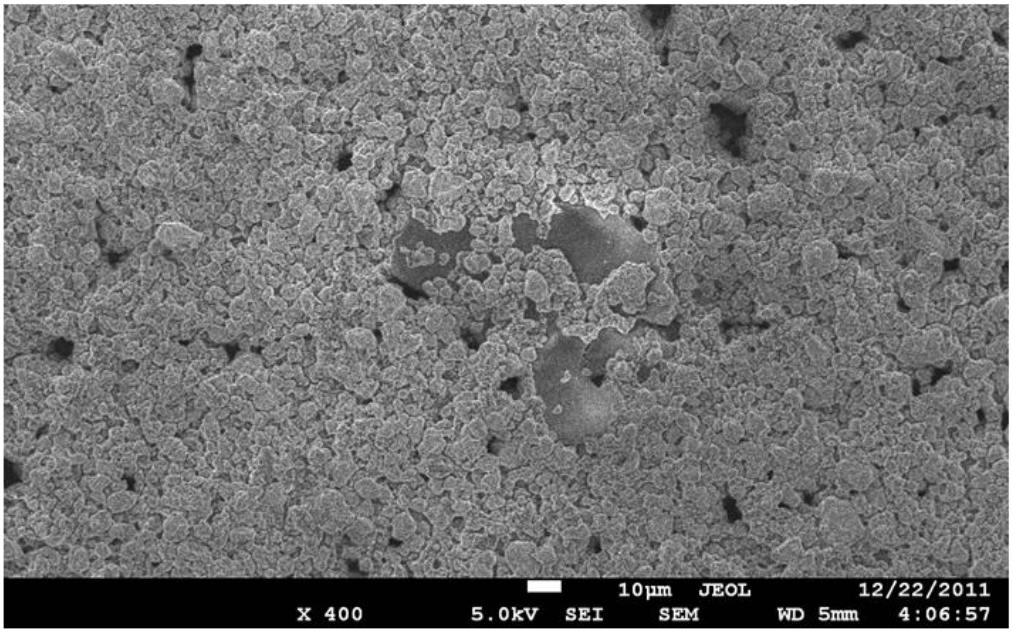
10µm JEOL 12/22/2011
X 400 5.0kV SEI SEM WD 5mm 4:06:57

Figure 5: A SEM image of a superhydrophobic paint surface

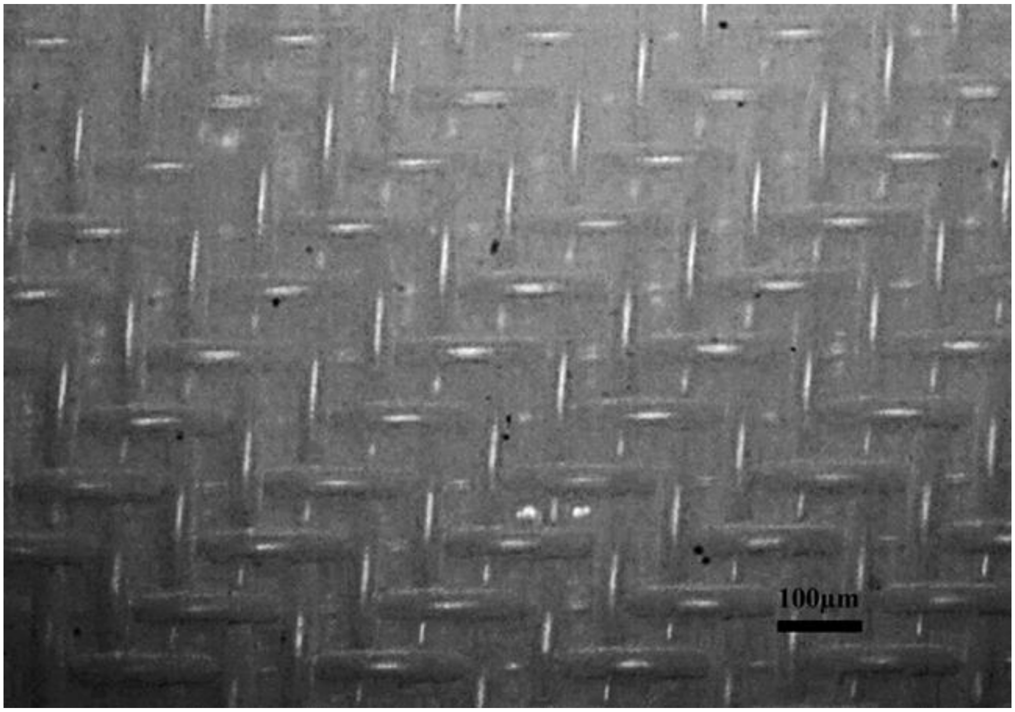

Figure 6: A microscope image of the surface structure for a superhydrophobic PTFE surface

The test surfaces were attached to a linear motor and were alternately immersed into and withdrawn from a reservoir of the test fluid so that the advancing and receding contact angles could be measured. No significant change in the dynamic contact angle measurements were observed with multiple sequential immersions of the plate into the reservoir. Additionally, the plate was found to be dry to the touch upon removal from the fluid. The curvature of the air-liquid interface near the contact line was recorded by a high-speed camera at sample rates up to 200Hz and optically zoomed in so that a 3cm x 3cm field of view could be observed. To effectively visualize the flow, thirteen micron diameter silvered hollow glass spheres (Sphericel, Potters Industry) often used for particle image velocimetry (PIV) were added to the test fluids at concentrations less than 0.1wt%. The particles were not surface active and as a result they were not observed to populate the air-liquid interface or to come out of solution and deposit on the Wilhelmy plate. Additionally, these particles have been used in previous studies to visualize flow past superhydrophobic surfaces and have not been observed to affect the flow or adsorb to the air water interface trapped along the superhydrophobic surface [19, 87]. A $5\,\mathrm{mW}$ diode laser and a cylindrical lens were used to generate a laser light sheet and illuminate a plane in the fluid in order to visualize the deformation of the interface. The solid substrate was accelerated from rest to a constant velocity between $2\,\mathrm{mm/s} < U < 200\,\mathrm{mm/s}$ which corresponds to capillary number range between $10^{-5} < Ca < 0.3$ depending on fluid properties.

The dynamic contact angles were determined by analyzing the high-speed video images as seen in Figure 4 using the program ImageJ. The angles were measured manually by first digitally zooming into the image by a factor of five and then fitting a line through roughly the first 500μm of the interface. Multiple measurements at each flow condition were taken and a statistical analysis performed. For the smooth PTFE surfaces, the uncertainty of the averaged experimental measurements was ±1º. While for the superhydrophobic surfaces, the uncertainty was found to be a little larger at ±3º due to the added noise associated with the unsteadiness of the contact line moving along a rough, partially wetting surface.

The sensitivity of the measurements to the spatial resolution of the images was studied by varying the optical/digital magnification of the contact line by an order of magnitude and making multiple measurements of the contact angle. No discernible trend in the data was observed with increasing resolution, but a standard deviation in the data at different magnifications of around 1º was found for both the hydrophobic and the superhydrophobic surfaces. Note that the images with the maximum spatial resolution of these experiments contained 30μm square pixels. To insure steady-state was reached in each case, the contact angle measurements were always performed at the mid-point of the substrates. This also aided with measurement consistency especially for the case of the superhydrophobic surface where variation in surface roughness and wettability across the substrate were found to affect the contact angle measurements by as much as 6º.

2.3 Results and Discussion

In Figure 7, the variations of both advancing and receding contact angles are plotted as a function of the capillary number for both the hydrophobic and superhydrophobic surfaces. The advancing contact angles are all plotted against a positive capillary number while the receding contact angles are plotted against a negative capillary number to differentiate the two regimes. To avoid confusion in an already busy figure, the error bars are not superimposed over the data but the value of the uncertainty is quoted in the caption. The dynamic contact angle measurements on the smooth PTFE surface showed a monotonic increase/decrease in the advancing/receding contact angle with increasing substrate velocity. At large capillary numbers, the advancing contact angle was found to approach an asymptotic value of $\theta_A = 150^\circ$. This is consistent with measurements in the literature [63].

For these superhydrophobic surfaces, the first deviation from the expected dynamic contact angle behavior that was observed occurred for the advancing contact angle measurements. Within experimental error, the advancing contact angles measured for these superhydrophobic surfaces were found to be insensitive to changes in the velocity of the solid substrate. This was true even at the very highest capillary numbers tested, $Ca \sim 0.2$. From this observation, it is clear that neither the hydrodynamic models nor the molecular theory can describe the advancing contact angles on superhydrophobic surfaces. These measurements, instead, suggest that for superhydrophobic surfaces, the advancing contact angle is independent of contact line velocity.

As seen in Figure 7, the receding contact angle was found to decrease monotonically with increasing capillary number for all the surfaces and fluids tested. On this linear scale, the variation in receding contact angle of the smooth PTFE surface appears very steep and was confined to the low capillary number regime. On the logarithmic scale used in subsequent plots, these data will be expanded and the scaling compared to both hydrodynamic and molecular models of dynamic contact angle. One interesting observation is that the decay in the receding contact angle with increasing capillary number for the superhydrophobic surfaces was significantly slower than for the smooth hydrophobic PTFE surfaces. As a result, due to the limitations of the velocity of the Wilhelmy plate, very little contact angle variation was achieved using water because the accessible capillary numbers were too small. In order to access a higher capillary number range, the glycerin in water and PEO in water test fluids were used because they have significantly higher viscosities than water. The delay in the onset of dynamic contact angle variation and the reduction in the magnitude of variation is likely the result of the reduction in viscous stress due to the presence of the shear-free air-liquid interface trapped within the features of the superhydrophobic surface. Superhydrophobic surfaces are known to produce slip at the wall which can easily result in slip lengths of more than 10μm [24]. Even though this slip length is small in comparison to the macroscopic length scales of this flow, a slip length of ten microns can still result in a significant reduction in the viscous stress, especially in the region of the flow close to the three phase contact line where the shear rate diverges if the no-slip boundary condition is imposed.

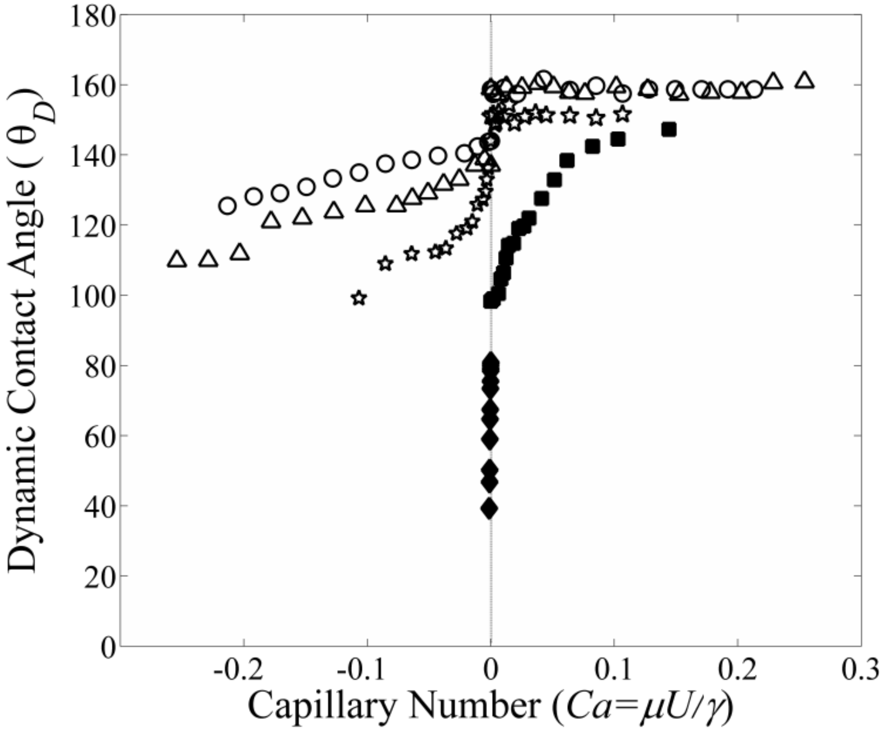

Figure 7: Dynamic contact angle as a function of capillary number. The data include: the superhydrophobic paint surface with (circle) glycerin solution and (triangle) PEO solution; (star) the superhydrophobic PTFE surface with glycerin solution; a smooth PTFE surface with (closed square) PEO solution and (closed diamond) pure water. The smooth PTFE data has an uncertainty of ±1° while the superhydrophobic data has an uncertainty of ±3°.

The effect of reduction in the viscous stress on superhydrophobic surfaces is apparent in the variations of the contact angle hysteresis. The contact angle hysteresis was calculated from the difference between dynamic advancing and receding contact angles and plotted with capillary numbers as shown in Figure 8. The fast decay of the dynamic receding contact angles for the smooth PTFE surface led to a dramatic increase in contact angle hysteresis in the low capillary number regime. For superhydrophobic surfaces, the introduction of regularly patterned or random features and the shear-free interface supported between them can induce a partial-slip boundary condition on the surface. As a result, the onset of changes to the contact angle hysteresis of superhydrophobic surfaces was found to be significantly delayed with the onset moving from $Ca=10^{-4}$ to $Ca=10^{-3}$ or even higher depending on the superhydrophobic surface tested.

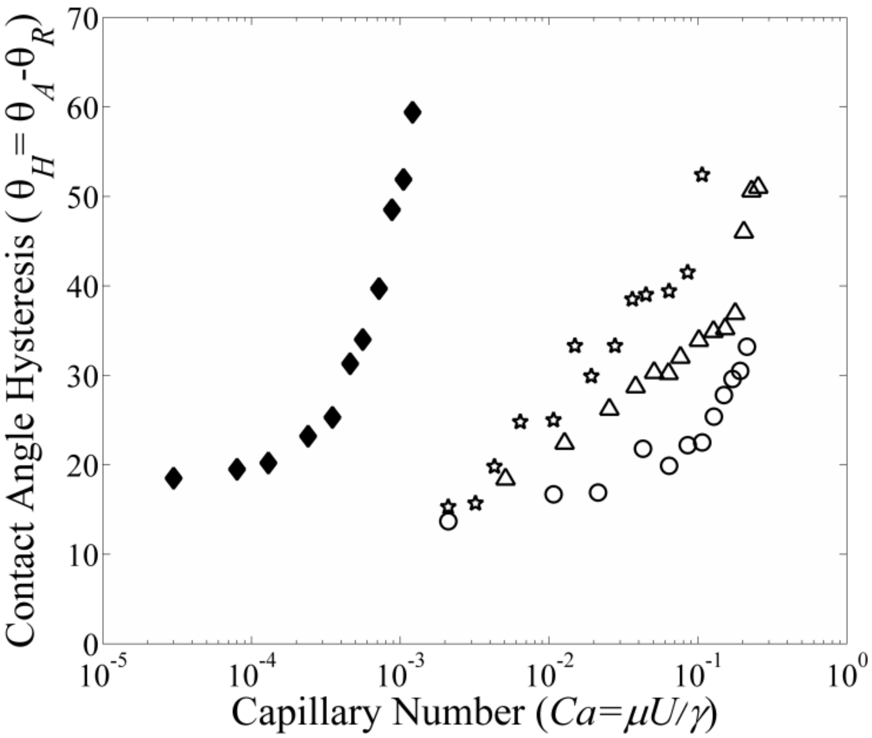

Figure 8: Contact angle hysteresis as a function of capillary number. The data include: the superhydrophobic paint surface with (circle) glycerin solution and (triangle) PEO solution; (star) the superhydrophobic PTFE surface with glycerin solution; a smooth PTFE surface with (closed square) PEO solution and (closed diamond) pure water. The smooth PTFE data has an uncertainty of ±1° while the superhydrophobic data has an uncertainty of ±3°.

To investigate the scaling trends of receding contact angles and to compare to the predictions of the hydrodynamic model in Equation 6, the difference between the cube of the static and dynamic receding contact angles were calculated and plotted against capillary number in Figure 9. The static contact angle of each data set was determined by extrapolation to zero capillary number using a cubic polynomial to fit between five and ten of the lowest capillary number data points. As seen in Figure 9, the receding contact angle data for pure water receding along the hydrophobic PTFE surface was found to scale like ${\theta_{R,s}}^3 - {\theta_R}^3 \propto Ca$ as predicted by the hydrodynamic Cox-Voinov-Tanner scaling law as shown by the fit superimposed over the data in Figure 9. Note that although it is not shown in Figure 9, the advancing contact angle data for smooth PTFE was also found to follow the Cox-Voinov-Tanner scaling law.

In contrast to the smooth PTFE surface, the behavior of the receding contact angle on the superhydrophobic surfaces was found to be more complex. None of the superhydrophobic surfaces tested were well fit over their entire range by the Cox-Voinov-Tanner scaling law. First, we will consider the superhydrophobic painted surfaces. At low to moderate capillary numbers, $Ca < 10^{-2}$, both the PEO and glycerin in water solutions appear to follow the Cox-Voinov-Tanner scaling law. Using Equation 6, with $\alpha = 2\left(\cos\theta_{plate} - \cos\theta_{R,s}\right)/3$ as shown by Eggers [77], it is possible to fit the experimental data in this region and infer a value of the slip length. In this moderate capillary number region, a value of $b = 12\,\mu\text{m}$ in Equation 6 fits both data sets very well. This value of slip length compares well to the direct laminar flow measurements of the slip length for the spray-painted superhydrophobic surfaces that we made using the experimental procedure outlined in Song et al. [24]. In those microfluidics experiments, a value of $b = 10\,\mu\text{m}$ was found for the superhydrophobic painted surface and a value of $b = 6\,\mu\text{m}$ was found for the superhydrophobic PTFE surface.

At a critical capillary number, a transition to a much weaker capillary number dependence in receding contact angle, $\theta_{R,s}{}^3 - \theta_R{}^3 \propto Ca^n$ where $n < 1$, was observed in both cases. For the superhydrophobic painted surface with the glycerin in water solution, the transition was found to occur at a capillary number of $Ca_{crit} \approx 0.02$ while for the PEO in water solution the transition did not occur until a capillary number of $Ca_{crit} \approx 0.08$. In each case a slope close to $n = \frac{1}{2}$, or $\theta_{R,s}{}^3 - \theta_R{}^3 \propto Ca^{1/2}$, was observed. Interestingly, beyond a capillary number of $Ca > 0.1$ the data for both fluids on the superhydrophobic paint surface transition back to a slope of one and the predictions of Cox-Voinov model, but with a much larger slip length of $b = 78\,\mu\text{m}$. The physical origin of this transition at high capillary number to a larger apparent slip length is not obvious. One possibility is that the increased slip length might be evidence of dynamic dewetting from some of the features of the randomly-rough spray-painted superhydrophobic surface.

For the case of the superhydrophobic PTFE surface, no region consistent with the Cox-Voinov-Tanner scaling law was observed. Instead, the data were found to have a consistent slope of $\theta_{R,s}{}^3 - \theta_R{}^3 \propto Ca^{1/3 \pm 0.08}$ or $(\theta_{R,s}{}^3 - \theta_R{}^3)^3 \propto Ca$ over more than two decades of capillary number. Note that the uncertainty reported in the slope is due to the $\pm 3^\circ$ uncertainty in the contact angle measurements. This scaling is also inconsistent with the predictions of the Blake and Haynes molecular kinetics model [83] for which a scaling of ${\theta_{R,s}}^2 - {\theta_R}^2 \propto Ca$ is expected for small capillary numbers. Additionally, this scaling is inconsistent with the effects of inertia for which a scaling of ${\theta_{R,s}}^3 - {\theta_R}^3 \propto Ca^2$ would likely be observed. Each of these theories predicts a dependence of the contact angle on the capillary number of between $\theta_R \propto Ca^{1/2}$ and $\theta_R \propto Ca^{2/3}$ while the data clearly show a much weaker dependence of $\theta_R \propto Ca^{1/9}$.

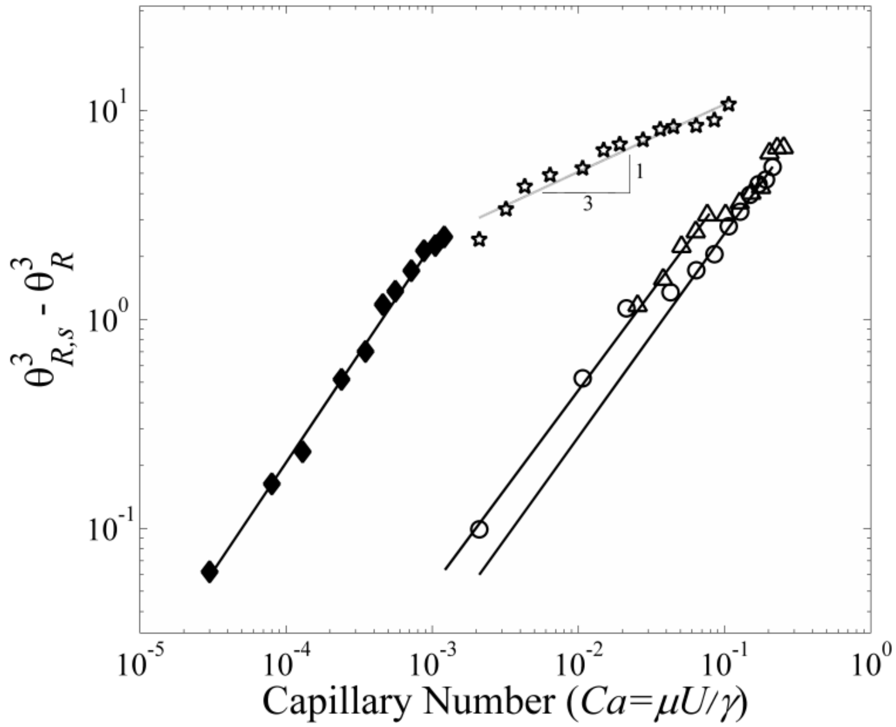

Figure 9: Plot of the difference in the cube of the static receding contact angle and the cube of the dynamic receding contact angle as a function of capillary number. The data include: the superhydrophobic paint surface with (circle) glycerin solution and (triangle) PEO solution; (star) the superhydrophobic PTFE surface with glycerin solution; a smooth PTFE surface with (closed square) PEO solution and (closed diamond) pure water. The smooth PTFE data has an uncertainty of ±1° while the superhydrophobic data has an uncertainty of ±3°. The solid lines represent fits to the Cox-Voinov-Tanner law with different slip lengths. For the superhydrophobic paint surface at low Capillary numbers, both data sets are fit well by a slip length of b=12μm while at large Capillary numbers the data are fit by a slip length of b=78μm.

For the superhydrophobic surfaces, both the hydrodynamic and molecular-kinetic models were able to partially fit the experimental data. However, neither of the two conventional models describes the weak dependence on capillary number observed for the superhydrophobic PTFE surface or the transitions observed for the superhydrophobic paint surfaces at moderate capillary numbers. In order to demonstrate the dependence of dynamic contact angles on the velocity over the entire velocity range, a combined model proposed by Petrov and Petrov [88] was tested. In this model, it is assumed that the static contact angle in the Cox-Voinov hydrodynamic model in Equation 6 is velocity dependent and that an appropriate value for the static contact angle can be obtained from Blake and Haynes' molecular-kinetic equation as shown in Equations 8 and 9.

$$\theta_D{}^3 = [\theta_S(U)]^3 \pm (9\mu U / \gamma)\ln(L/b) \tag{8}$$

$$\theta_S(U) = \cos^{-1}[\cos\theta_{S,0} \mp (2k_B T / \gamma\lambda^2)\sinh^{-1}(U / 2K_\omega\lambda)] \tag{9}$$

Here $\theta_S(U)$ is velocity dependent static contact angle and $\theta_{S,0}$ is the static contact angle at rest. It was found to capable of fitting the experimental data over its entire range as seen in Figure 10. Unfortunately, although the model did fit the data, a physical interpretation of the variation in the model fit parameters could not be inferred from the data. For each case, best fit to the distance of molecular displacement, λ, was of the same order of molecular length, $\lambda \sim 10^{-9} m$. However, for glycerin and polyethylene solutions on same superhydrophobic paint surface, the frequency of adsorption and desorption, K_ω, differed by a factor of about 100. This result implies that the selection of the testing fluid can make different behaviors of dynamic contact angles with capillary number even if each solution has same viscosity and surface tension and was tested on the same superhydrophobic surface. In each case, the slip length used in the combined model was fixed at $b_{SHS} = 78\mu m$. However, it should be noted that equally good fits could be achieved with Petrov's combined model for slip lengths that were unphysical and as large as $b = 250\mu m$. The success of the combined model in capturing the trends in the data suggests that the role of the molecular stress is important for the case of superhydrophobic surfaces and can influence the dynamic contact angle measurements even at relatively large capillary numbers due to the dramatic reduction of the viscous stress resulting from slip.

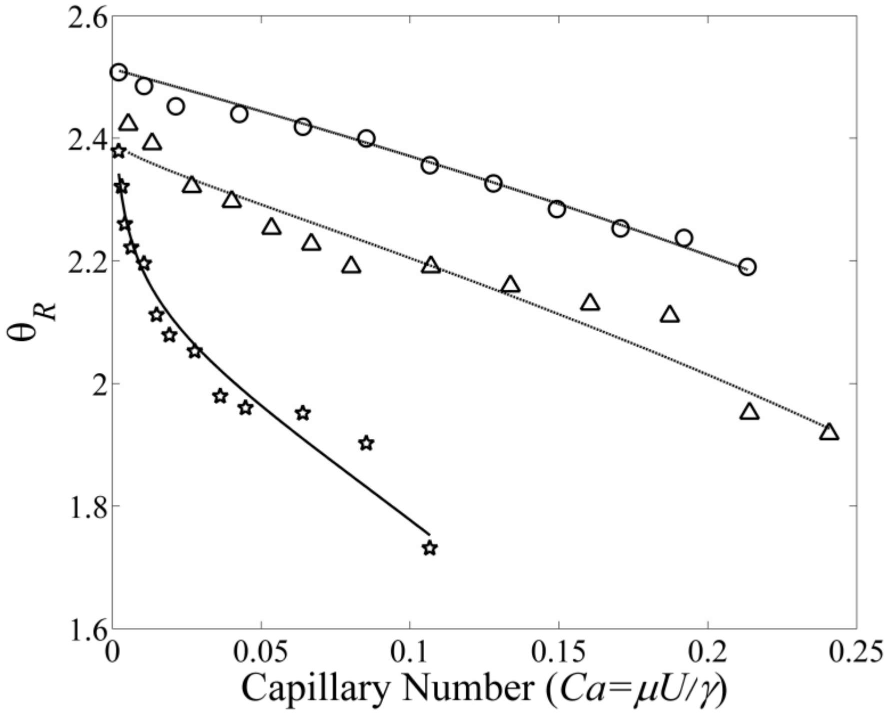

Figure 10: Fitting of the combined model to the receding contact angle as a function of capillary number. The data include: superhydrophobic paint surface with (circle) glycerin solution and (triangle) PEO solution; (star) a superhydrophobic PTFE surface with glycerin solution. The superhydrophobic data has an uncertainty of ±3º. The parameters used are below. For superhydrophobic paint surface with (circle) glycerin solution, λ=7.3*nm*, K_ω=3.4×10^7, *b*=78*µm*. For superhydrophobic paint surface with (triangle) PEO solution, λ=4.7*nm*, K_ω=5.5×10^5, *b*=78*µm*. For a superhydrophobic PTFE surface with glycerin solution, λ=1.41*nm*, K_ω=3.1×10^5, *b*=78*µm*.

Finally, we should note that at the largest capillary numbers reached in these experiments, a transition is often observed from continuous dewetting of the fluid to the deposition of a smooth uniform Landau-Levich film [74]. However, no film was deposited in any of the experiments presented here. All the surfaces were found to be dry upon removal from the liquid bath, although, there has been work that has shown that a very small amount of fluid can be pinched off and remain behind on the top of the features of a superhydrophobic surface as the interface recedes [89]. This is further evidence that the large slip lengths of these superhydrophobic surfaces can dramatically reduce the viscous stresses developed near the contact line which de Gennes [90] showed were responsible for the dynamic wetting transition to film coating at large capillary numbers.

2.4 Conclusions

In this paper, we have performed a series of dynamic contact angle measurements by using a modified Wilhelmy plate method with hydrophobic and superhydrophobic surfaces. The water and aqueous solutions of polyethylene oxide solutions and glycerin solutions were studied in order to vary the liquid's viscosity. The hydrophobic smooth PTFE surface showed significant asymmetry in the dynamic contact angles with respect to the capillary number. However, both the advancing and receding angles were found to follow the hydrodynamic Cox-Voinov-Tanner scaling law, i.e $\theta_{R,s}{}^3 - \theta_R{}^3 \propto Ca$. The dynamic contact angles measured for the superhydrophobic surfaces showed very different characteristics. The presence of microscale structures on the surface of a regularly patterned superhydrophobic PTFE surface and a randomly rough superhydrophobic spray-painted surface resulted in large static advancing and receding contact angles and little static contact angle hysteresis. For all of the superhydrophobic surfaces tested, the advancing contact angles were found to be independent of the capillary number even as the capillary number was driven in excess of $Ca > 0.1$. This observation is a direct result of the reduction of viscous stress at the three-phase contact line caused by from the presence of slip along the superhydrophobic surface. The reduction of viscous stress was also found to have a large impact on the dynamic receding contact angles measured for each of the superhydrophobic surfaces. For the superhydrophobic PTFE surface, the receding contact angle was found to decrease with increasing capillary number, but at a rate that was much weaker than that predicted by the hydrodynamic Cox-Voinov-Tanner scaling law or the Blake-Haynes molecular kinetic theory, $\theta_{R,s}{}^{3} - \theta_{R}{}^{3} \propto Ca^{1/3}$. For superhydrophobic spray-painted surfaces, however, a different behavior was observed. For those surfaces, the dynamic receding contact angles were described well at low capillary numbers by the Cox-Voinov model with a slip length of approximately $b = 12\mu\mathrm{m}$. This slip length closely matches the value independently measured for these surfaces in microfluidic drag reduction experiments. At moderate capillary numbers, a transition to a weaker capillary number dependence was observed similar to the case for the superhydrophobic PTFE surface. Finally, at larger capillary numbers, the data were again found to follow the Cox-Voinov-Tanner scaling law, but with a much larger slip length. For both the superhydrophobic surfaces tested, Petrov and Petrov's combined hydrodynamic-molecular model was found to fit the behavior of the dynamic receding contact angles well over the entire range of capillary numbers observed.

CHAPTER 3

DYNAMIC CONTACT ANGLE MEASUREMENTS OF VISCOELASTIC FLUIDS

3.1 Introduction

The dynamic wetting of a liquid along a solid surface is a phenomenon that occurs in great number of natural and industrially-relevant processes. Over the last few decades, there has been a great deal of research performed, both experimental and theoretical, with the goal of better understanding the dynamic wetting processes over a wide range of flow conditions, and fluid and solid properties [2, 62-64]. Still, there are a number of open questions that remain. In this paper, we will investigate the effect that fluid rheology and specifically viscoelasticity can have on dynamic wetting. We will demonstrate that the addition of fluid elasticity can modify the contact line dynamics and have a great influence on the evolution of contact angle with contact line velocity.

In order to quantify the effect of viscoelasticity on the wetting dynamics of a liquid on a non-deformable solid surface, the shape of the fluid interface can be measured along with the resulting contact angle made between the fluid and the surface. At rest, the contact angle can exist anywhere between the advancing and receding contact angles [2]. For a Newtonian fluid under flow, molecular-level adsorption/desorption processes and macroscopic viscous dissipation can result in an increase in the measured advancing contact angle and a decrease in the measured receding contact angle beyond its static value [2, 62]. The value of the contact angle for a moving three phase contact line is thus not fixed, but is dynamic and, depends in a known way on the velocity of the contact line.

Through experimental measurements and theoretical development, the dependence of dynamic contact angles on the speed of moving contact line has been revealed for both wetting and non-wetting Newtonian fluids [62] as well as a limited subset of shear thinning and weakly elastic fluid [91, 92]. From these results, two different classes of dynamic wetting models have been developed; molecular-kinetic models [83] and hydrodynamic models [71-73]. For the hydrodynamic models, viscous dissipation in the vicinity of the contact line has been shown to lead to a deformation of the fluid interface and a change in the contact angle that scales like $\theta_D{}^3 - \theta_S{}^3 \propto Ca$. This result is known as the Cox-Voinov-Tanner scaling law. Here θ_D is the dynamic contact angle, θ_S is the static contact angle and $Ca = \eta U / \sigma$ is the capillary number where U is the velocity of the contact line, η is the viscosity and σ is the surface tension. Although it is widely accepted, the Cox-Voinov-Tanner scaling law is not universal. It has been observed to fail at extremely low capillary number regime, $Ca < 10^{-4}$, and at very large capillary numbers $Ca > O(0.1)$, where air entrainment, complete coating and the effects of inertia have been observed [81]. In the case of molecular-kinetic models, the energy dissipation by a contact line friction resulting from adsorption and desorption of molecules along the moving contact line is responsible for contact angle changes. In the model of Blake and Haynes [83], the dynamic contact angle varies as $\theta_D = \cos^{-1}\left[\cos\theta_S - \left(2k_B T / \sigma\delta^2\right)\sinh^{-1}\left(U / 2K_\omega\delta\right)\right]$ where k_B is the Boltzmann constant, T is the temperature, δ is adsorption distance of molecules, and K_ω is frequency of molecular displacements.

The common forced wetting techniques used to measure the dynamic contact angles are a capillary tube [63, 93, 94] and a plunge tank [66-68, 95]. For example, using a glass capillary tube, Hoffman [63] measured the dynamic contact angle by displacing Newtonian liquids in the tube filled with air. Petrov et al. [69] and Blake [67, 85] measured dynamic contact angles by plunging a solid surface into a tank of liquid. Using a plunge tank, a Wilhelmy plate or a cylindrical strand of material can be immersed or withdrawn from a reservoir allowing the observer to investigate both advancing and receding contact angles. Additionally, in this technique, the effect of gravity and inertial can typically be neglected and the observer can gain access to the variation of the contact line through high resolution, high speed imaging. For these reasons, we chose the Wilhelmy plate technique to make the dynamic contact angle measurements presented here.

The dynamic wetting of non-Newtonian fluids is of great interest because of its application to a great number of industrial applications involving coating flow. That said, there are only a limited number of papers in the literature investigating dynamic wetting of non-Newtonian fluids, none of which probe the range of Weissenberg numbers, where elasticity becomes dominant, $Wi = \dot{\gamma}\lambda > 1$. Here $\dot{\gamma}$ is shear rate and λ is relaxation time of the fluid. Seevaratnam et al. [96] studied aqueous solutions of xanthan gum with molecular weight of $2\times10^6 g/mol$. At the contact line speeds they studied, the response of their fluids was dominated by shear thinning with negligible impact of elasticity. Shear thinning was shown to reduce the viscous bending of the air-water interface near the contact line. As a result, a weak dependence of the dynamic contact angle on capillary number was found which did not following classic hydrodynamic model, ${\theta_D}^3 \propto Ca$. Prior of the work of Seevaratnam et al. [96], Carre and Eustache [97] studied spreading dynamics of shear thinning fluids in wetting and de-wetting modes and generalized the classic hydrodynamic model to shear thinning non-Newtonian fluids. They revealed that the dynamic contact angles of power law shear thinning fluids does not follow the classic hydrodynamic model, rather it depends on the spreading rate to the shear thinning power law exponent *n* such that, $\cos\theta_s - \cos\theta_D = \frac{K}{\gamma}\left(\frac{U}{\theta_D}\right)^n$. Like Carre and Eustache case, the classic hydrodynamic theory was normally applied to describe the dynamic wetting of non-Newtonian fluid. More recently, Liang et al. [98] developed a model to explain the wetting behaviors of non-Newtonian fluids based on Blake's molecular-kinetic theory. Wei et al. [91] tested Boger fluids which are dilute polymer solutions dominated by elasticity and with negligible shear thinning. They found that the curvature of the advancing air-liquid interface was enhanced, but that the capillary number dependence of the dynamic contact angles was not altered compared to the Newtonian fluids. This is likely because the Weissenberg numbers reached in their experiments were all less than one and as a result large elastic effects are not expected.

In this study, we will present dynamic contact angle measurements of a series of viscoelastic fluids. A hydrophobic surface was used so that both dynamic advancing and receding contact angle measurements can be made. The Wilhelmy plate technique allows us to reach high speed of a testing substrate, making it possible to probe the variation of dynamic contact angles over a wide range of capillary numbers. The test fluids used consists of an extremely high molecular weight aqueous polyacrylamide solution with a relaxation time large enough to make high Weissenberg number experiments possible. We will demonstrate that the dynamic contact angle data at high Weissenberg number do not follow either the expected hydrodynamic or molecular-kinetic scaling even if shear thinning of the fluid viscosity is accounted for. Instead, we will show a much stronger dependence on contact line velocity resulting from the presence of significant elastic stresses in the fluid.

3.2 Experimental Setup

3.2.1 Materials

A series of test fluids were used for this experiment. For Newtonian fluid pure water was used. In addition, polyethylene oxide (PEO, Sigma Aldrich) with 2×10^4 g/mol was used to increase the viscosity of the water without making it viscoelastic. Hereafter, this solution will be designated as Newtonian-PEO solution. For the viscoelastic fluids used in these experiments, two different water-soluble polymers were used. The first was a commercially-available polyacrylamide (PAM) with an extremely high molecular weight (Flopaam 3630, SNF Floerger®) often used in enhanced oil recovery. Solutions with two different concentrations of PAM (0.01 wt and 0.05 wt%) were used in these experiments. As will be shown by detailed rheological measurements, each of the PAM solutions has a large zero shear rate viscosity that shear thins with increasing shear rate, significant fluid elasticity and a large easily-measured relaxation time. A second viscoelastic fluid was tested consisting of an aqueous solution 20wt% of 2×10^4 g/mol PEO and 0.1wt% of a high molecular weight (8×10^6 g/mol) PEO. This Boger fluid was designed to have significant elasticity without shear thinning. Hereafter, this solution will be designated as the viscoelastic PEO solution. All polymer solutions were prepared in deionized water by mixing gently for at least 24 hours at a room temperature to obtain a homogeneous solution. The surface tension of the PEO solution was measured to be 0.06 N/m using a pendant drop experiment and the surface tension of both PAM solutions was measured to be 0.07 N/m.

The steady shear viscosity of each solution was measured using a stress-controlled rotational rheometer (TA, DHR3) with a cone-and-plate geometry. The results are plotted as a function of the applied shear rate in Figure 11. As seen in Figure 11, the viscosity of the viscoelastic PEO solution was found to be constant at $\eta = 0.088 Pa \cdot s$, while the viscosity of the Newtonian PEO solution was slightly lower and measured to be $\eta = 0.064 Pa \cdot s$. At low shear rates, the viscosity of both the 0.01wt% and 0.05wt% PAM solutions were found to exhibit a constant viscosity with value of $\eta_0 = 0.2 Pa \cdot s$ and $\eta_0 = 5 Pa \cdot s$, respectively. Beyond a critical shear rate, the viscosity of both the 0.01wt% and 0.05wt% PAM solutions were found to shear thin with increasing shear rate. The shear thinning of each solution is well described by a power law model such that $\eta = \beta \dot{\gamma}^{n-1}$. The exponent, *n*, was obtained by fitting the power law model to the viscosity data. A value of *n*=0.45 and *n*=0.32 was found for the 0.01wt% and 0.05wt% PAM solution, respectively.

To characterize the viscoelasticity of the PAM solutions and viscoelastic PEO solution, small amplitude oscillatory shear (SAOS) tests were performed using a controlled-stress shear rheometer (TA DHR-3) using a 40mm 2° cone-and-plate geometry at T=20°C. The storage and loss moduli, G' and G'', were measured from high to low frequency, and the measurements were stopped once the terminal regime was reached. From the results presented in Figure 12, the relaxation time, λ, can be inferred from the crossover frequency of the storage and loss modulus, $\lambda = 1/\omega$. The relaxation times of 0.01% and 0.05% PAM solutions were found to be $\lambda = 0.67s$ and $\lambda = 11s$, respectively. Unfortunately, due to the small value of relaxation time for the viscoelastic PEO solution, as seen in Figure 12, a crossover frequency could not be observed within the frequency window tested. Due to the inertia of the aluminum cone used the frequencies that could be probed for the viscoelastic PEO solution were limited to $\omega < 15$ rad/s. The crossover frequency was approximated by fitting storage and loss moduli to a single mode Maxwell model. A reasonable fit to the data could be established for relaxation times of between 0.03s and 0.05s. To double check this approximation, capillary breakup extensional rheology (CaBER) measurements were used to measure the relaxation time of the PEO solution [99, 100]. In CaBER, the relaxation time can be calculated by the rate of decay in the diameter with time. From the CaBER measurements, an extensional relaxation time of $\lambda_E = 0.05s$ was measured suggesting that the upper limit of the relaxation time estimated from the SAOS data for the viscoelastic PEO solution was the appropriate choice.

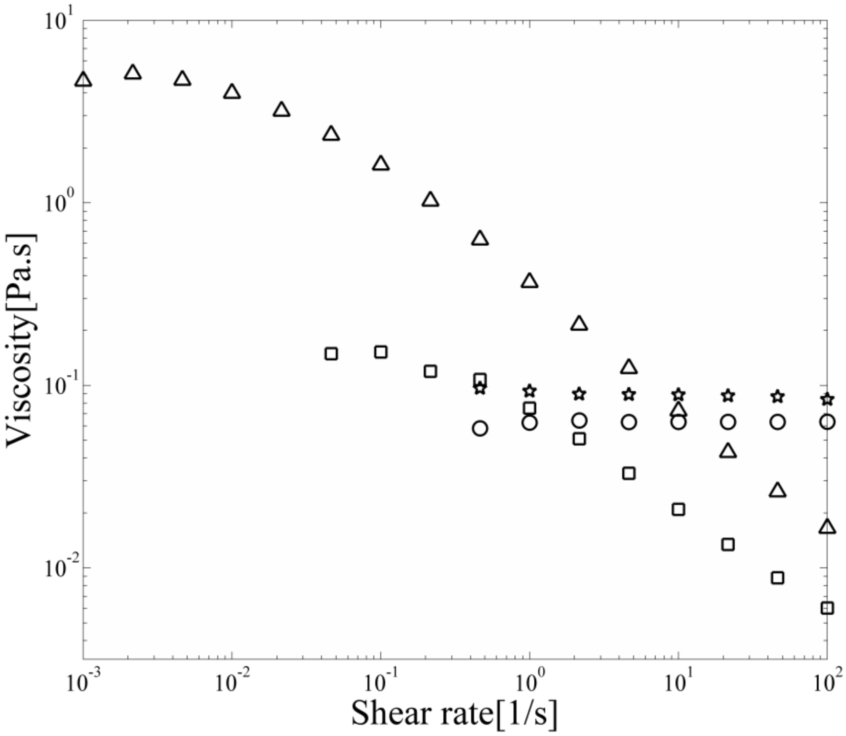

Figure 11: Steady shear viscosity measurements of the test fluids as a function of shear rate. The data include: 0.01wt% PAM solution (square); 0.05wt% PAM solution (triangle); viscoelastic PEO solution (star); and Newtonian PEO solution (circle).

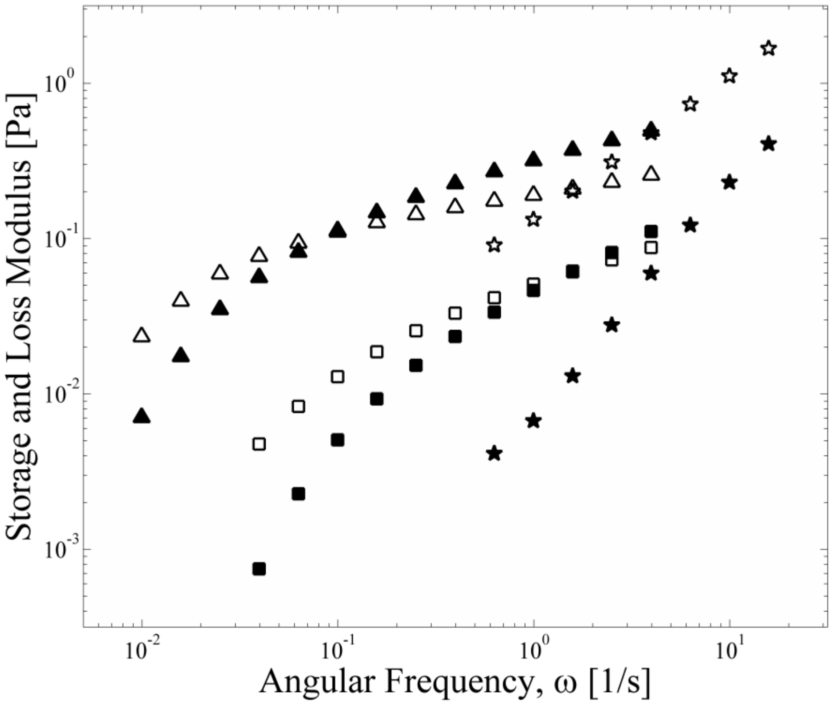

Figure 12: Storage modulus (filled symbols) and loss modulus (hollow symbols) as a function of angular frequency. The data include: 0.01wt% PAM solution (square); 0.05wt% PAM solution (triangle); and viscoelastic PEO solution (star).

3.2.2 Dynamic Contact Angle Measurements

The modified Wilhelmy plate method was used to measure dynamic contact angles of test fluids. A schematic diagram of the Wilhelmy plate technique is presented in Figure 4. To create the Wilhelmy plate, a PTFE sheet (McMaster Carr) with 3cm wide and 6cm tall was attached to an acrylic plate of the same size with epoxy and mounted to a linear motor. The solid substrate was accelerated from rest to a constant velocity between $2\,\mathrm{mm/s} < U < 200\,\mathrm{mm/s}$. Depending on the fluid viscosity, this speed range corresponds to capillary number between $10^{-5} < Ca < 0.3$. For all experiments performed below this upper limit of capillary number, no air was observed to be entrained into the liquid bath during the advancing contact angle measurements. As reported earlier in the literature this can be an issue at large capillary numbers [67].

The test surface was immersed into and withdrawn from a liquid bath. As a result of the large static contact angle of water and these aqueous solutions on the PTFE surface, it was possible to probe both the dynamic advancing and dynamic receding contact angles. The bending of the air-liquid interface near a three phase contact line was recorded by a high speed camera with sampling rate up to 200Hz. A 5mW diode laser and a cylindrical lens were used to generate a laser light sheet perpendicular to the high speed camera. The deformation of the interface was shown effectively by the reflection of the ten micron diameter PIV particles (Sphericel, Potters Industry) added into the liquid. The particles were not surface active and were never observed to come out of solution and deposit on the Wilhelmy plate or affect the dynamic contact angle measurements.

To measure the dynamic contact angles, the high-speed video was analyzed using the program ImageJ. The images imported from the high-speed video were digitally magnified, and the dynamic contact angles were measured by manually fitting a line through roughly the first 500µm of the interface. All the images used for these contact angle measurements had a spatial resolution of 30µm per pixel. As a result, the details of the interface shape and the fluid dynamics very close to the wall in the inner region, where the stress singularity present at the three phase contact line must be relieved through slip or the formation of a precursor film or a number of other alternate mechanisms, could not be resolved with our measurements [64]. Instead, our measurements were limited to the wedge-like flow region outside the inner region where viscous and viscoelastic stresses are still significant and can deform the interface and affect the value of the measured contact angle. To ensure repeatability of our measurements, the sensitivity of the measurements to the spatial resolution of the images was studied by varying the optical/digital magnification of the contact line by an order of magnitude and making multiple measurements of the contact angle. No discernible trend in the data was observed with increasing resolution, but a standard deviation in the data of around 1° was found.

To ensure repeatability of the measurements and that steady-state was reached in each case, the dynamic contact angles were measured at the midpoint of the surface as it was immersed into the liquid. For these low Reynolds number flows, Re<1, in all cases, the flow becomes fully-developed very quickly as can be observed from the video images. However, for the viscoelastic fluids, sufficient time must be provided for the elastic response of the fluid to fully develop. This can be characterized using the Deborah number which is the ratio of the relaxation time of the fluid to the timescale of the flow, $De = \lambda / t$. For $De < 1$, the flow can be considered fully developed. This is the case for all experiments performed with the viscoelastic PEO solution and the 0.01wt% PAM solutions. However, due to its large relaxation time, for some of the high capillary number tests using the 0.05wt% PAM solution, the Deborah number was larger than one and the flow might not be fully developed even though time-resolved images of the contact line show no significant changes in the shape of the contact line past the midpoint of the plate. The uncertainty of the averaged experimental measurements was about ±1.0º for advancing contact angles and ±1.0º for receding contact angles. The error bar will not be included in the graphs, however, so that the variation of dynamic contact angles of all the test fluids can be observed more clearly. Note that the image seen in Figure 4 is the original image imported from the high speed video without modification.

3.3 Results and Discussion

3.3.1 Dynamic Contact Angle Measurements

The variation of advancing contact angles of Newtonian and viscoelastic fluids is plotted as a function of the capillary number as seen in Figure 13. The capillary number compares the relative importance of viscous forces to interfacial forces acting near the three phase contact line between the various liquids and the PTFE surface. Following the work of Carre and Eustache [97], the shear rate dependent viscosity, $\eta(\dot{\gamma})$, used to evaluate the capillary number of viscoelastic fluids. For a power law fluid the capillary number can be written as

$$Ca = \frac{\eta(\dot{\gamma})\,\mathrm{U}}{\sigma} = \frac{\beta\dot{\gamma}^{n-1}\dot{\gamma}L}{\sigma} = \frac{\beta\dot{\gamma}^{n}L}{\sigma} \tag{10}$$

In this equation, the shear rate is defined as $\dot{\gamma} = U / L$ where L is the characteristic length scale of the flow. Note that the choice of the appropriate length scale to use when evaluating the shear rate is not obvious. As one approaches the contact line, the film thickness decreases and, as a result, the shear rate increases, eventually becoming infinitely large at the contact line. As a result, the shear rate dependent viscosity and the first normal stress difference are not uniform throughout the flow, but are in fact a function of distance from the contact line. Here we will use the capillary length $\kappa^{-1} = \sqrt{\sigma / \rho g}$ as the characteristic length scale because it is the only natural length scale to choose. As seen in Figure 13, this choice of characteristic length scale does a reasonably good job of collapsing the data with capillary number as is expected for Newtonian fluids, although there are some important differences in the response of the four fluids can be seen in Figure 13 and will be discussed in detail in subsequent paragraphs.

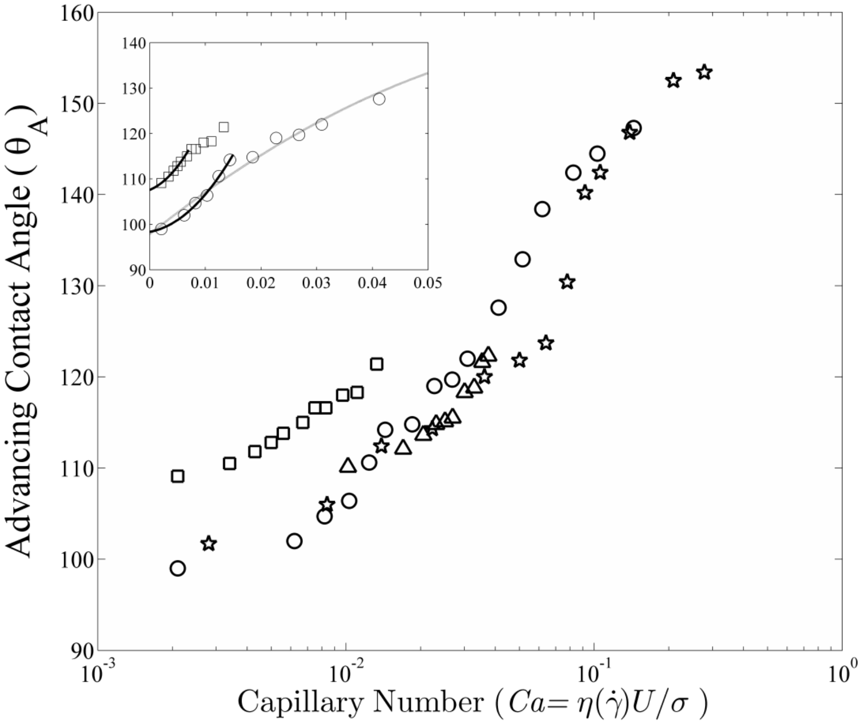

Figure 13: Advancing contact angle as a function of capillary number. Note the shear rate dependent viscosity was used to calculate the capillary number. The data include: 0.01wt% PAM solution (square); 0.05wt% PAM solution (triangle); viscoelastic PEO solution (star); Newtonian PEO solution (circle). Inset shows the several fits to the data using a second order polynomial to illustrate the method used to determine the static contact angle.

The static contact angle of all the fluids on the PTFE studied was determined by extrapolating the initial 5-10 data points to Ca=0 using a second order polynomial as shown in the inset of Figure 13. In this figure, only two dataset were included to clearly show the determination of static contact angles. The coefficient of determination, R^2, which indicates goodness-of-fit was measured to be over 98% in all cases. Depending on the number of data points chosen, a variation in the value of the static contact angle of 1-2° was possible. In the cases of the PAM solutions, the static advancing contact angle of $\theta_{A,s} = 108^\circ$ was found which is roughly 10° larger than the case of Newtonian solution. The Newtonian PEO solution had a static advancing contact angle of 97.8° while the viscoelastic PEO solutions had a static advancing angle of $\theta_{A,s} = 100.4^\circ$.

All fluids tested in Figure 13 shows a monotonic increase in the advancing contact angles with increasing plate velocity. The advancing contact angle was not observed to reach 180°. For the Newtonian and viscoelastic PEO solutions, the data was found to approach a plateau near $\theta_A = 150^\circ$ at the highest capillary numbers tested. A similar plateau was not observed for either of the PAM solutions, however, because the shear thinning of the viscosity and the limitations of the maximum speed of linear motor made it impossible to get to a high enough capillary number to observe the plateau. With increasing fluid elasticity in the two PAM solutions, the expected increase in the advancing contact angles was found to shift to higher capillary numbers. In addition, there are details hidden in the data presented in Figure 13 that are difficult to observe because of the log scale and choice of axis. For instance, the slope of the variation of the advancing contact angles appears to grow with increasing fluid elasticity. This is perhaps most obvious for the case of high molecular weight PEO solution which shows on upturn in the data around $Ca \approx 0.07$. Because this viscoelastic fluid has a constant viscosity, the observed deviation from the expected general response of a Newtonian fluid and the specific response of the Newtonian PEO solution also shown in Figure 13 suggests that the upturn in the data is likely a direct result of the fluid's elasticity.

To better understand this transition in dynamic contact angle variation, the advancing contact angles of all three viscoelastic fluids were plotted as a function of Weissenberg number, $Wi = \dot{\gamma}\lambda$, in Figure 14. The Weissenberg number compares the relative importance of elastic and viscous stresses. For $Wi > 1$, elastic stresses are important while, for $Wi < 1$, viscous stresses dominate the flow. As can be observed in Figure 14, the sharp transition of the advancing contact angles of viscoelastic PEO solution occurs at a Weissenberg number of approximately one, $Wi \approx 1$, where the elastic effect of the fluid begin to become important in the flow. For both the viscoelastic PAM solutions, the Weissenberg number was much larger than one, $Wi \gg 1$. As a result, for both these solutions, elasticity should be important over the entire velocity range and no obvious transition from viscous to elastically-dominated flow was observed with increasing Weissenberg number.

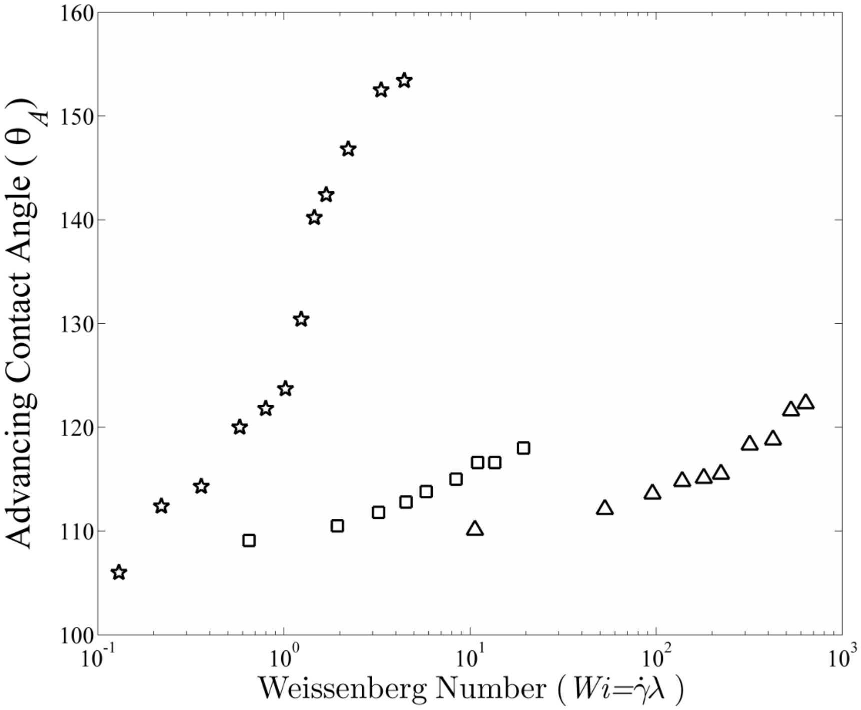

Figure 14: Advancing contact angle as a function of Weissenberg number. The data include: 0.01wt% PAM solution (square); 0.05wt% PAM solution (triangle); viscoelastic PEO solution (star).

Next, the scaling behaviors of advancing contact angles was investigated and compared to the classic hydrodynamic and molecular kinetic models. In Figure 15, the difference between the cube of dynamic advancing contact angles and static contact angles were plotted as a function of capillary number. As expected, the scaling behavior of the advancing contact angles of the PTFE surface was found to follow Cox-Voinov-Tanner's scaling law, ${\theta_A}^3 - {\theta_{A,s}}^3 \propto Ca$, at low to moderate capillary numbers before approaching an asymptotic value at large capillary numbers. The Cox-Voinov-Tanner scaling law is represented by a line of slope one in the log-log plot presented in Figure 15.

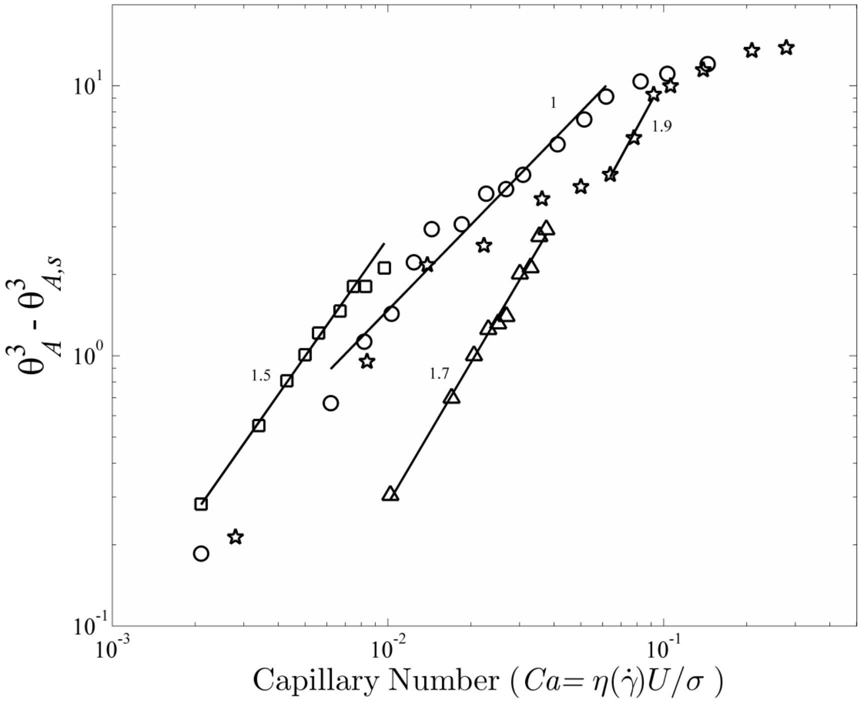

Figure 15: The difference in the cubes of dynamic and static advancing contact angles as a function of capillary number so that the scaling trends can be observed. Note that for Tanner's law, ${\theta_A}^3 - {\theta_{A,s}}^3 \propto Ca$. The data include: 0.01wt% PAM solution (square); 0.05wt% PAM solution (triangle); viscoelastic PEO solution (star); Newtonian PEO solution (circle).

Unlike Newtonian solutions, a very different scaling behavior was observed in the case of the viscoelastic solutions. For both PAM solutions, a deviation from the prediction of Cox-Voinov-Tanner's law was observed. As the Weissenberg number increased with the fluid elasticity, a slope close to $\theta_A{}^3 - \theta_{A,s}{}^3 \propto Ca^2$ was observed. For the 0.01wt% PAM solution, the advancing contact angle was found to scale like $\theta_A{}^3 - \theta_{A,s}{}^3 \propto Ca^{1.5\pm0.15}$, while for the 0.05wt% PAM solution it was found to scale like $\theta_A{}^3 - \theta_{A,s}{}^3 \propto Ca^{1.7\pm0.15}$. The uncertainty in the slope was calculated by performing a propagation of error analysis given the uncertainty of both the measured advancing contact angle and the static contact angle. As we will discuss in detail later, this scaling make intuitive sense as the flow-induced elastic stresses should be proportional to the square of the shear rate, $\dot{\gamma}^2$, and as a result proportional to the square of the velocity, $\dot{\gamma}^2 \propto U^2$. For the viscoelastic PEO solution, interesting transition in the scaling behavior was observed. As can be observed from Figure 15, before reaching $Wi = 1$, where fluid elasticity begins to become important in the flow, the scaling behavior of the advancing contact angle was found to follow the response of a Newtonian fluid, $\theta_A{}^3 - \theta_{A,s}{}^3 \propto Ca$. For $Wi > 1$, however, a slope close to $\theta_A{}^3 - \theta_{A,s}{}^3 \propto Ca^2$ was observed. This transition in the data is further evidence supporting our hypothesis that fluid elasticity can have a significant impact on the variation of the dynamic contact angle.

In Figure 16, the variation of the receding contact angles for all four test fluids on the PTFE surface is shown. The static receding contact angle was calculated in the same manner as the static advancing contact angle above with examples of the second order polynomial fits superimposed over Newtonian solution and 0.01wt% PAM solution data presented in inset of Figure 16. The static contact angle of Newtonian solution was found to be 80.8º while the static contact angle of viscoelastic PEO solution was found to be 82.3º. The static receding contact angles were found to be $\theta_{R,s} = 85^\circ$ and $\theta_{R,s} = 88.5^\circ$ for the 0.01wt% and 0.05wt% PAM solutions, respectively. For all fluids tested, the receding contact angles were found to decrease monotonically with increasing plate velocity. As was the case for the dynamic advancing contact angle, the Newtonian fluid's response is well predicted by the hydrodynamic model. However, the variation of the receding contact angles was confined to very narrow capillary number regime compared to that of the advancing contact angle.

Two interesting phenomena were observed for the viscoelastic fluids. First, the onset of decay in the receding contact angles was delayed to higher capillary number regime with increasing fluid elasticity. Unlike the advancing case, this delay is quite dramatic even when the shear thinning of the viscosity is accounted for as it is in Figure 16. This result indicates that fluid elasticity hinders the viscous bending of the air-water interface when the fluid recesses. Second, the delay in capillary number for the onset of receding contact angle variation appears to be quite sensitive to the elasticity of the fluid. Increasing from 0.01wt% to 0.05wt% PAM was found to shift the data to higher capillary numbers by more three decades. Unfortunately, unlike the advancing case, where measurements of the PEO solution crossed $Wi = 1$ and a distinct transition could be observed, in the receding case, flow rates surpassing $Wi > 1$ could not be reached for the PEO solution. As such, no distinct flow transition was observed for the PEO. All measurements for the two PAM solutions were for $Wi > 1$ where elastic effects are expected to be important.

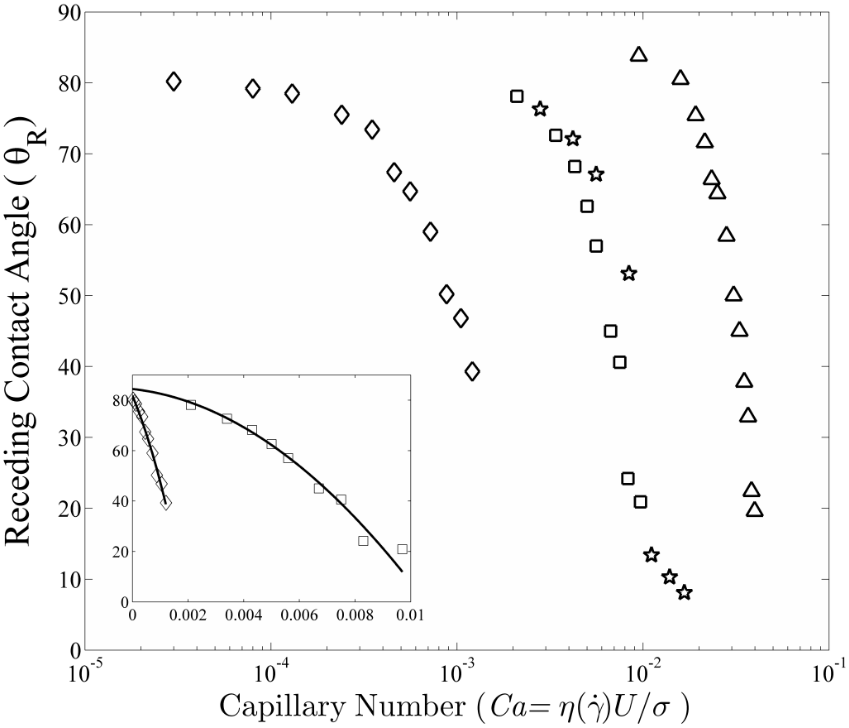

Figure 16: Receding contact angle as a function of capillary number. The data include: 0.01wt% PAM solution (square); 0.05wt% PAM solution (triangle); viscoelastic PEO solution (star); pure water (diamond).

The scaling behavior of the receding contact angle were studied by plotting the difference between the cube of dynamic receding contact angles and the cube of static receding contact angles, ${\theta_{R,s}}^3 - {\theta_R}^3$, against the capillary number. As seen in Figure 17, the prediction of the Cox-Voinov-Tanner's law, ${\theta_{R,s}}^3 - {\theta_R}^3 \propto Ca$, fits the data for the Newtonian fluid over the entire capillary number range. For the viscoelastic PEO solution, the receding contact angle was found to scale like ${\theta_{\mathrm{R},s}}^3 - {\theta_R}^3 \propto Ca^{1.1\pm0.1}$. This scaling is not obviously deviated from the response of Newtonian solutions, indicating that the effect of elasticity was not apparent in the receding contact angle for the viscoelastic PEO solution because as we noted before, the Weissenberg number never becomes greater than one. However, even though no change was observed in scaling with capillary number, a significant delay in the onset of changes to the receding contact angles were observed for the viscoelastic PEO solution. A similar delay was not observed for the advancing contact angle measurement and the cause of this shift remains an open questions. It should be pointed out, however, that although we are representing each flow with a single Weissenberg number based on the shear rate evaluated with the plate velocity and the capillary length, the shear rate is not constant throughout the flow field. In fact, as one approaches the contact line, the shear rate blows up to infinity. In fact, the shear rates are so large near the contact line that it is possible that the viscoelastic PEO solutions, which the rheology measurements presented in Figure 11 show to have a constant viscosity up to shear rates of $100\mathrm{s}^{-1}$, could in fact be shear thinning at still higher rates. As a result, even though Weissenberg number as we have defined it here is less than one, there are regions close to the contact line where elasticity and shear thinning can still become important perhaps causing the delays in the onset of receding contact angle changes observed here.

As observed in advancing contact angle cases, the scaling behavior of the receding contact angle of each the viscoelastic PAM solution was found to deviate from the prediction of Cox-Voinov-Tanner's law. As to the case of the advancing contact angle, the scaling for the viscoelastic fluids approached $\theta_A{}^3 - \theta_{A,s}{}^3 \propto Ca^2$. With increasing fluid elasticity the resulting scaling increased from $\theta_{\mathrm{R},s}{}^3 - \theta_R{}^3 \propto Ca^{1.2\pm0.1}$ for 0.01wt% PAM solution to $\theta_{\mathrm{R},s}{}^3 - \theta_R{}^3 \propto Ca^{1.7\pm0.1}$ for 0.05wt% PAM solution.

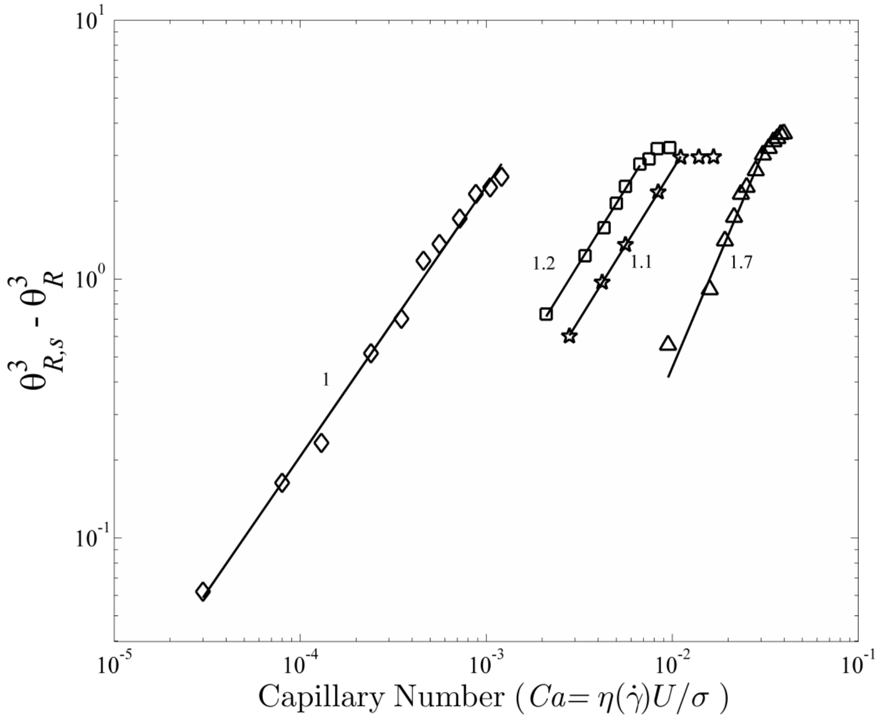

Figure 17: The difference in the cubes of the static and dynamic receding contact angle as a function of capillary number. Note that for Tanner's law $\theta_{R,s}{}^3 - \theta_R{}^3 \propto Ca$. The data include: 0.01wt% PAM solution (square); 0.05wt% PAM solution (triangle); viscoelastic PEO solution (star); pure water (diamond).

3.3.2 Viscoelastic Scaling Analysis

In order to understand the scaling behavior of dynamic advancing and receding contact angles for the viscoelastic fluids, a simple scaling model was developed using a similar approach to Tanner's model. The main difference is of course that the elastic normal stress of the fluid, τ_{xx}, cannot be neglected for the viscoelastic fluids. By introducing the first normal stress coefficient, we can arrange the two-dimensional momentum equation as follows:

$$\frac{dP}{dx} = \frac{\partial \tau_{xx}}{\partial x} + \frac{\partial \tau_{yx}}{\partial y} = \frac{\partial}{\partial x}(\psi_1 \dot{\gamma}^2) + \frac{\partial}{\partial y}(\eta \dot{\gamma}) + \frac{\partial \tau_{yy}}{\partial x} \tag{11}$$

where dP/dx is the pressure gradient, $\psi_1(\dot{\gamma}) = (\tau_{xx} - \tau_{yy})/\dot{\gamma}^2$ is first normal stress coefficient, $\dot{\gamma}$ is the shear rate, and u is the velocity of the main flow direction (x-direction). Here we assume that variations of the normal stress, τ_{yy}, are small compared to variations in the normal stress, τ_{xx}, allowing us to neglect the last term in Equation 11. Using a dimensional analysis, a scaling for dynamic contact angle can be derived from Equation 11 for a viscoelastic fluid. For the viscoelastic fluids studied here, both the first normal stress coefficient and the viscosity can modeled using power law equations $\psi_1 = \alpha \dot{\gamma}^{m-2}$ and $\eta = \beta \dot{\gamma}^{n-1}$, with different power, law dependence, *m* and *n*, on the shear rate. Here, $\alpha\left[\mathrm{Pa \cdot s^m}\right]$ and $\beta\left[\mathrm{Pa \cdot s^n}\right]$ are indices that set the magnitude of the normal stress and viscosity of the power law fluid. Substituting into Equation 11 and differentiating we get

$$\frac{dP}{dx} = \alpha m \dot{\gamma}^{m-1} \frac{d\dot{\gamma}}{dx} + \beta n \dot{\gamma}^{n-1} \frac{d\dot{\gamma}}{dy} \tag{12}$$

By non-dimensionalizing Equation 12 using characteristic variables, x_c, y_c, U and p_c we get

$$\frac{P_c}{x_c}\frac{d\bar{P}}{d\bar{x}} = \alpha m\left(\frac{U}{y_c}\right)^m \frac{1}{x_c}\frac{d}{d\bar{x}}\left(\frac{d\bar{u}}{d\bar{y}}\right)^m + \beta n\left(\frac{U}{y_c}\right)^n \frac{1}{y_c}\frac{\partial}{\partial\bar{y}}\left(\frac{d\bar{u}}{d\bar{y}}\right)^n \qquad (13)$$

Because all dimensionless quantities, represented by variables with an over bar, are by definition order one in magnitude we can conclude that

$$\frac{P_c}{x_c} = \pm\frac{\alpha_1 m U^m}{{y_c}^m x_c} + \beta_1 n\frac{U^n}{{y_c}^{n+1}} \qquad (14)$$

Here α_1 and β_1 are fitting constants that are not necessarily the same as α and β, but should be of the same order of magnitude. The non-dimensional pressure variable can be assumed to the Laplace pressure at the air-liquid interface, $P_c \propto \sigma(\frac{1}{R_1}+\frac{1}{R_2}) \approx \sigma\frac{d^2y}{dx^2}$. In addition, for small contact angles the slope of the interface, y_c / x_c, can be represented to the dynamic contact angle, θ_D. The result is a scaling for dynamic contact angle of viscoelastic liquids.

$$\theta_D{}^3 = \pm\frac{\alpha_1 m U^m}{\sigma {y_c}^{m-1}}\theta_D + \frac{\beta_1 n U^n}{\sigma {y_c}^{n-1}} \qquad (15)$$

The power law dependence capillary number of the viscosity, *n*, and first normal stress coefficient, *m*, were taken from the rheological measurements presented in Figure 11 and Figure 12. Because of the low elastic normal forces produced by these samples in steady shear, the first normal stress coefficient was estimated from the linear viscoelasticity measurements using Cox-Merz Rule, $\psi_1 \approx 2G^{'} / \omega^2$. The result was a power law scaling of $\psi_1 = 0.01\dot{\gamma}^{-1.2}$ and m = 0.8 and $\eta = 0.07\dot{\gamma}^{-0.55}$ and n=0.45 for the 0.01wt% PAM solution, and a power law scaling of $\psi_1 = 0.62\dot{\gamma}^{-1.5}$ m = 0.5 and $\eta = 0.36\dot{\gamma}^{-0.68}$ and n=0.32 for the 0.05wt% PAM solution.

To validate this model, the predictions of Equation 15 were superimposed over the measurements of the difference between the cube of dynamic receding contact angles and the cube of static receding contact angles for the PAM solutions in Figure 18. The viscoelastic scaling model predicts the scaling of the dynamic contact angles for the limiting cases of a Newtonian fluid, $\theta_D{}^3 - \theta_{D,s}{}^3 \propto Ca$, and a elasticity-dominated fluid with a constant first normal stress coefficient, $\theta_D{}^3 - \theta_{D,s}{}^3 \propto Ca^2$. For the viscoelastic fluids tested here, the data resides somewhere between these two limits. For the case of the dynamic advancing contact angle, the scaling model does a nice job of fitting the experimental data over the entire range of capillary number for both the 0.01wt% and the 0.05wt% case. The only exception is within the region at high velocities where the contact angle approached the asymptotic value. For the receding case, the scaling model also fits the data very well, especially at high velocities. Some deviation at low velocities can be seen. This is could be due to the uncertainty with which the static receding contact angle can be quantified. There is a $\pm 1^\circ$ uncertainty in the data which becomes more significant at low velocities when there is only a small deviation from the static contact angle. Or, alternatively, it could be because the data is so close to 90° that the small angle assumption that has been used breaks down. Finally, if we compare the predictions of our scaling model to that of Carre and Eustache, which only takes shear thinning effect into consideration, the fit from our model is significantly better. The model of Carre and Eustache cannot match the slope of either the dynamic advancing or receding contact angle when fluid elasticity is important. Note a fit to the dynamic contact angle data of the viscoelastic PEO solution was also attempted using the simple scaling model. Unfortunately, the rheological measurements of this fluid were not sufficient enough to allow it to be fit by a power law fluid. What is clear is that a more sophisticated model needs to be developed if one wishes to predict the dynamic contact angle for a fluid across the transition from low to high Weissenberg numbers observed for the viscoelastic PEO case.

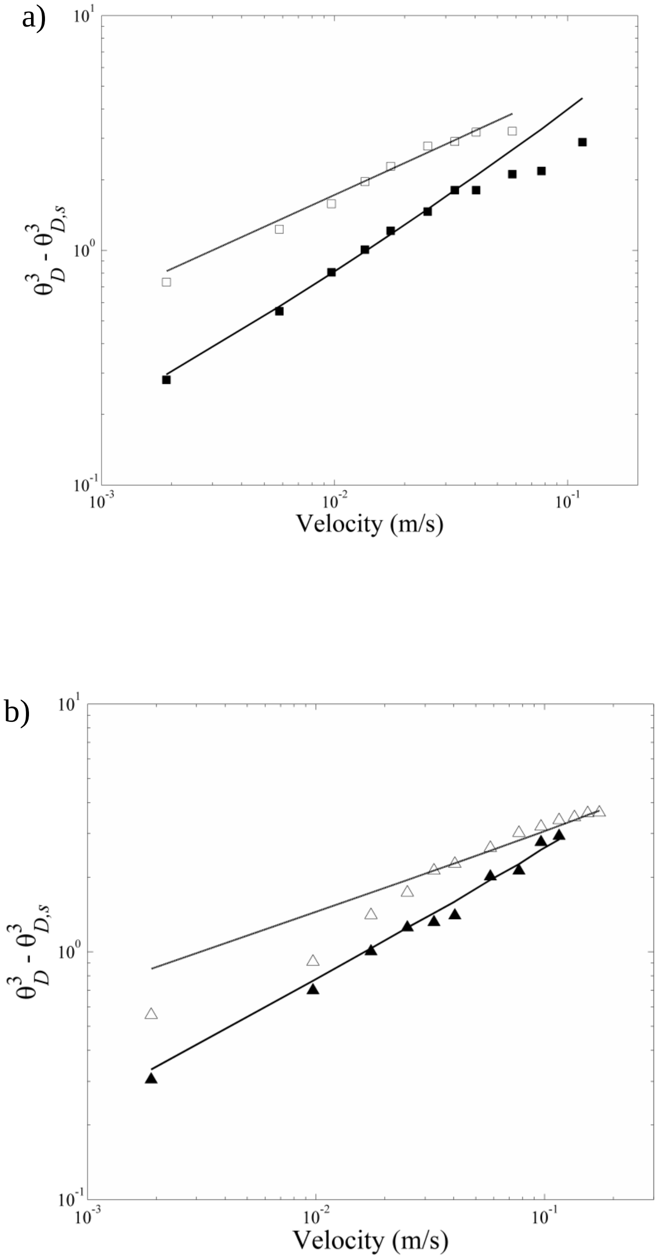

Figure 18: The difference in the cubes of the static and dynamic receding contact angle as a function of plate velocity. The experimental data include (a) advancing (filled square) and receding (void square) contact angles for the 0.01wt% PAM solution and (b) advancing (filled triangle) and receding (void triangle) contact angles for 0.05wt% PAM solution. Superimposed over the data is the theoretical prediction of Equation 15.

3.4 Conclusions

In this study, the dynamic advancing and receding contact angles of viscoelastic fluids were measured through the use of a modified Wilhelmy plate technique. A PTFE surface was used as the testing surface. Aqueous polyethylene oxide and polyacrylamide solutions with different fluid elasticity were prepared as test fluids. The advancing contact angles of both the Newtonian and viscoelastic solutions were found to increase with increasing plate velocity, while the receding contact angles were found to decrease with increasing plate velocity. However, significant differences were observed in the variation of the dynamic contact angles with capillary numbers between the Newtonian solution and viscoelastic solutions. Fluid elasticity was found to delay the onset of variation of dynamic contact angles to the higher capillary numbers. In addition, the dynamic contact angles of viscoelastic fluids were found to scale like $\theta_D{}^3 - \theta_{D,s}{}^3 \propto Ca^2$. This is a significant departure from the scaling of the dynamic contact angles of the Newtonian solution which were found to follow Cox-Voinov-Tanner's hydrodynamic scaling law, $\theta_D{}^3 - \theta_{D,s}{}^3 \propto Ca$. The effect of fluid elasticity becomes more transparent when the data was recast in terms of the Weissenberg number. A transition in the growth of the advancing contact angle was observed at $Wi = 1$, above which, the fluid elasticity becomes important in the flow. Below $Wi < 1$, where viscous stresses dominate the flow, the variation in dynamic advancing contact angles was found to scale like $\theta_D{}^3 - \theta_{D,s}{}^3 \propto Ca$, in agreement with the prediction for a Newtonian fluid. For $Wi > 1$, where elastic effects are important, the variation of advancing contact angle was found to scale like $\theta_D{}^3 - \theta_{D,s}{}^3 \propto Ca^2$. A simple scaling model was developed to predict scaling behaviors of the dynamic contact angles of viscoelastic fluids. This model was capable of describing the behavior of the dynamic contact angles well over a wide range of plate velocities.

CHAPTER 4

ROLE OF INTERFACE SHAPE ON THE LAMINAR FLOW THROUGH AN ARRAY OF SUPERHYDROPHOBIC PILLARS

4.1 Introduction

As a solid object moves through a fluid, it will invariably experience a resistance force or a drag. Drag increases operational cost of airplanes, automobiles and pipelines. As a result, reducing drag in fluid flow has been one topic of study in the field of fluid dynamics. In internal flows like those through pipes, for example, a number of different strategies have been utilized to reduce the shear stress along the pipe wall including the addition of high molecular weight polymers to the flow [101], the injection of air bubbles near the surface of the pipe [102, 103], and the introduction of small-scale structures to a hydrophobic wall to make it superhydrophobic and to trap air along the surface of the pipe [18, 20, 22]. Among those methods, the use of superhydrophobic surfaces for drag reduction has been spotlighted over the last two decades [15] and will be the focus of this paper.

The drag reduction produced by a superhydrophobic surface depends on the dimensions of the pipe or channel, the fraction of the superhydrophobic surface covered by an air-water interface, and the size and spacing of the surface features [15, 18, 24, 31]. Maximum drag reduction is achieved with decreasing channel height, increasing air-water interface coverage and larger feature spacing [18]. The existence of a non-zero slip velocity at the air-water interface has been demonstrated through micro PIV (µPIV) measurements and numerical simulations [19, 44]. In most previous studies, the air-water interface trapped within the superhydrophobic surface was assumed to be flat. However, at large flow rates and pressures, the interface can be deformed and eventually driven into the surface features and lost. Thus, understanding the role of interface shape on the performance of superhydrophobic surfaces is extremely important if the performance of the surfaces is to be fully optimized.

The theoretical deflection of the air-water interface can be determined by the difference in the static pressure between the water and the air phases and spacing between surface roughness, $P_{water} - P_{air} = 2\sigma_w \cos(\pi - \theta)/l$ [15]. Here, σ_w is surface tension of the water, l is spacing between surface roughness, θ is deflection angle of the interface from the flow direction, and the deflection is assumed to drive the interface into a circular hole. As the static pressure in the water phase is increased through an increase in the flow rate and/or a decrease in the channel height, the deflection angle of the interface increases but remains pinned to the top of the surface roughness until it reaches the local advancing contact angle. As a result, the air-water interface is driven further and further into the surface as pressure in the water compresses the air phase, giving the interface a concave shape. At a large enough water pressure, the advancing contact angle is reached and the air-water interface collapses, eliminating the drag reducing properties of the superhydrophobic surfaces. Conversely, a convex interface shape can also be achieved by decreasing the static pressure of the water phase or increasing the static pressure of the air phase.

In laminar flows, it has been shown that the continuity and shape of the air-water interface is an important factor in drag reduction. Steinberger *et al*. [104] used a modified SFA to investigate the hydrodynamics of a water glycerol mixture confined between a sphere and a superhydrophobic surface containing a square array of $d = 1.3\mu\text{m}$ holes to form a ‘bubble mattress’. Isolated bubbles have been shown both experimentally and numerically to perform relatively poorly for drag reduction because the air-water interface that is formed is not continuous along the surface and large slip velocities cannot be obtained [105]. The experimental measurements of Steinberger *et al*. [104] actually showed that a larger slip length was achieved for the hydrophilic, fully-wetted holes in the Wenzel state, $b \approx 105\text{nm}$, then the hydrophobic Cassie state, $b \approx 20\text{nm}$. To understand why, the authors performed a series of numerical simulations where they studied the effect of interface shape on the resulting slip length. They found that the maximum drag reduction was achieved when the air-water interface supported above the holes was flat and dropped off quite significantly for menisci that protruded into the flow or into the holes. The theoretical predictions of Sbragaglia *et al*. [106] found similar results for the flow past microridges supporting deformed interfaces. Steinberger *et al*. [104] showed that it is the immobility of the air-water interface and the resulting blockage of the flow that combine to actually enhance drag for bubbles protruding beyond the hole at an angle greater than $\theta > 60°$. These results are in agreement with Richardson’s early predictions [107] that the proper macroscopic boundary condition to use for a perfectly shear-free surface will become no-slip if the surface is sufficiently rough. To date, no experiments have been performed to confirm these results for superhydrophobic surfaces which produce significant drag reduction like arrays of microridges or microposts where the interface is mobile, however, work with bubble matrices has contributed to evolve experimentally.

Tsai et al. [44] experimentally measured the shape of the air-water interface using confocal microscopy. Through micro PIV measurements, they found that a concave air-water interface reduces the slip length from that measured on a flat interface [44]. Their follow-up research demonstrated the role of the interface geometry on the slippage over a wide range of protrusion angle from a bubble mattress [45]. An active control of the static pressure within the air phase was used to modify the protrusion angle of the interface. A maximum drag reduction of 21% and an equivalent slip length of 5μm were obtained at the protrusion angle of 10° [45]. This slip length decayed quickly for protrusion angles beyond 10°. In this study, the channel height was large enough that the additional confinement effects due to the protrusion of the bubbles into the channel were small.

In this paper, we will systematically change the air-water interface shape of superhydrophobic pillars in the microchannel by controlling the static pressure in the channel. Direct measurements of the pressure drop and velocity vector field for the flow around superhydrophobic pillars will be presented for various interface shapes. These measurements will allow us to better understand and optimize the performance of superhydrophobic surface.

4.2 Experimental Setup

A schematic diagram of the microfluidic device is shown in Figure 19. The microchannels were produced with regular array of circular and apple-core-shaped superhydrophobic pillars which bridge across the microchannel to create a microfluidic porous media. The microchannels were designed using AutoCAD and a close up of the pillar cross sections are shown in Figure 19c and 19d. Each of the pillar design start from a circular cross-section with a diameter of D_0 =150μm, are spaced 375μm apart and are equal in height to the microchannel at H=62 μm. As seen in Figure 19c, the circular cross section pillar is fully wetted by the water and will be used as the control. To make superhydrophobic pillars, a number of different geometries were tried including ‘x’ shaped and ‘+’ shaped pillars. The apple-core design seen in Figure 19d was converged upon because of the ease of creating individual trapped bubbles along the side walls of the pillars during the initial filling of the microchannel and the longevity of the bubbles in this design. The bubbles happened on the side of the apple-core-shaped pillars were found to last for a full set of day long experiments without the need to replenish. To create the apple-core-shaped pillar, a circle of diameter, 35μm, was cut from each size of the circular pillar with the center of the cut out located at a position 47μm from the center of the circle. The apple-core-shaped pillars were then aligned so the shear-free air-water interface would be placed in the contraction between pillars where the maximum effect would produce. The microfluidic device designs were then printed on a high-resolution mask at 20,000 dpi to allow for resolution of features as small as 10μm. A negative of the mask was transferred to a photoresist (SU-8 2100, MicroChem) spun coat onto a silicon wafer using a mask aligner (SUSS MicroTec MA6). To form the final microfluidic devices, a casting from the master was created in polydimethylsiloxane (PDMS) (Dow Sylgard 184) [18, 40], removed from the master and bonded to a microscope glass spun coat with a thin layer of partially cured PDMS [108] before a final bake at 60°C overnight created an excellent seal.

An inlet and multiple outlets were incorporated into the design at the ends of the channel as seen in Figure 19a so that the working fluid could be driven through the device using a syringe pump. Distillated water was used as the working fluid in all experiments presented here. Four pressure ports were incorporated to read the pressure at multiple locations within the microchannel and get accurate pressure drop values. The pressure drops reported here will primarily be from the most upstream and downstream ports. The two pressure ports in the middle were superfluous for pressure drop measurements, but in addition to the three outlet ports, they were extremely useful for removing unwanted air bubbles within the microfluidic device. The static pressure in the microchannel was controlled by changing the pressure drop through the outlet tubing. This was accomplished by manually tightening or loosening a hose clamp. The change in static pressure was used to change the shape of the air-water interface trapped along the superhydrophobic pillar from roughly flat, D/D_0=0.8, to circular, D/D_0=1.0, to convex, D/D_0=1.1. Here, D is the width of the apple-core-shaped pillar measured at the center of the trapped air-water interface. Some variation in the measured size of the trapped air bubbles was observed for the superhydrophobic pillars due to variation in the fabrication process. To minimize error, the diameter of the air bubbles was measured at 50 different superhydrophobic pillars in the microchannel.

All the pressure drop measurements were performed using manometer columns with 0.5mm height resolution and were performed at a fixed volume flow rate of Q=0.1ml/min. This flow rate corresponds to a capillary number of $Ca = \mu U / \sigma$ = 6.6×10^{-5} and a Reynolds number of $Re = \rho U w / \mu$ =0.71. The streamwise velocity between each post in the microchannel, $U_{pillar} = Q / n(w - nD_0)$ =4.75mm/s, was calculated using conservation of mass, and confirmed by micro particle image velocimetry (μPIV).

Here, μ is the viscosity of working fluid, H is the depth of the microchannel, w is the width of the microchannel, n is number of posts, ρ is the density and σ is the surface tension. The depth of the microchannel was measured to be $62.2 \pm 0.1\,\mu\text{m}$ using a surface profilometer. The pressure drop of the apple-core-shaped superhydrophobic pillars was compared to that of the baseline circular pillars to evaluate the effect of air-water interface shape on the pressure drop. The maximum uncertainty of pressure drop was calculated to be 5Pa.

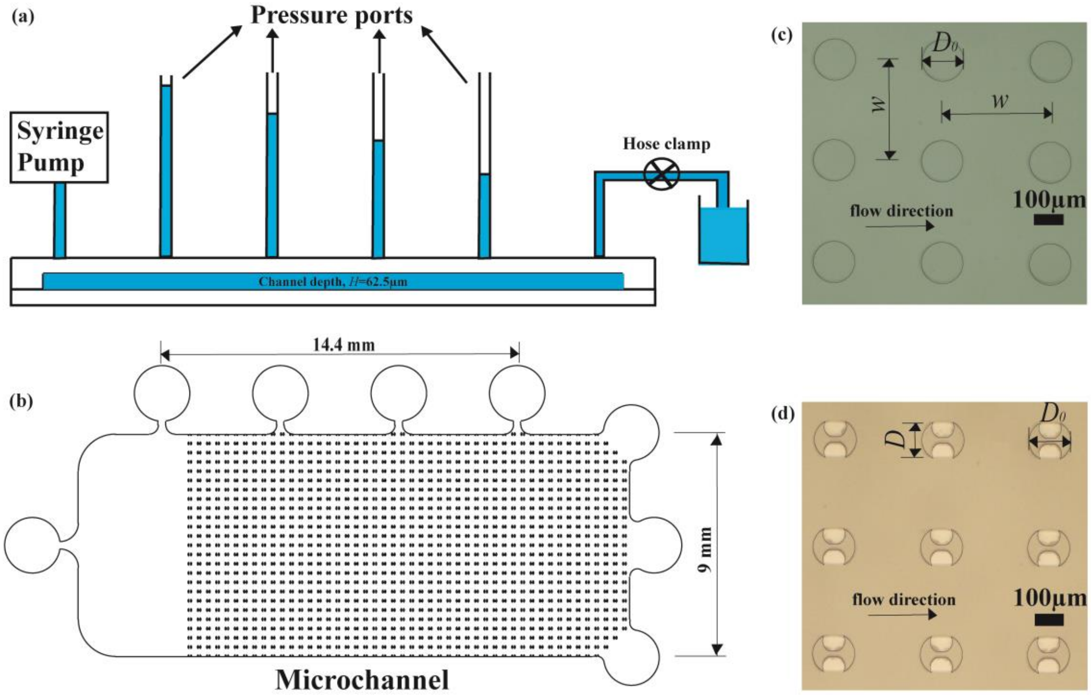
(a)
Pressure ports
Syringe Pump
Hose clamp
Channel depth, H=62.5µm
(c)
D0
w
w
flow direction
100µm
(b)
14.4 mm
9 mm
Microchannel
(d)
D
D0
flow direction
100µm

Figure 19: Schematic diagram of the experimental set up. Also included are (a) schematic diagram for pressure drop measurements, (b) top-down schematic diagram of the microchannel, and optical microscope images of (c) circular pillars and (d) apple-core-shaped superhydrophobic pillars. The diameter of each post, D_0, is 150µm spaced 225µm apart.

To measure velocity vector fields around the circular and superhydrophobic pillars in the microchannel, micro particle image velocimetry (PIV) system was utilized. The microchannel was placed to a Nikon inverted microscope (Nikon Eclipse TE 2000-U) with a 20× objective. Fluorescent particles with 1 µm diameter (FluoSpheres) were mixed with the distillated water and driven through the microchannel at a flow rate of Q=0.1ml/min. The particles absorb blue light from an illumination source (X-cite 120, EXFO) and emit green light. The emission from the tracer particles was collected by a high speed camera (Phantom V4.2) with 512 × 512 pixels resolution. The sample rate of the camera was 1000Hz, resulting in a time interval between successive images of Δt=1ms. A commercial PIV software (Davis 7.2 software, LaVision) was used to correlate the particle displacements and calculate velocity vector fields. To reduce noise, the velocity fields from 1000 individual cross-correlations were averaged to produce each vector field. The field of view for the PIV measurements is 559 × 559 µm so that a tight zoom could reveal the presence of slip along the air-water interface trapped within the apple-core-shaped superhydrophobic pillars. The minimum correlation window size used was 6 × 6 pixels with 25% overlap to maximize spatial resolution in search of slip. The resulting vector spacing was 4.4 µm. However, for the representational two-dimensional velocity vector fields and vorticity fields, a window size of 16 × 16 pixels was chosen to increase the vector length, while avoiding vector overlap. All the velocity measurements were performed in the middle of microchannel at a depth of 30µm.

4.3 Results and Discussion

Starting with a fresh microchannel, an air bubble was trapped within the side walls of the superhydrophobic apple-core-shaped pillars by a forced wetting process. In Figure 20a, the dry apple core-shaped superhydrophobic posts are shown in the microchannel. Water was driven with a syringe pump through the microchannel. As seen in Figure 20b, as the water advanced through the microchannel, the water was pinned and deflected at the front edges of each successive pillar. The water remained pinned until its contact angle with the pillars reached $\theta_A = 110^\circ$ locally. This can be seen in Figure 20b. Beyond this advancing contact angle, the air-water interface advanced along the surface of a single pillar. When the advancing water reached the upstream edge of the cut out in the apple-core-shaped pillar, the air-water interface continued to deform, but remained pinned. The combination of the high advancing contact angle and surface tension kept the water from wetting down into the cavity within the pillar wall. As a result, as the water progressed past each successive pillar, a small bubble of water was trapped within each apple-core-shaped pillar. The air bubbles were initially relatively small with flat or concave profile, however, as the pressure of the initial flow was removed, the air bubbles expanded beyond $D / D_0 > 1$ as seen in Figure 20c. This is because the pressure in the air phase remains set by the local pressure during the initiation of the microchannel in Figure 20b. As the flow is removed, the pressure in the water phase drops. The air will expand, until the internal pressure is balanced by the combination of water pressure and Laplace pressure produced by the curved air-water interface.

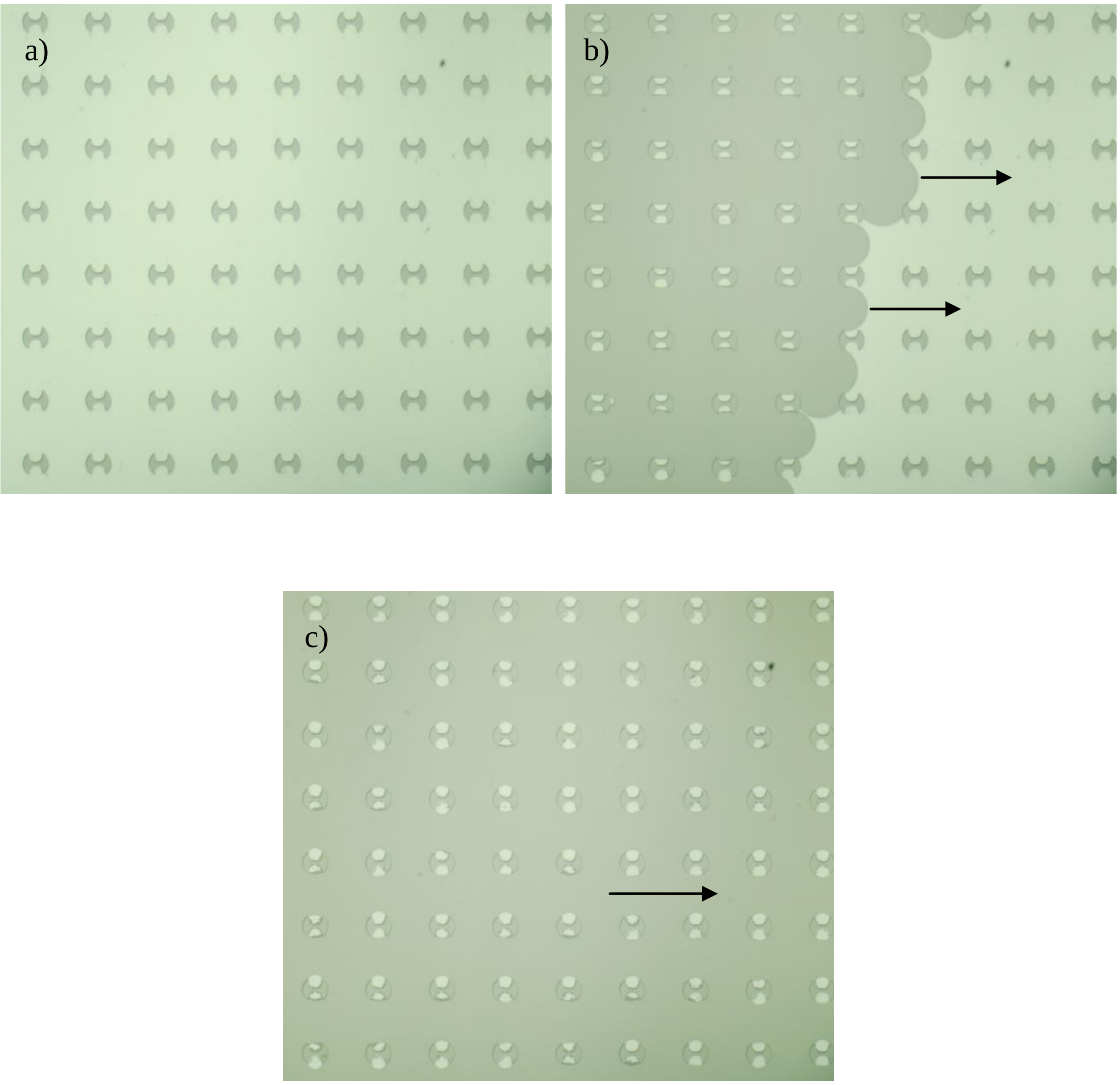

Figure 20: A series of microscope images showing the initialization of the microfluidic device and formation of the air-water interface in the superhydrophobic apple-core-shaped pillars at $Ca = 6.6\times10^{-5}$. Included are images of superhydrophobic pillars (a) dry prior to flow initialization, (b) during the wetting process, and (c) fully initialized. The flow direction is from left to right.

For comparison with the superhydrophobic pillar array, pressure drop measurements were first performed on an array of solid circular cross section pillars shown in Figure 19. At an average velocity of U=4.75mm/s and a capillary number of Ca= 6.6×10^{-5}, a pressure drop of ΔP=159.4 Pa was measured. Next, a series of pressure drop measurement were performed for the apple-core-shaped superhydrophobic pillar arrays to investigate the dependence of pressure drop on the shape of the trapped air-water interface. To facilitate these measurements, the pressure drop through the downstream tubing was systematically changed with a hose clamp in order to change the static pressure in the microfluidic device without affecting the flow rate. The changing static pressure modulated the curvature of the air-water interface through a range from D/D_0=0.8 to D/D_0=1.1. Multiple measurements with different interface curvature were made with a given microfluidic device, allowing interface shape and pressure drop to reach a stable equilibrium between each pressure drop measurement. The pressure drop reduction for superhydrophobic pillars and in some cases pressure drop enhancement was calculated by comparing its pressure drop to the pressure drop across the array of circular pillars at the same velocity and capillary number. The results are shown in Figure 21. The pressure drop reduction is defined as $PDR = (\Delta P_{circular} - \Delta P_{SHS}) / \Delta P_{circular}$. At D/D_0=1.0, where the protrusion of the air-water interface from within the apple-core-shaped pillar results in a cross-section shape that is identical to that of the circular pillar, a pressure drop reduction of PDR=2.5% was attained. Although data exactly at D/D_0=1.0 was not obtained, the pressure drop reduction at D/D_0=1.0 was interpolated from the data by fitting a second order polynomial to the measured pressure drop in Figure 21. This result shows the impact that the presence of the fluid slip that resulting reduction of shear stress at the air-water interface can have on the flow through a micro-pillar array. This pressure drop reduction may appear small when compared to flow across superhydrophobic surfaces with continuous slip interfaces (ridges, posts, etc) [18]. However, when compared against bubble matrices, which similarly pin the contact line and force the slip velocity to zero at upstream and downstream corners of the trapped air-water interface, this level of drag reduction is quite consistent [104, 105]. In addition, in our microfluidic device, the fluid experienced an additional large viscous drag from the presence of the top and bottom walls of the microchannel. The pressure drop from the viscous flow between two pillars, which is the drag reduced by the presence of the shear free air-water interface, is only one component of the total pressure drop. If one assumes a perfectly shear free pillar, a batch of the envelope calculation predicts a maximum of just over 13% drag reduction for this geometry.

As seen in Figure 21, the measured pressure drop reduction was found to be quite sensitive to changes in the shape of the air-water interface. By constricting the downstream tubing and raising the static pressure in the microchannel, the air-water interface trapped within the superhydrophobic pillars was compressed. At the highest pressures tested, the interface became flat and aligned parallel to the flow direction for D/D_0=0.8. As the air pocket was compressed, the effective flow cross-sectional area of the pillars became larger. As a result, the form drag related to the pillar size and shape as well as the drag resulting from shear stress associated with the flow between pillars was reduced. Thus, the pressure drop would have become smaller due to geometry changes even in the absence of the shear free air-water interface. A maximum pressure drop reduction of 18% was measured at D/D_0=0.8. By reducing the outlet constriction, the static pressure in the channel was reduced and the air pockets were allowed to grow beyond $D/D_0 > 1$. As seen in Figure 21, a sharp decrease in the pressure drop reduction was observed with increasing non-dimensional interface diameter. In fact, beyond $D/D_0 > 1.02$, a negative pressure drop reduction or in other words a pressure drop increase was observed. As the air-water interface protruded into the water phase, it becomes an additional obstacle to fluid flow by reducing the cross-sectional area between pillars. A 35% increase in the pressure drop was observed for the largest non-dimensional interface diameter tested, D/D_0=1.1. Similar measurements for bubble matrices with convex air-water interfaces have been reported in the post [104]. Here, we show for both convex and concave interface shapes that the drag through a microchannel array of superhydrophobic pillars can be very sensitively controlled by the air-water interface shape.

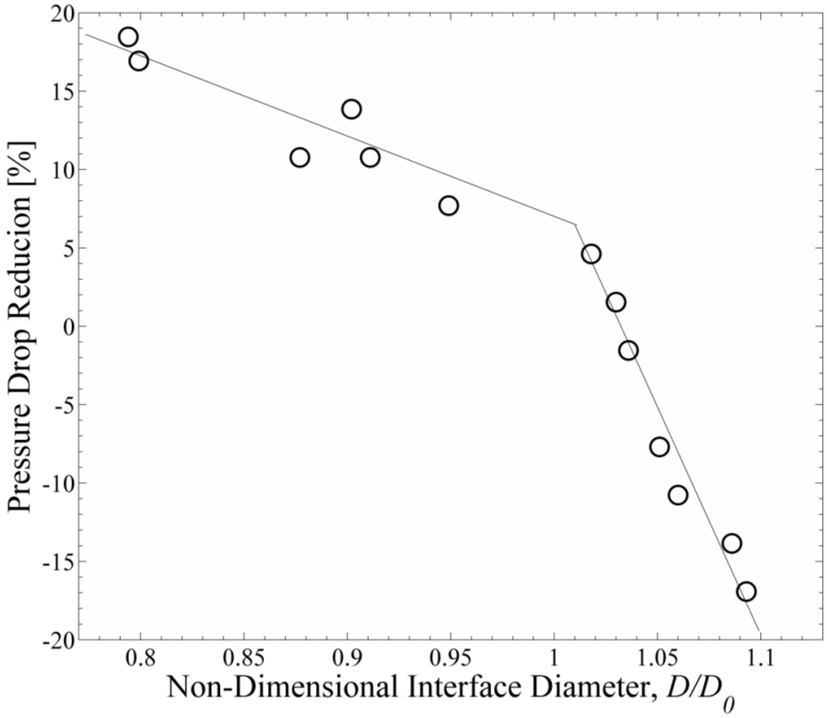

Figure 21: Pressure drop reduction as a function of non-dimensional interface diameter for flow through a microchannel containing a regular array of superhydrophobic apple-core-shaped pillars. The data is non-dimensionalized through comparison against an array of circular pillars with diameter D_0 and includes the experimental pressure drop (circles) and linear lines fitted to the data to guide the reader’s eye (solid line).

In order to better understand the observed pressure drop variation with changing the air-water interface shape, detailed velocity fields around two adjacent circular and superhydrophobic pillars were measured using micro particle image velocimetry (μPIV). These two-dimensional vector fields were then used to study in detail the presence and effect of slip along the air-water interface trapped with the superhydrophobic pillars. This was done by examining the evolution of the velocity profiles along three different slices parallel to the flow direction as well as one slice perpendicular to the flow cutting between the centers of two adjacent pillars.

The velocity vector fields and corresponding vorticity fields around the circular and superhydrophobic apple-core-shaped pillars are presented in Figure 22. The dimensionless interface diameter of the superhydrophobic pillars was D / D_0=0.88 and D / D_0=1.09, respectively. The spatial channel positions were non-dimensionalized by the diameter of the circular post, D_0=150μm. It should be noted that due to variations in the exact interface shape, cases of superhydrophobic pillars with asymmetric flow can be found throughout the microchannel. As seen in Figure 22, symmetric flow was observed on both the adjacent circular and superhydrophobic pillars. In both cases, stagnation points were observed at the leading edges and trailing of the pillars. The flow was then found to accelerate into the contraction between pillars before decelerating on its way out. This acceleration and deceleration of the flow allowed the resulting streamline curvature and shear results in high vorticity areas at the top and bottom of the pillars in the throat of the contraction.

From Figure 22, the first obvious difference between the circular and superhydrophobic pillars can be seen in the magnification of the vorticity. The maximum and extent of the vorticity for both cases of the superhydrophobic pillars were found to be smaller than those of the circular pillars. For $D/D_0 = 0.88$, the shape of the air-water interface was flat, which was parallel to the flow direction. The curvature effect from the geometry of the interface was reduced compared to the case of the circular pillar, resulting in the decrease in the magnitude of the vorticity. As the air-water interface was increased beyond $D/D_0 > 1$, the vorticity is expected to increase with the increased streamline curvature and velocity in the contraction. In fact, the presence of the slip at the air-water interface was found to reduce the magnitude of the vorticity at $D/D_0 = 1.09$.

To quantify magnitude of the vorticity attenuation at $D/D_0 = 1.09$, the maximum values of vorticity around six different sets of pillars was measured and averaged. The absolute maximum of the vorticity for the superhydrophobic case was measured to be ω=155 s^{-1} . Thus, the presence of the air-water interface resulted in a 12% decrease in the vorticity compared to the flow past a solid circular pillar. Reduction of vorticity has been observed previously for flow past a micro-scale circular cylinder with a superhydrophobic coating [87]. In those experiments, which were performed at large Reynolds number, the reduction in vorticity was found to delay flow separation and vortex shedding and reduce the magnitude of the time periodic lift force [109].

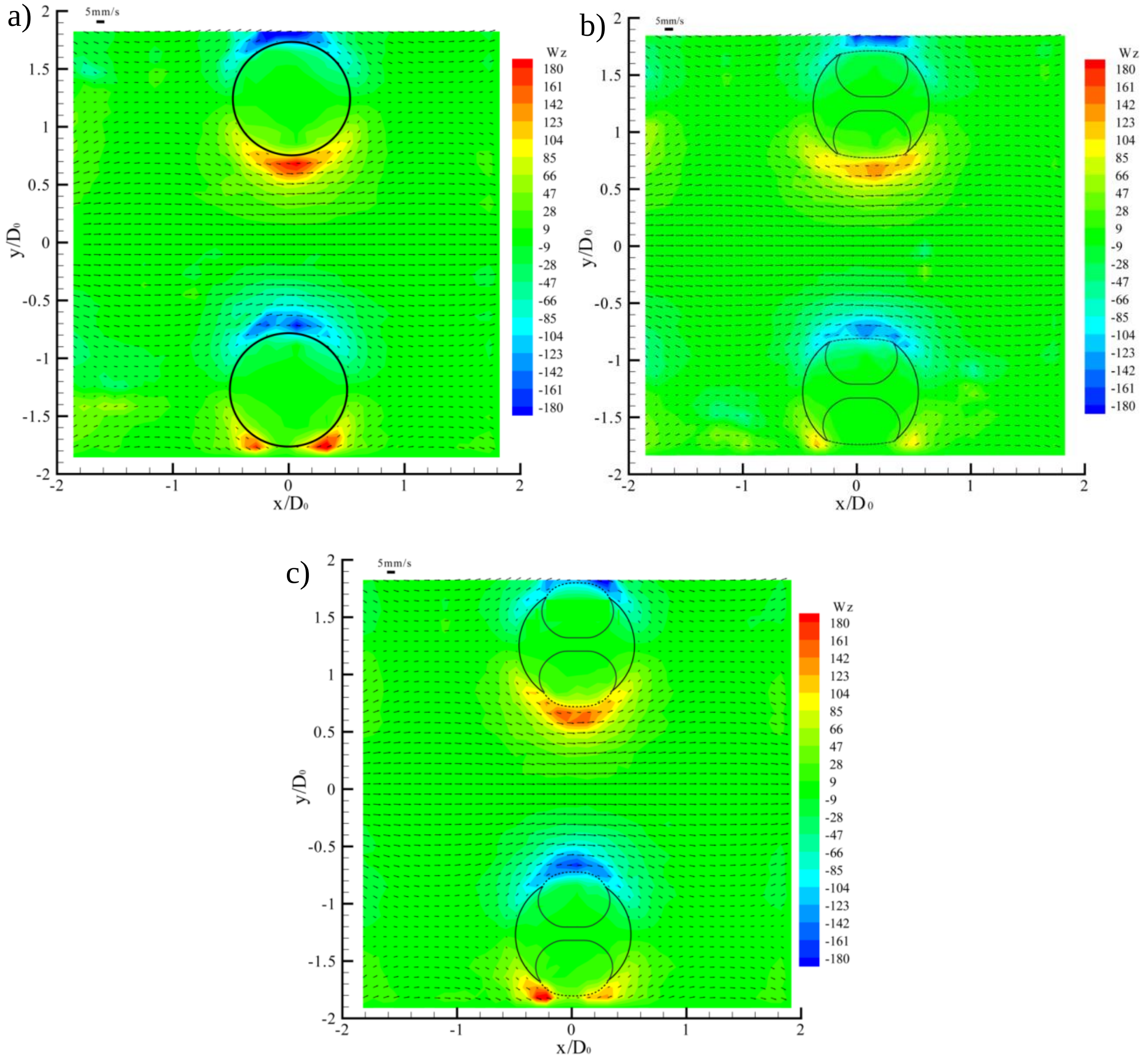

Figure 22: Particle image velocimetry (PIV) vector fields of flow through a regular array of (a) circular and (b) and (c) superhydrophobic apple-core-shaped pillars at *Ca*= 6.6×10^{-5} with vorticity overlaid as a contour map. Solid lines are overlaid on the data to indicate the position of pillars while dashed lines are used to represent the position of the air-water interface formed by the air bubble trapped against the superhydrophobic pillar. For the superhydrophobic pillar, the non-dimensional diameter was measured to be (b) D/D_0=0.88 and (c) D/D_0=1.09 from bright-field image.

In Figure 23, streamwise velocity measurements are presented for both the circular pillars and the apple-core-shaped superhydrophobic pillars along the three different slices between the two pillars parallel to the flow direction. In all the cases, the streamwise velocities were non-dimensionalized by the average streamwise velocity, $U_{avg} = 4.75$ mm/s. A schematic diagram is inserted into Figure 23 to show the locations of the horizontal measurement slices: which were located specifically at the bottom edge of the circular pillar or, for the case of two superhydrophobic pillars, at the edge of the air-water interface of the upper pillar, along a horizontal slice 4.4μm below the first slice off closer to the centerline, and along the centerline between the two adjacent pillars.

As shown in Figure 23a, along the centerline between the two pillars, the streamwise velocity was found to accelerate from $U/U_{avg} = 0.95$ to $U/U_{avg} = 1.27$ by 33% for the circular pillars. A similar amount of the increase in the acceleration of the flow was observed at $D/D_0 < 1.0$ for the superhydrophobic pillars. However, as the air-water interface was increased and reached up to $D/D_0 = 1.09$, the streamwise velocity was found to accelerate from $U/U_{avg} = 0.92$ to $U/U_{avg} = 1.30$ by 41%. The increase in the maximum velocities of the flow between the superhydrophobic pillars was slightly larger than that of the circular posts for two reasons. One, there is slightly larger confinement effects as $D/D_0 > 1.0$ and two, as we will see, there is slip along the air-water interface trapped against the apple-core-shaped superhydrophobic pillar. Note that because of the relative proximity of the upstream and downstream pillars, the velocities in the microchannel are not consistent. Integrating the velocity profile along any vertical slice confirms conservation of mass for both pillars within a couple of percent. Additionally, the influence of the upstream and downstream pillars can be observed in the upstream in the velocity data at x/D_0=1.3 which is the midpoint between pillars. The data for all velocity profiles was found to be symmetric around this point as expected.

Even more significant variations in the streamwise velocities can be observed slices taken very near the solid and superhydrophobic pillars. The streamwise velocity profile past both the circular and superhydrophobic pillars decreased from nearly U/U_{avg} = 0.7 for upstream of the pillars to a minimum at the narrowest point in the centerline and increased downstream of the pillars back to U/U_{avg} = 0.7. For the slice that passes through the edge of the circular pillar, the streamwise velocity was found to go to zero, thus confirming the no-slip condition at the solid surface.

The evolution of the velocity profiles obtained for the superhydrophobic pillars was quite different in two important ways. First, as the non-dimensional interface diameter was increased and reached $D/D_0 = 1.09$, the streamwise velocity was found to increase slightly from U/U_{avg} = 0.69 to U/U_{avg} = 0.73 just upstream and downstream of the pillars at $D/D_0 = \pm 0.7$. This could be due to the slight differences in the pillar cross sectional geometry as the air bubble attached to the superhydrophobic pillar in this case protruded out beyond extent of the circular pillar to a width of D/D_0=1.09 and resulting in a slightly non-circular shape which could modify the local velocity profile. This flow phenomenon is more prevalent for the data in the slice taken 4.4μm away from the air-water interface as shown in Figure 23c. Note that when the non-dimensional interface diameter was smaller than one, $D/D_0 < 1$, the increase in the streamwise velocity was not observed near the edge of the air-water interface.

Second, at the neck, streamwise velocity past the superhydrophobic pillars does not go to zero, but instead shows a pronounced slip velocity of approximately 20% and 30% the average velocity in the channel for $D/D_0 = 0.88$ and $D/D_0 = 1.09$, respectively. The micro PIV measurements past superhydrophobic surfaces in the past have shown similar magnitude slip velocities [19]. These results indicate that the air bubbles trapped within the superhydrophobic pillars could act as obstacles to the flow when its size increase beyond $D/D_0 > 1$ even as a large slip velocity is observed along the trapped air-water interface.

For the PIV measurements presented in Figure 23, the final computation window size was 6 × 6 pixels, resulting in a vector spacing of 4.4 µm. In order to accurately report a slip velocity and slip length, the position of the solid-water interface of the circular pillars and the air-water interface of the superhydrophobic pillars must be very accurately known. To find their location, bright-field images were used to accurately determine the position of the solid-water and air-water interfaces within a single pixel (or 1µm) using ImageJ. Once the location of the interface was attained, the slip velocity at the interface was determined by fitting the six velocity data points closest to the interface with a second order polynomial and extrapolating the fit to the interface. In Figure 24, the streamwise velocity profile measured along a vertical/ cross flow slice connecting the centers of the two pillars is shown. The solid vertical lines at $y/D_0 = \pm 0.75$ indicate the edge of the circular pillar while the vertical dashed lines at $y/D_0 = \pm 0.7$ indicate the position of air-water interface trapped within the superhydrophobic pillar. The slip velocity data extrapolated from the second order fits are superimposed on the interface lines.

For both the circular and superhydrophobic pillars, the streamwise velocities were found to remain nearly constant between the two adjacent pillars. This is consistent with flow through rectangular channels where the height is significantly smaller than the width. The velocity decreases sharply with a large velocity gradient near the pillars. The velocity at the solid circular pillar was found to be zero within the uncertainty of the velocity and wall position, confirming the no-slip boundary condition. However, the velocity at the air-water interface of the superhydrophobic pillars was measured to be non-zero with an average value of $U_{slip} = 1.7 \pm 0.2$ mm/s at $D/D_0 = 1.09$, as shown in Figure 24. This slip velocity corresponds to 36% of the average streamwise velocity in the microchannel. When the non-dimensional interface diameter was larger than one, $D/D_0 > 1$, similar amount of slip velocity was observed and its average value was measured to be $U_{slip} = 1.3$ mm/s. Given the spatial uncertainty of the interface location and the error of the velocity measurements, the data is known with an uncertainty of ± 0.3 mm/s. Additionally, this slip velocity can be reanalyzed in terms of Navier's slip length, *b* [15]. The slip length is the hypothetic distance to be extended to achieve the same pressure drop. In this case, $b \simeq 6.7 \pm 0.8 \mu m$, which is similar to the measurement in the literature for bubble matrices [45]. Note that, as the non-dimensional interface diameter was smaller than one, $D/D_0 < 1$, the slip velocity was found to decrease. It was measured to be $u_{slip} = 0.3 \pm 0.2$ mm/s at $D/D_0 = 0.88$.

As seen in Figure 24, this large slip velocity was present even if the air bubble was protruded toward the water phase and the non-dimensional interface diameter became D/D_0=1.09. Based on the result that the pressure drop was increased by 17% at D/D_0=1.09, the geometry effect of the air-water interface was found to dominate the flow changes in this case over the slippage effect at the air-water interface. This is especially important as the non-dimensional interface diameter is increased.

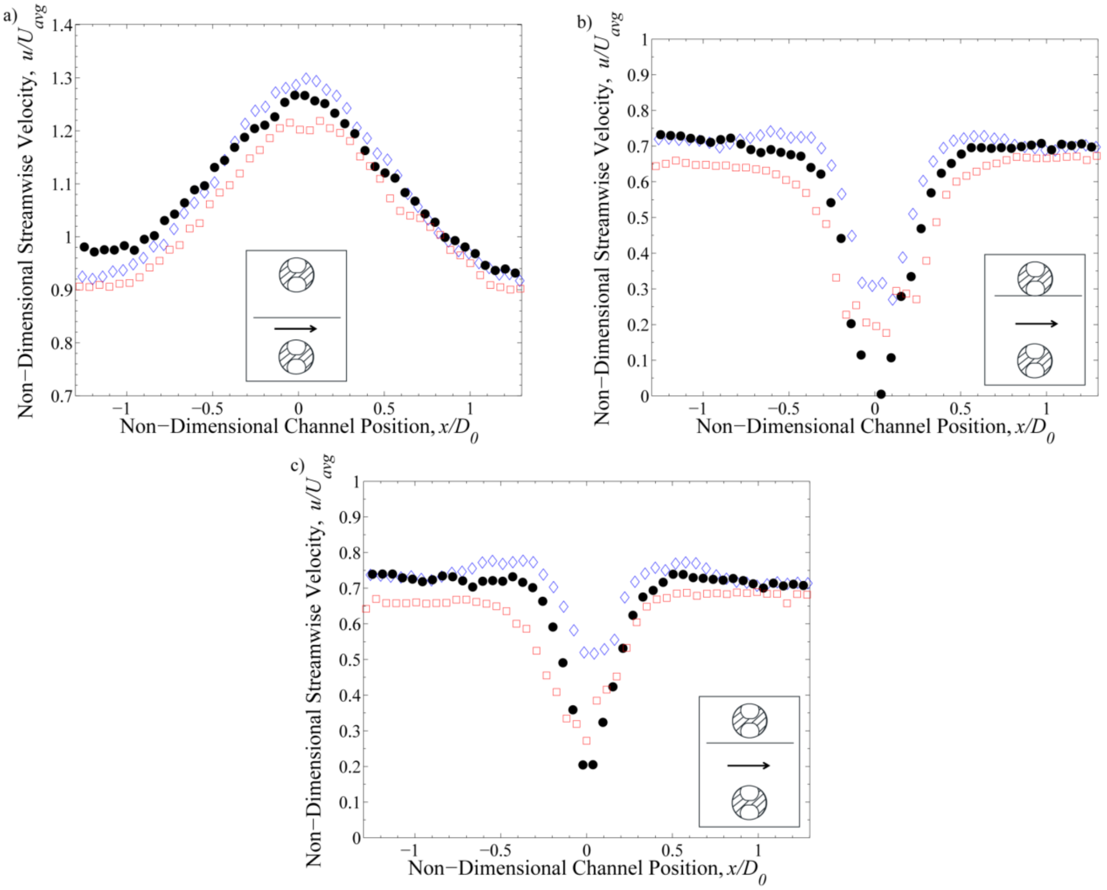

Figure 23: Non-dimensional streamwise velocity as a function of non-dimensional channel position, x/D_0. The streamwise velocities were measured along (a) the centerline between two posts, (b) at the edge of the solid surface or air-water interface of the upper pillar, and (c) at a position 4.4µm below the edge of the upper pillar. The velocity was non-dimensionalized by the average streamwise velocity, u/U_{avg}. Inset shows the locations of the measurement slices in relation to the two pillars. The experimental data include the velocity measured in the microchannel with the circular pillars (filled circle) and the superhydrophobic apple-core-shaped pillars (square for D/D_0=0.88 and diamond for D/D_0=1.09).

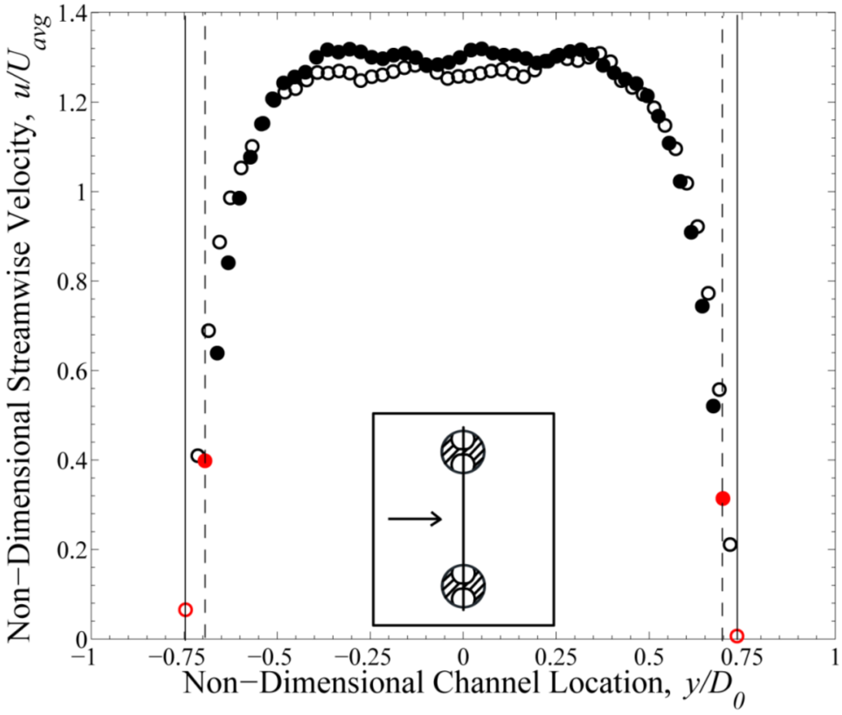

Figure 24: Non-dimensional streamwise velocity u/U_{avg} as a function of non-dimensional channel location for velocities evaluated along x/D_0 =0. The experimental data include velocity profiles for circular pillars (○) and superhydrophobic pillars (●). The slip velocity data are superimposed on the interface lines with red symbols. The vertical solid lines at $y/D_0 = \pm 0.75$ represent the edge of the circular pillar while the dashed lines at $y/D_0 = \pm 0.7$ represent the location of the air-water interface formed around the superhydrophobic pillar.

4.4 Conclusions

The measurements of the pressure drop and velocity vector fields through a regular array of superhydrophobic pillars were performed to investigate the role of the air-water interface shape on drag reduction. The PDMS microfluidic channel was created with a regular array of apple-core-shaped superhydrophobic and circular pillars. The air was trapped on the side of each superhydrophobic pillar because of the shape and hydrophobicity of the pillar. The air-water interface was changed from concave to convex shape by changing the static pressure in the microchannel. All the measurements were performed in capillary number of $Ca = 6.6\times10^{-5}$. The pressure drop through the microchannel containing the superhydrophobic pillars was found to be sensitive to the air-water interface shape. For static pressure which resulted in the apple-core-shaped superhydrophobic pillars having a circular cross section, $D/D_0 = 1$, the drag reduction of 7% was measured as a result of slip along the air-water interface. At large static pressures, the interface was driven into the apple-core-shaped pillars. It results in decrease in the effective size of the pillars and an increase in the effective spacing between pillars. The maximum pressure drop reduction of 18% was measured at the non-dimensional interface diameter of D/D_0=0.8. At small static pressures, on the contrary, the pressure drop was increased by 17% at D/D_0=1.1 as the expanding air-water interface constricted flow through the array of pillars even if the large slip velocity was maintained. To better understand the significant change in the pressure drop, the velocity vector fields around the circular and superhydrophobic pillars were measured by a micro particle image velocimetry (µPIV). The symmetric flow was observed for both the circular and superhydrophobic pillars. Along the centerline between the pillars, the streamwise velocity was found to accelerate at the contraction of the circular and superhydrophobic pillars. As the air-water interface of the superhydrophobic pillars was expanded and reached up to $D/D_0 = 1.09$, the streamwise velocity was increased by 41% which was larger than the case of the circular pillar, 33%. Even more obvious changes in the flow around the circular and superhydrophobic pillars were observed in the velocity profiles taken very near the pillars. The streamwise velocity was decreased from $U/U_{avg} = 0.7$ for upstream of the pillars to a minimum at the narrowest point in the centerline and increased downstream of the pillars back to $U/U_{avg} = 0.7$. In particular, the streamwise velocity was found to increase by 5% just upstream and downstream of the superhydrophobic pillars at $D/D_0 = 1.09$ since the air bubble trapped in the superhydrophobic pillar protruded out beyond extent of the circular pillar.

The slip velocity at the air-water interface was found to exist in all the non-dimensional interface diameters tested. The average slip velocity was measured to be $u_{slip} = 1.3$ mm/s, which corresponded to 27% average streamwise velocity in the microchannel. The corresponding slip length was measured to be $b = 6.7\mu m$. Interestingly, the slip velocity was still valid at D/D_0=1.09 where the pressure drop was increased by up to 17%. These results explain that the geometry effect of the air-water interface became dominant when the interface diameter of the superhydrophobic posts became larger than that of the circular posts. Throughout a series of measurements of pressure drop and velocity vector fields, both the geometry and slippage effects on the air-water interface was found to affect laminar drag reduction.

CHAPTER 5

DRAG REDUCTION ON LIQUID-INFUSED SUPERHYDROPHOBIC SURFACES

5.1 Introduction

Superhydrophobic surfaces are rough hydrophobic surfaces containing micron and/or nanometer-sized surface structures. The combination of the chemical hydrophobicity and the small scale surface roughness can result in the entrapment of air within the surfaces topography. The presence of this air-water interface has been shown to mobilize liquid droplets on these superhydrophobic surfaces, allowing droplets to slide off easily. This observation is a direct result of the high advancing contact angle, $\theta_A > 150^\circ$, and the low contact angle hysteresis, $\theta_H = \theta_A - \theta_R \approx 5^\circ$ that can be achieved with the right surface design. The presence of the air-water interface trapped along a superhydrophobic surface can be utilized for laminar or turbulent drag reduction [15, 18-21, 23, 25, 110], and to make a surface self-cleaning [8, 17], anti-fouling [26, 27], or anti-icing [28, 29]. Due to the incredible potential of superhydrophobic surfaces over a broad range of applications and industries, the development of superhydrophobic surfaces has drawn a lot of attention among researchers in the past two decades [30, 34].

Unfortunately, there are a number of inherent issues with application of superhydrophobic surfaces that could hinder their wide-spread adaptation in areas such as drag reduction. The air that is trapped within the structures of the superhydrophobic surfaces can collapse under high static or dynamic pressure [15, 50]. Loss of the trapped air can also occur when the superhydrophobic surface is brought in contact with organic liquids or complex mixtures with low surface tension. Additionally, defects introduced during the manufacturing process or mechanical damage incurred during experimentation can also cause a loss of the air-water interface [3, 50]. Without the air-water interface, the attractive benefits of the superhydrophobic surfaces for drag reduction, droplet mobilization or anti-icing cannot be realized.

Liquid-infused surfaces (LIS) have recently been developed and shown great promise to overcome many of the inherent limitations of conventional air-infused superhydrophobic surfaces. Wong et al., [49] whose work was inspired by the Nepenthes pitcher plant, utilized the small scale structures of superhydrophobic surfaces as a space to lock in an incompressible and immiscible lubricant. They demonstrated that the liquid-infused surfaces had a number of interesting properties including: liquid repellency of various simple and complex liquids with low surface tension, robustness under high pressure, and restoration of liquid repellency after physical damage. Several research groups have investigated further potential benefits of liquid-infused surfaces [51-56]. Here we will focus on the application of liquid-infused surfaces to drag reduction.

Using a cone and plate rheometer, Solomon et al. [55] measured the drag forces on liquid-infused surfaces. Their surfaces were fabricated from a silicon wafer using a laser ablation process that resulted in a surface with 50µm tall posts spaced roughly 50µm apart with nanometer scale roughness decorating the sides and tops of the posts. A series of different viscosity oils were used to coat the rough silicon surface while the working fluid was a water-glycerin mixture. The viscosity ratio, μ_w / μ_o, between the working fluid and the lubricating oil was varied from approximately $\mu_w / \mu_o = 0.03$ to 260. Here, μ_w is the viscosity of the bulk aqueous phase and μ_o is the viscosity of the oil phase infused into the surface. Solomon et al. [55] demonstrated that an increase in drag reduction could be achieved with increasing viscosity ratio resulting in a maximum drag reduction of 16% and an equivalent slip length of 18μm for the case with the largest viscosity ratio tested, $\mu_w / \mu_o = 260$. One advantage to using a cone-and-plate rheometer to measure drag reduction of liquid-infused surfaces is that the imposed flow has closed streamlines. As a result, depletion of oil from lubricating layer with time in the flow direction is negligible and does not affect the measured drag reduction. Jacobi et al. [111, 112] showed that fluid-fluid interface can be rearranged by the centripetal pressure gradient, however, they showed that the presence of microstructure and the concentric pinning lines that Solomon et al. [55] etched onto the surface would mitigate radial oil depletion as well. However, for flows without closed streamlines, like the flow through a microchannel studied here, loss of oil from the lubricating layer can be a serious problem [111-114]. This is because to obtain drag reduction, a non-zero slip velocity is produced at the interface between the bulk fluid and the lubricating fluid, whether air or oil [19]. This slip velocity can be 50% or more of the average bulk free-stream velocity. As a result, the flow of the bulk fluid imparts a non-zero velocity to the lubricating fluid trapped within the rough surface. For flow within a microchannel, therefore, oil is driven along the liquid-infused surfaces from the inlet to the outlet where it is either swept away or forced to recirculate within the lubricating layer thereby reducing its effectiveness for drag reduction. As a result, in some cases, continuous injection of the lubricant from a reservoir is necessary for prolonged operation of liquid-infused surfaces [49, 55].

In this study, systematic measurements of the pressure drop for the flow past a series of liquid-infused surfaces in a microchannel will be presented. To test the impact of surface design on drag reduction, the lubricating oil was infused into a series of superhydrophobic surfaces containing both precisely engineered patterns of micro-posts and micro-ridges as well as randomly rough superhydrophobic surfaces fabricated by sanding PTFE with various sandpaper grits. The longevity of the lubricant layer on each surface was studied both with microscopy and time-resolved pressure drop measurements. The experimental results demonstrate that, for the surfaces studied here, the randomly rough liquid-infused surfaces were more effective at maintaining the lubricating oil layer. However, it should be noted that, even for the most effective surfaces tested, a loss in performance was observed with time. These measurements presented here will provide potential applicability and limitations of liquid-infused surfaces to microfluidic devices and large scale drag reduction applications such as turbulent drag reduction in pipelines and along ship hulls.

5.2 Experimental Setup

The initial experiments In the experiments presented here, the drag reduction of flow past liquid-infused surfaces was measured using a microchannel geometry. A schematic diagram of the microfluidic flow cell used to make pressure drop measurements is shown in Figure 25. The microfluidic device consists of three parts: a rectangular microchannel, testing surfaces, and two clamps used to seal the microchannel.

The microchannel was fabricated from Polydimethylsiloxane (PDMS) (Sylgard 184, Dow Corning) using a standard soft lithography method. An inlet and an outlet for the flow of working fluids were introduced at the ends of the microchannel and spaced 60mm apart. In addition, two pressure ports were created in the microchannel 45mm apart to measure the pressure drops across the liquid-infused surfaces. The microchannel was attached to an acrylic cover slip to increase its rigidity and distribute the clamping force uniformly across the device. Due to the low modulus (~1.8 MPa) of the PDMS, the microchannel was deformed slightly when it was sealed resulting in an actual microchannel depth measured to be 150μm through microscopy and fits to the pressure drop measurements from flow past smooth PTFE surfaces. Note that the effect of the side walls of the microchannel are negligible in our experimental set up due to its high aspect ratio (23:1) [24]. As a result, for the purposes of theoretical pressure drop calculations, the channel can be assumed to be equivalent to two infinite parallel plates without introducing significant error.

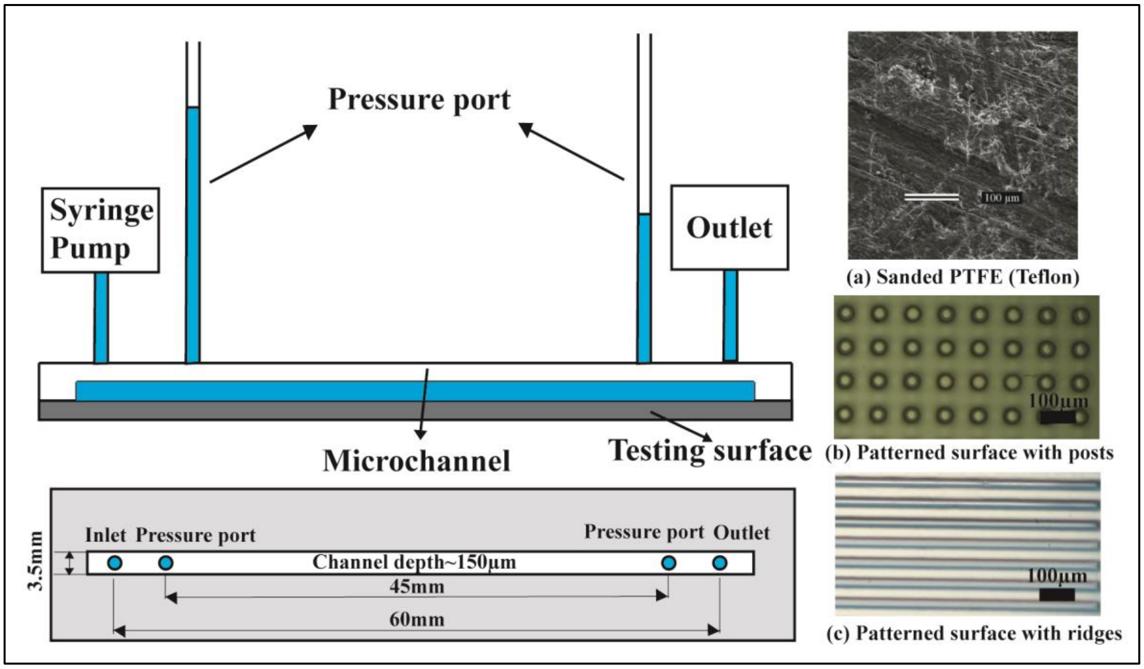
Pressure port
Syringe Pump
Outlet
Microchannel
Testing surface
Inlet
Pressure port
Pressure port
Outlet
3.5mm
Channel depth~150µm
45mm
60mm
100 µm
(a) Sanded PTFE (Teflon)
100µm
(b) Patterned surface with posts
100µm
(c) Patterned surface with ridges

Figure 25: Schematic diagram of the experimental set up used for pressure drop measurements. Also included are (a) a scanning electron microscopy image of a PTFE surface sanded with 240-grit sandpaper (RMS roughness of 13.7µm) and optical microscope images of (b) a PDMS surface consisting of 50µm posts spaced 50µm apart, and (c) a PDMS surface containing 30µm ridges spaced 30µm apart.

In order to create a series of randomly rough superhydrophobic surfaces to test as liquid-infused surfaces, smooth polytetrafluoroethylene (PTFE) surfaces (McMaster-Carr) were sanded by several grits of sandpapers (McMaster-Carr) to impart small scale surface features [24, 33]. A scanning electron microscopy (SEM) image of the resulting PTFE surfaces is shown in Figure 25a. This technique for fabricating superhydrophobic surfaces was initially developed by Nilsson et al. [33]. They demonstrated that superhydrophobic surfaces with very large advancing contact angles, $\theta_A \approx 150^\circ$, and extremely low contact angle hysteresis, $\theta_H \approx 5^\circ$, could be generated using a 240-grit sandpaper. In addition, they demonstrated that the advancing contact angle and the contact angle hysteresis could be controlled by selection of sandpapers and the surface roughness that it imparts onto the PTFE. To produce the sanded PTFE surfaces, a smooth PTFE surface was first glued to the microscope glass with epoxy to keep the surface flat and smooth. The surface was then sanded by hand with a sanding motion biased in the flow direction using sandpaper grits of 180, 240, and 320 [24]. The resulting RMS surface roughness was measured to be 15.4μm, 13.7 μm, and 10.9 μm for 180-, 240- and 320-grits of sandpaper based on the literature [33]. To maximize consistency between surfaces, the sanding was performed for the same amount of time and applied pressure for each surface. However, given the variation resulting from the fabrication process, it was important to perform experiments using a number of different sanded PTFE surfaces. For each experimental data point presented here, at a minimum, three surfaces were fabricated and tested independently so that experimental uncertainty could be assessed [24]. Following the sanding of the surfaces, a residue of PTFE particles remained and was removed from the surface by first blowing them off with compressed air and then performing a final rinse with distillated water. The surfaces were then allowed to air dry before being coated with the lubricating fluid.

The precisely patterned superhydrophobic surfaces were fabricated in PDMS using standard soft lithography methods [18, 40]. The masks used for the fabrication of master wafers were printed on a high-resolution transparency with a resolution of 20,000 dpi, thus allowing for features as small as 10µm. The pattern was transferred from the mask to the wafer using mask aligner and a photoresist (SU-8) resulting in a surface topography that was a negative of the desired superhydrophobic surface. For these experiments, the patterns consisted of circular micro-posts and micro-ridges with a diameter/width 50µm and 30µm, respectively, as seen in Figure 25b and 25c. The spacing between the micro-ridges was varied from 30µm to 60µm while the features were all 25µm tall. To create the superhydrophobic surface, polydimethylsiloxane (PDMS) (Sylgard 184, Dow Corning) was cast onto the silicon master and cured overnight at $60^{\circ}\mathrm{C}$. After gently peeling the PDMS from the silicon master it was ready to be coated with the lubricating oil.

In order to produce drag reduction, the lubricant fluid within the liquid-infused surfaces must not be miscible with the working fluids [49, 55]. A number of different oils were tested before selecting silicone oil. Silicone oil was chosen because it was found to fully wet the surface features of both the PDMS and PTFE in the presence of both air and the working fluid. Furthermore, it was crucial to select a lubricant with low viscosity so that the ratio of the viscosity of the working fluid, μ_w, and the viscosity of the lubricating oil, μ_o, could be as large as possible, $\mu_w / \mu_o \gg 1$. To accomplish this, silicone oil with a viscosity of $\mu_o = 5\text{cP}$ was chosen. In order to create a uniform coating on the superhydrophobic surfaces, the surface was tilted to 75°. A constant volume of 9µl of silicone oil was then placed at the top of the surface and allowed to wick into the features on the surface under the combined action of surface tension and gravity. Excess oil was allowed to drain from the bottom of the surface and any large drops were gently scraped away using a flexible doctoring blade. Note that increasing the volume of oil introduced onto the superhydrophobic surface did not have any effect on drag measurements, however, using less than 9µl of oil resulted in a surface that was not fully infused with oil and larger initial pressure drop measurements.

For the working fluid, a series of glycerin and water solutions of different compositions were created. They varied in viscosity from that of pure water with the viscosity of μ_w = 1cP to the glycerin and water solutions which had viscosities of μ_w = 26cP and 46cP. Given the viscosity of the silicone oil, viscosity ratios of μ_w / μ_o = 0.2, 5.2, and 9.2 were achieved. Once the microchannel and the testing surface with a lubricant layer were carefully aligned and sealed [24], a syringe pump (KD Scientific Model 100) was used to pump the working fluid through the microfluidic device at a constant flow rate. The flow rate was systematically varied to probe the effect of flow velocity on drag reduction for each of the surfaces and viscosity ratios tested. However, so that the experiments at different viscosity ratios could be compared to each other, a set of experiments were all performed at a constant in capillary number of $Ca = \mu_w U / \gamma = 0.001$. The capillary number compares the relative importance of viscous to interfacial stresses in a flow. Here U is the average velocity in the microchannel and $\gamma = 29\text{mN/m}$ is the interfacial tension between the aqueous working fluid and the lubricating oil [115].

5.3 Results and Discussion

The initial experiments were performed using the precisely patterned PDMS superhydrophobic surfaces. To ensure the quality of the superhydrophobic surface, measurements of drag reduction with the surface in the Cassie-Baxter state, with air trapped between the features of the superhydrophobic surface, were performed and compared to previous measurement in the literature. Measurements of the pressure drop reduction and slip length for the air-infused superhydrophobic surfaces containing 30μm wide micro-ridges spaced 30μm apart were measured to be 40% and 20μm respectively, compared to the measurements for the smooth PDMS surface. These measurements are in agreement with our previously published results for this superhydrophobic surface [18]. The air was then displaced by coating the superhydrophobic micro-ridge surface with silicone oil as described in the previous section to test the effectiveness of liquid-infused surfaces for drag reduction. The expectation was that for a large viscosity ratio between the aqueous phase and the oil approaching the viscosity ratio between water and air, $\mu_{water} / \mu_{air} = 55$, that similar values of drag reduction would be achieved. Unfortunately, no pressure drop reduction was observed for flow past the liquid-infused surfaces containing 30μm ridges even at the largest viscosity ratio tested, $\mu_w / \mu_o = 9.2$, when compared to the result of the smooth PDMS surface. To test the effect of flow rate, the flow rate was varied between $0.01\text{ml/min} < Q < 1\text{ml/min}$ which is equivalent to an average velocity within the microchannel of $0.3\text{mm/s} < U < 31.7\text{mm/s}$ and equivalently a capillary number between $0.0005 < Ca < 0.05$. No pressure drop reduction was observed in any of the cases for the precisely patterned liquid-infused surfaces tested. Similar observations were made for liquid-infused surfaces with 30μm wide micro-ridges spaced 60μm wide and 50μm micro-posts spaced 50μm apart.

To understand this null result, the lubricant layers of patterned surfaces were observed optically before and after the pressure drop measurements using an inverted microscope (Nikon TE2000) with a 10x objective. The microscope images are shown in Figure 26. The images in Figure 26a clearly demonstrate that, before the flow is initiated, the silicone oil, which is dyed in Figure 26a to appear dark, fully wicks into grooves between the micro-ridges on the PDMS surface creating a uniform lubricating layer. After a flow rate of U=0.4 mm/s with a viscosity ratio between the working fluid and lubricating layer of $\mu_w / \mu_o = 9.2$ was imposed across the liquid-infused surfaces, the image in Figure 26b clearly shows that the oil within the liquid-infused surface was partially swept away by the flow, driven downstream and removed through the outlet of the microchannel. During the experiment, the working fluid penetrated into and recirculated within the grooves between the micro-ridges, displacing the lubricant and leaving behind grooves that at steady state were only partially filled by lubricant. In some cases, the lubricant that was left behind in the PDMS grooves was observed to contain small droplets of the working fluid. As the flow rate decreases, the rate of depletion of the lubricant layer was slowed. In all cases tested, however, the oil interface was stripped well before the pressure drop measurements reached equilibrium, making it impossible to observe the transient effects on this case. Similar depletion of the lubricant layer was also observed in the case of PDMS liquid-infused surfaces patterned with 50μm wide micro-posts.

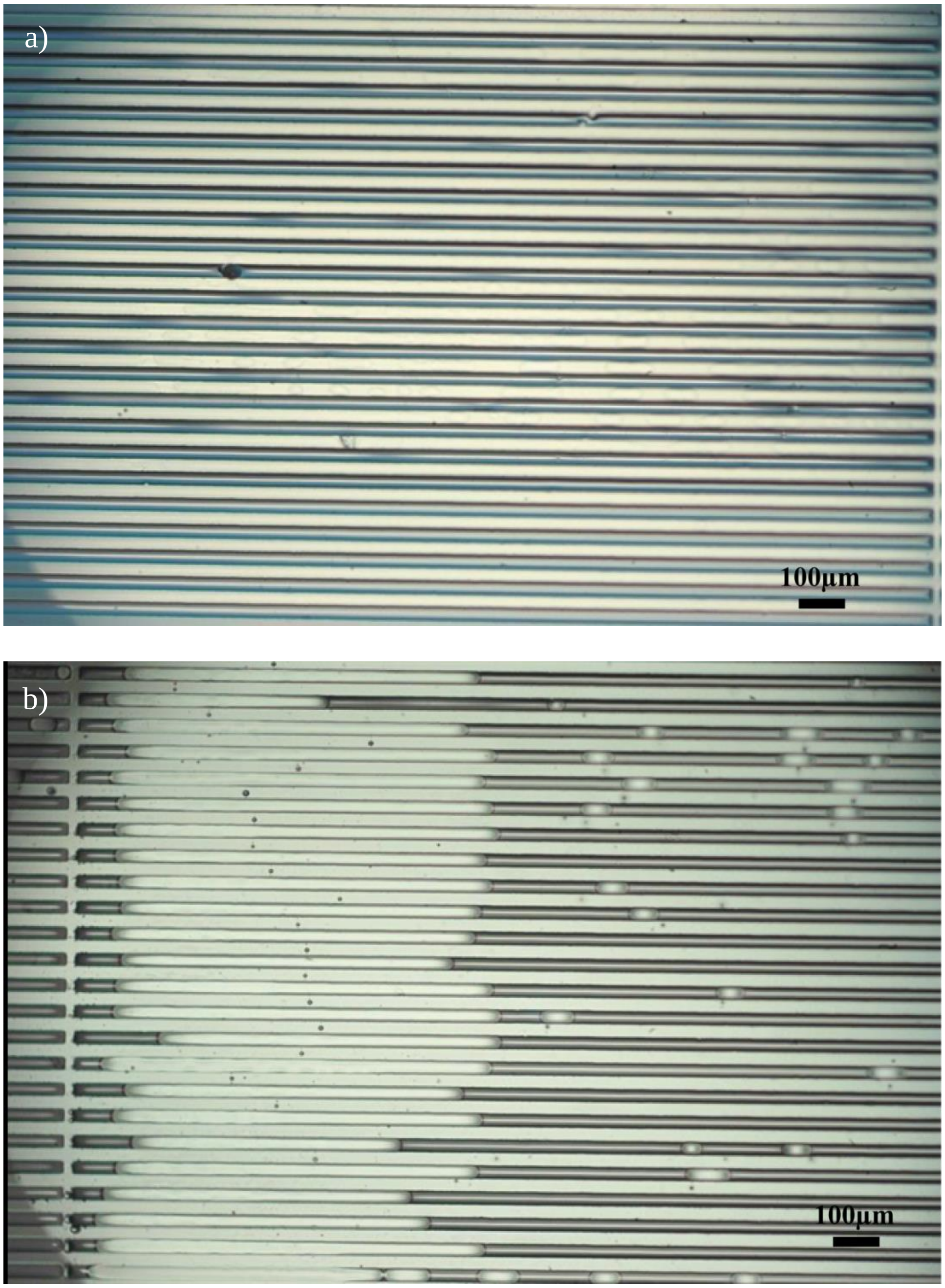

Figure 26: Microscope images of a superhydrophobic surface patterned with 30µm spacing micro-ridges (a) before flow showing all the channels between the micro-ridges fully filled with lubricating oil and (b) after a flow of *U*=0.4mm/s was applied for *t*=120 min showing oil partially stripped from between the micro-ridges.

A number of additional modifications were made to attempt to stabilize the lubricating oil layer. Silicone oil was initially used, however, with long exposure it was found to cause the patterns on the PDMS surface to swell perhaps facilitating the loss of oil from the liquid-infused surfaces or perhaps causing an increase in the drag masking the expected pressure drop reduction. As an alternative, Miglyol oil, which is commonly used in cosmetics, was chosen as the lubricant fluid. Miglyol oil is known not to swell PDMS and also can be purchased with a low viscosity, 10cP, and low interfacial tension with pure water, 20mN/m. On both PDMS superhydrophobic surfaces, however, the depletion of the lubricant layer occurred again even in after lowest capillary number tested, $Ca = 0.0005$.

This failure to maintain fully wicked lubricant layer on patterned liquid-infused surfaces was also observed by Wexler et al. [113, 114]. They used a transparent microfluidic flow cell with a surface patterned with 9µm wide grooves spaced 9µm apart and observed the depletion of silicone oil from the grooves over time. The shear stress from the external flow of water was found to induce a recirculation within the lubricant layer trapped within the micron-sized grooves. The net result was a fast depletion of the lubricant from the downstream end of the surface grooves. At long times, Wexler et al. [113, 114] showed that a finite length of the lubricant layer remained within the grooves near the outlet port of the microfluidic device. The final wetted length of the grooves was found to depend on interfacial properties of the fluids and the aspect ratio of the patterned surface features. More importantly, the supplements they provide clearly show that micro-posts of the same height randomly placed on the surface delayed the depletion of the oil from the lubricating layer. It suggests the possibilities to attain the drag reduction on liquid-infused surfaces with random features. To explore this further, here we investigate a surface that is both random in the two-dimensional arrangement of surface topography, but also random in the height of the surface features.

In order to investigate the stability of the lubricant layer on liquid-infused surfaces with three-dimensionally random features, we chose to investigate the effectiveness of a series of sanded PTFE surfaces and measured the pressure drop across these surfaces in the microchannel. Time-resolved pressure drop measurements of the liquid-infused PTFE surfaces are shown in Figure 27. In this figure, the pressure drops of the PTFE surfaces sanded with 180-grit (RMS roughness of 15.4µm), 240-grit (RMS roughness of 13.7µm), and 320-grit (RMS roughness of 10.9µm) sandpaper are compared for the same viscosity ratio between the aqueous phase and the lubricating oil, $\mu_w / \mu_o = 9.2$, and at a constant average flow velocity of *U*= 0.4mm/s and a constant capillary number of *Ca*=0.001. All the surfaces tested exhibited both a short-time (3hrs) and a long-time (12hrs) plateau in the measured pressure drop. The short time plateau was reached after approximately thirty minutes to one hour of flow. Due to the large viscosity of the working fluid and the low flow rates tested this relatively long start-up time was needed for the working fluid to fully fill the microfluidic device and for the flow to reach equilibrium. Similar start-up times were observed for the case of all sanded PTFE surfaces and were found to be independent of surface roughness. The minimum pressure drops were maintained for approximately two hours regardless of the microstructures on the surfaces. As was observed for air-infused superhydrophobic sanded PTFE surfaces [24], the 240-grit sanded surface was again found to exhibit the lowest pressure drop of the three sanded

PTPE surfaces tested. After about three hours, however, depletion of the lubricant layer was observed through both microscope imaging and oil droplets collecting in the downstream tubing. As a result of the long time oil depletion, a gradual increase in the measured pressure drop was observed. At large times, unlike the precisely patterned liquid-infused surfaces, the pressure drop settled into a long-time plateau, similar to the value observed for these PTFE surfaces in the Wenzel state when the surface roughness was fully wetted by water. These measurements indicate that after 10hrs of flow at a capillary number of Ca=0.001 most of the lubricant infused in these sanded PTFE surfaces was depleted from between the surface structures and was replaced by the aqueous working fluid.

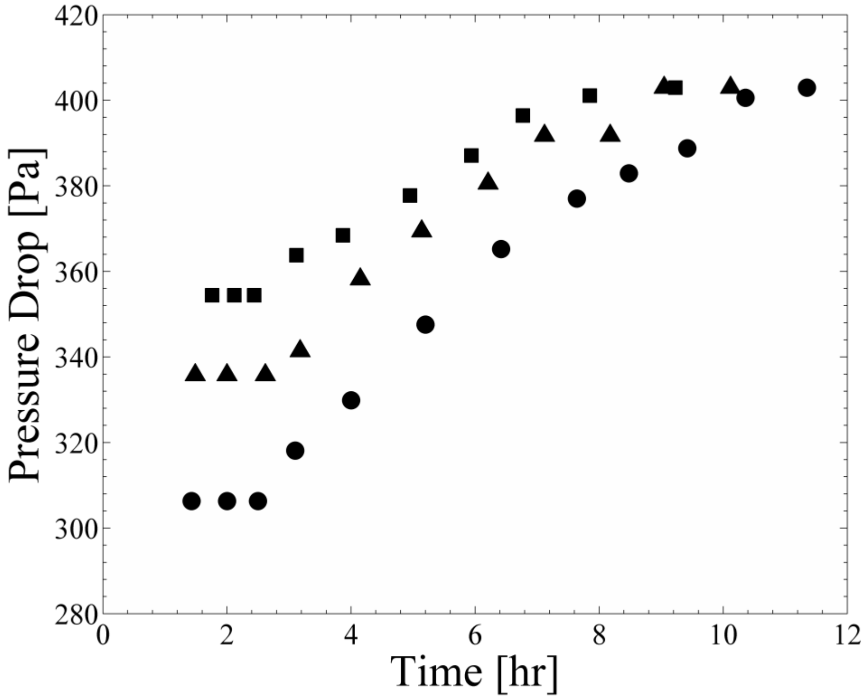

Figure 27: Pressure drop as a function of time for a series of liquid-infused superhydrophobic sanded PTFE surfaces showing the longevity of the lubricating layer. The experimental data include PTFE surfaces sanded with a series of different sandpaper with grit designation of (square) 180-grit, (circle) 240-grit, and (triangle) 320-grit for the viscosity ratio of $\mu_w / \mu_o = 9.2$. The RMS surface roughness was estimated as 15.4µm, 13.7µm, and 10.9µm for 180-, 240-, and 320-grits of sandpaper based on the literature [33]. All experiments were performed at a constant flow velocity of *U*=0.4mm/s and a constant capillary number of *Ca*=0.001. The pressure drop data have a maximum uncertainty of 14 Pa.

To understand the delayed depletion of the lubricant layer on randomly rough surfaces, the surface profile of the PTFE surface sanded with grit designation of 240-grit was measured by Dektak profilometer equipped with stylus of 12.5μm. Figure 28 shows a 150μm wide slice of the profilometer data for sanded PTFE chosen because it was a good representative of the overall surface topography. A sketch of our physical interpretation of the drag reduction data has been superimposed over the surface profile. The standard deviation of the surface roughness was measured to be ± 3.1μm for the range of 150μm shown in Figure 28, but, if the surface roughness measured across the entire channel is considered, a standard deviation of ± 6.5μm was measured. During preparation of the liquid-infused surfaces, the lubricant was applied with little shear stress as it was allowed to wick into the surface features and drain slowly down the surface under gravity. As a result, the lubricating oil is likely trapped between the very tallest protrusions of the surface at the start of the drag reduction experiments. We have represented our proposed initial conditions of the liquid-infused surfaces schematically in Figure 28a. In this hypothetical scenario, the resulting liquid-infused surfaces contain large deep pools of oil and very few solid protrusions. As a result, at the start of each experiment, the interface is nearly shear-free with only a small number of isolated no-slip patches corresponding to the tallest peaks in surface roughness. Under shear flow, these pools will slowly drain, but due to the interconnectivity of the surface, they can be maintained by re-circulation through the three-dimensional surface topography. We believe that these large nearly shear-free lubricant areas are what lead to the initial minimum in the pressure drop measurements observed for the first three hours of the experiments as shown in Figure 27. This emphasizes the importance and value of three dimensional random surface roughness for establishing and maintaining liquid-infused surface drag reduction. With time, the lubricant layer was depleted, and the depth of the oil layer was slowly reduced. A medium times, $t > 3$ hrs, the oil layer was stripped sufficiently to begin to reveal additional solid surface features. Finally, at long times, most oil reservoirs have been depleted and only isolated patches of oil on an otherwise rough solid surface remained as we have shown schematically in Figure 28b. This depletion results in the long time, $t > 12$ hrs, plateau observed in the data in Figure 27, which approaches the pressure drop associated with the Wenzel state.

Note that, at short times, the PTFE surface sanded by 240-grit sandpaper had the lowest pressure drop amongst the sanded surfaces tested while all surfaces approached the same long time plateau. This trend is consistent with the superhydrophobic drag reduction measurements for sanded PTFE surfaces in the literature [24]. For superhydrophobic drag reduction, Song et al. [24] argued that the 240-grit sandpaper optimized the feature spacing compared to other sandpaper grits. Increasing the grit size (decreasing the grit designation) increases the width and depth of the scratches and grooves imparted to the PTFE by the sanding process [33]. As the spacing between surface features increases, the slip length and drag reduction are known to increase [18, 116]. However, beyond a critical feature spacing, the air-water interface cannot support a large pressure difference between the water and the air and can collapse to the Wenzel state under flow conditions. For the superhydrophobic sanded PTFE surfaces this hypothesis is supported by an increase in contact angle hysteresis for sandpaper grit designations smaller than 240. Here, however, the lubricating oil is incompressible and a similar transition is not expected. In fact, the advancing contact angles and contact angle hysteresis for all three liquid-infused surfaces are quite similar at roughly $\theta_A = 100^o$ and $\theta_H = 4^o$ for the 180-grit, 240-grit, and 320-grit sanded PTFE surfaces. The increase in pressure drop from 240-grit to-180 grit is therefore unlikely due to a loss of lubricant from the surface but instead due to the nuances of the initial oil coverage as sketched out in Figure 28.

Figure 29 shows the time evolution of the pressure drop on the liquid-infused PTFE surface sanded by the 240-grit sandpaper (RMS roughness of 13.7µm) for three different viscosity ratios. In these measurements, the capillary number was fixed to Ca = 0.001 in order to keep the balance between interfacial and viscous stresses consistent between experiments. This was achieved by increasing the flow rate as the viscosity of the working fluid was reduced to achieve a smaller viscosity ratio. As the viscosity ratio was reduced from μ_w / μ_o= 9.2 to 0.2, the short time minimum in the observed pressure drop was achieved more quickly. This is a direct result of the increased flow rate needed to maintain a constant capillary number of Ca=0.001. For the case of a viscosity ratio of $\mu_w / \mu_o = 0.2$, the short-time minimum pressure drop was maintained for just one hour. In order to maintain a constant capillary number, the average velocity in the microchannel for the $\mu_w / \mu_o = 0.2$ case was nearly 50 times larger than the $\mu_w / \mu_o = 9.2$ case yet the oil was stripped in only 1/3 the time.

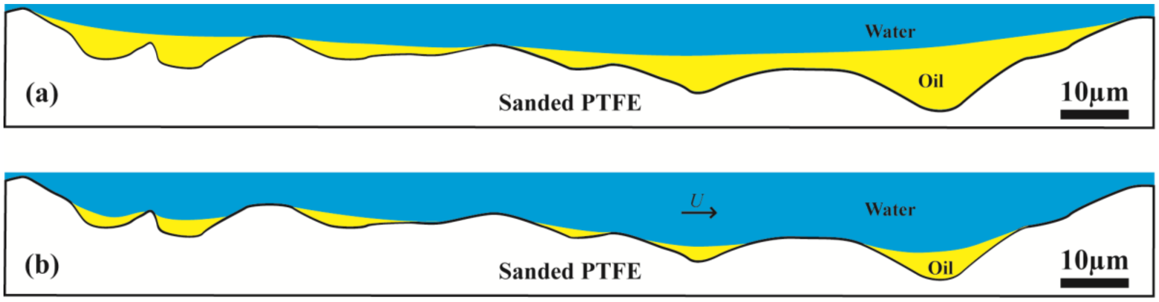

Figure 28: The lubricant pools on the PTFE surface sanded with grit designation of 240-grit (RMS roughness of 13.7μm). This 150μm long slice of the surface was taken from actual profilometry measurements. It is a representational slice of the sanded PTFE surface. Superimposed on the surface topography is a schematic diagram of the evolution of the oil-water interface which we believe help to explain the experimental results. The initial condition of the surface is shown in (a) while in (b) the long time LIS is shown with oil depleted from the surface.

In order to understand the difference in depletion rate of the oil layer quantitatively, we consider the laminar pressure driven flow between two parallel plates. The top plate is no-slip smooth surface. The bottom plate is slippery rough surface containing oil layer with thickness of *t* and viscosity of μ_o. This oil layer separates the working fluid with viscosity of μ_w from the bottom plate, generating the height of the water phase, *h-t*. Here, *h* is the channel height. By matching shear stress at the oil-water interface, $\mu_w(\partial u_w / \partial y) = \mu_o(\partial u_o / \partial y)$, and assuming Poiseuille flow in the channel, the velocity at the interface is predicted to be $u_o = \left(Ca \frac{\sigma}{\mu_o} \frac{\mathrm{t}}{(\mathrm{h}-\mathrm{t})} \right) \left(1 + \frac{\mu_w}{\mu_o} \frac{\mathrm{t}}{(\mathrm{h}-\mathrm{t})} \right)^{-1}$. In our experiment, the microchannel height was measured to be 150µm and the oil layer could be assumed to be same order of grit size of the sandpaper, 30µm. From this calculation, the interfacial velocity for the μ_w / μ_o=0.2 case predicted to be three times larger than that of μ_w / μ_o=9.2 case. This result is consistent with our experimental observation seen in Figure 29 which indicate the μ_w / μ_o=0.2 case begins to lose oil after roughly one hour while the μ_w / μ_o=9.2 case lasts for almost 3 hrs. Thus, it is clear that capillary number alone does not fully describe the dynamics of lubricating oil depletion. The viscosity ratio also plays an important role as it sets the magnitude of the resulting oil-water interfacial velocity which dictates the mass flux of lubricating oil within liquid-infused surfaces.

Note that the long-time plateau was not observed for the case of a viscosity ratio of $\mu_w / \mu_o = 0.2$ due to the limited capacity of the syringes used in the syringe pump and the fact that even as the flow rate was 50 times larger than the $\mu_w / \mu_o = 9.2$ case, the oil was removed only three times as fast. As a result, a nearly 20 fold increase in syringe volume would have been required to reach steady state for the $\mu_w / \mu_o = 0.2$ case.

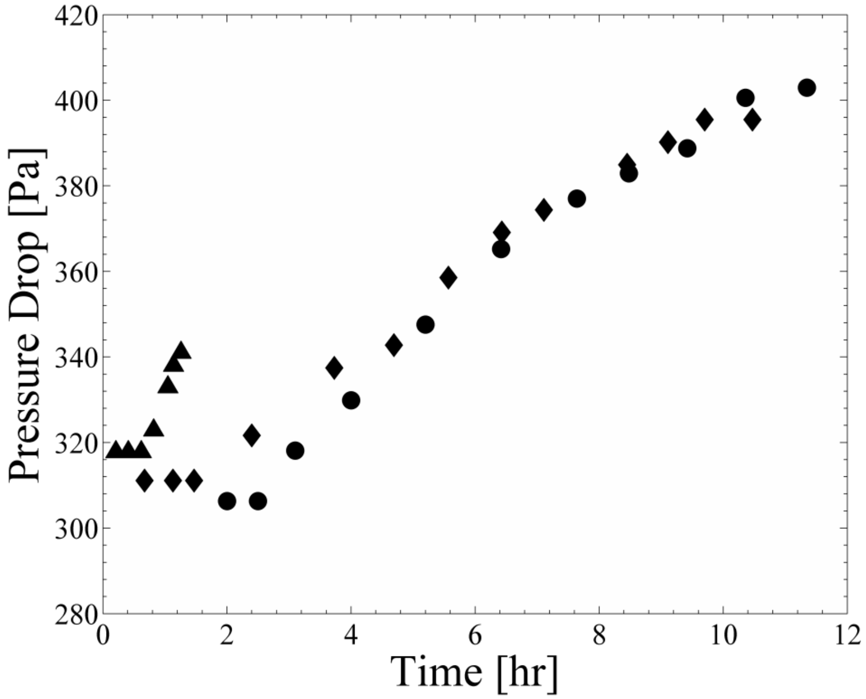

Figure 29: Pressure drop as a function of time for the liquid-infused superhydrophobic sanded PTFE surfaces sanded with a grit designation of 240-grit (RMS roughness of 13.7µm) at *Ca*=0.001. The experimental data include the viscosity ratio of (triangle) $\mu_w / \mu_o = 0.2$, (diamond) $\mu_w / \mu_o = 5.2$ and (circle) $\mu_w / \mu_o = 9.2$. Due to the change in the viscosity of the aqueous phase, to maintain a constant capillary number, the flow velocity increase with decreasing viscosity of the aqueous phase. The pressure drop data have a maximum uncertainty of 14 Pa.

From the longevity studies of the lubricant layer in Figure 29, the effect of viscosity ratio on liquid-infused surfaces drag reduction can be quantified by comparing the average values of the short-time plateau in the pressure drop data to a smooth PTFE surface. A minimum of three measurements with the microfluidic device was recorded. Between each experiment, the device was broken down and reassembled to ensure the repeatability and the robustness of the measurement. In addition to the average pressure drop reduction, the slip length, $b = HD_R / (3 - 4D_R)$, was calculated based on the pressure drop reduction, D_R, and the channel height, H [18].

From the data in Figure 29, a clear increase in the pressure drop reduction and slip length can be observed with increasing viscosity ratio for the 240-grit sanded PTFE surface. The data show linear dependence on viscosity ratio. The mean pressure drop reduction and the slip length on the liquid-infused surfaces were measured to be 10 ± 12 %, 12 ± 11%, and 13 ± 11% and 6 ± 7 µm, 7 ± 7 µm, and 8 ± 7 µm for the viscosity ratio of 0.2, 5.2, and 9.2, respectively. This linear relationship is expected as it is predicted by the theory developed by Ybert et al. [116], and shown experimentally by Solomon et al. [55] for flow within a cone-and-plate rheometer. The error bars on the data represent both the uncertainty of the individual measurements, but also the uncertainty of the channel height which is needed to determine the smooth pressure drop. As discussed earlier, the variation in the surface roughness of the sanded PTFE surface was quite large resulting in a ± 6µm uncertainty in the microchannel height. Within those error bars the trends in drag reduction and slip length are significant, but these measurements show the challenges in making drag reduction/slip length measurements when the slip length is close to uncertainty in the channel dimensions.

5.4 Conclusions

The pressure drop measurements on the liquid-infused superhydrophobic surfaces were performed through a microchannel by varying the surface topography and the viscosity ratio between the water and lubricant phases. A low viscosity, immiscible and incompressible silicone oil was filled to the gaps between structures of superhydrophobic surfaces. The patterned surfaces with micro-posts and micro-ridges and randomly rough PTFE surfaces sanded by different grits of sandpapers were prepared for testing surfaces. Several aqueous glycerin solutions with different viscosities were used to change the viscosity ratio. The precisely patterned superhydrophobic surface containing constant height posts and ridges was found ineffective at maintaining a lubricant layer within the microstructure for any measurable length of time even in low capillary numbers, $Ca \approx 0.001$. The shear stress exerted from external flow resulted in a non-zero velocity at the oil-water interface, resulting in a fast depletion of the lubricant from between the micro-features of liquid-infused surfaces. Conversely, the randomly rough PTFE surfaces, the lubricating oil layer was found to be much longer lived. As a result, a minimum pressure drop corresponding to significant drag reduction was easily maintained for a viscosity ratio of $\mu_w / \mu_o = 9.2$ flowing at $Ca = 0.001$ for more than three hours. This result was found to be independent to the size of the microstructures introduced into the PTFE by different grit sandpaper. We believe that this is because the three-dimensional patterned surface provided the added pathways for re-circulation of the lubricant. Due to the presence of a small number of high spots (tall posts) on the sanded PTFE surface, it was possible for oil to reside within large pools with nearly complete coverage of the surface topography. Over time the slow depletion of the lubricant layer was found to accelerate most likely as these large oil reservoirs were depleted and its level fall below the top of the tallest surface features. The result was a slow increase in the pressure drop over ten hours before second plateau of the pressure drop was reached. This final pressure drop was equivalent to a Wenzel state. The effect of the viscosity ratio on liquid-infused surfaces was also studied. For a constant capillary number experiment, the lower viscosity ratio liquid-infused surfaces were found to deplete oil and lose their effectiveness more quickly. However, if the experiment were run at constant flow rate the longevity would increase with reduced viscosity ratio. Our experiments show that the velocity at the oil-water interface is the key to understand lubricant depletion. Finally, the pressure drop reduction and the corresponding slip length were found to increase with increasing viscosity ratio.

CHAPTER 6

DROPLET IMPACT DYNAMICS ON LUBRICANT-INFUSED SUPERHYDROPHOBIC SURFACES

6.1 Introduction

The development of superhydrophobic surfaces was inspired by the extreme water repellency observed in plants [8] and insects [117, 118] around the world. These superhydrophobic surfaces are comprised of hydrophobic surfaces containing micron and/or nanometer-sized surface structures. Due to surface tension, air can be trapped between peaks of surface roughness thus preventing water from penetrating into the gaps or valleys between surface protrusions. The presence of the resulting air-water interface can increase the advancing contact angle with water towards 180° while eliminating contact angle hysteresis [31, 32, 119, 120]. The air-water interface is nearly shear-free. As a result, superhydrophobic surfaces are useful in a number of promising applications such as laminar and turbulent drag reduction [15, 18, 19, 21, 23-25], anti-icing [28, 29], and anti-fouling [26, 27]. Unfortunately, there are a number of situations in which the great potential cannot be fully realized. For example, the air-liquid interface can collapse under large static and/or dynamic pressure [15, 50] as well as the presence of any mechanical defects on the surface [3, 50]. Furthermore, the air-water interface does not repel low surface tension liquids even under low static and/or dynamic pressure without the inclusion of special surface features like a re-entrant structure [37].

Recent developments in lubricant-infused surfaces (LIS) have begun to address many of the implementation issues associated superhydrophobic surfaces [49, 53]. In LIS, an immiscible, incompressible, and low-viscosity lubricant is coated onto a superhydrophobic surface where it is deposited into the surface structure. Smith et al. [54] showed that depending on the interfacial tension among the oil, water, and surface, the lubricating oil will either become impregnated within the surface roughness leaving the tops of the roughness exposed to the water or the lubricating oil will fully encapsulate the surface features. The latter is beneficial for enhancing droplet mobility, but is prone to faster lubricant depletion rates.[54] The incompressible lubricant layer resists large static pressure and repels various kinds of liquid including those with low surface tensions [49]. Furthermore, the lubricant layer was found to restore a liquid-repellent property after abrasion and impact of liquids unlike the air-infused superhydrophobic surfaces. A number of research group have begun to investigate other potential uses of lubricant-infused superhydrophobic surfaces including for drag reduction, anti-icing, and anti-bacterial applications [51, 52, 54-57, 113, 114, 121, 122].

For lubricant-infused surfaces, the effect of ratio between viscosity of the water, μ_w , and the oil phases, μ_o , is always an important factor to understand. On superhydrophobic surfaces filled with air, viscosity ratio between water and air is approximately $\mu_w / \mu_{air} = 55$ at room temperature. This large viscosity ratio justifies the frequent assumption that the air-water interface is shear-free. Solomon et al. [55] showed that the frictional stress along a lubricant-infused surface can be reduced by increasing the viscosity ratio between the water and oil phases, μ_w / μ_o. Their measurement of LIS using a cone-and-plate rheometer showed a maximum drag reduction and a maximum slip length of 16% and 18μm, respectively, at a viscosity ratio of $\mu_w / \mu_o = 260$. Rosenberg et al. [121] recently showed drag reduction measurements on the lubricant-infused surface in the Taylor-Couette flow. They demonstrated that no drag reduction was attained at a viscosity ratio of $\mu_w / \mu_o = 0.03$. However, the drag reduction was found to increase from 5% to 14% as a viscosity ratio was increased from $\mu_w / \mu_o = 0.67$ to $\mu_w / \mu_o = 2.7$ [121]. Viscosity ratio has also been shown to affect droplet impact dynamics on lubricant-infused surfaces. Recent studies by Lee et al. [57] and Hao et al. [122] demonstrated that the retraction of a droplet from a lubricant-infused surface after impact was delayed significantly by increasing the viscosity of the infused oil or, equivalently, by reducing the viscosity ratio between the impinging water droplet and the infused oil layer. No differences in spreading dynamics were observed. This could be because all of the viscosity ratios tested were quite small, $\mu_w / \mu_o \ll 1$. As a result, many of the possible difference in droplet spreading dynamics, especially for lubricant-infused surfaces where the viscosity ratio was well above $\mu_w / \mu_o > 1$, could not be observed.

In this chapter, the spreading and retraction dynamics of droplet impacting on a series of lubricant-infused surfaces will be presenting. However, unlike previous studies, we will increase the viscosity ratio to values larger than one to more fully investigate the effect of the viscosity ratio on the spreading and retraction dynamics of impacting droplets on LIS. Our experimental results will be compared against a theoretical model which predicts the increase in the maximum diameter of droplet after impacting on lubricant-infused surfaces with increasing viscosity ratio and reduced oil viscosity.

6.2 Experimental Setup

A standard experimental setup for the droplet impact studies was used. For the impinging droplets, a 55wt% glycerin/water solution was used to increase the viscosity ratio. The aqueous glycerin droplets with an initial diameter of D_0 = 3.3mm, a surface tension of σ_w=67mN/m and a viscosity of μ_w= 6mPas were generated using a syringe pump (KD Scientific Model 100) from a syringe tip attached to plastic tubing and suspended a distance between 0 and 2m above a levelled glass table. The droplets were accelerated by gravity, and their velocity at impact and exact diameter were measured through analysis of high speed video camera (Phantom 4.2) images.

A series of test surfaces were placed at the impact location. These surfaces include a smooth polytetrafluoroethylene (PTFE) sheet purchased from McMaster-Carr which was used as a baseline along with a series of superhydrophobic and lubricant-infused surfaces. To produce the superhydrophobic surfaces, the smooth PTFE surface was roughened by sanding it with a 240-grit sandpaper to introduce randomly rough micro-scale structures using the sanding technique described in Nilsson et al. [33]. This grit size is known to produce a superhydrophobic surface with a high advancing contact angle, $\theta_A = 150^\circ$, and an extremely low contact angle hysteresis, $\theta_H = \theta_A - \theta_R = 4^\circ$ [33]. In addition, these sanded PTFE surfaces have been shown to produce significant laminar drag reduction where tested in microfluidic channel experiments [24]. The superhydrophobic 240-grit sanded PTFE surface used here has been shown to result in a slip length of b = 20μm. Note that the RMS surface roughness was estimated as 5.6μm and 13.7μm for the smooth PTFE surface and the sanded PTFE surfaces, respectively, based on the literature [33].

Several silicone oils (Cannon Instrument Company) with the viscosity of μ_o = 5, 14, 100mPas and a surface tension of σ_o = 20mN/m were infused into superhydrophobic PTFE surfaces by allowing the oil to wick into the surface topography. Excess silicone oil was removed by a doctor blade to produce uniform and thin oil layer. The resulting viscosity ratio between impacting droplets and the infused oil film, $\mu_{ratio} = \mu_w / \mu_o$, was varied between $0.06 < \mu_{ratio} < 1.2$. In microfluidic channel experiments [123], the lubricant-infused surfaces have shown to produce increase in pressure drop reduction and slip length with increasing the viscosity ratio from $\mu_{ratio} = 0.2$ to $\mu_{ratio} = 9.2$. The pressure drop reduction was found to increase from 10% to 13% while the slip length was found to increase from 6μm to 8μm (Kim & Rothstein 2016). The contact angle hysteresis of water on all three lubricant-infused PTFE surfaces were measured and found to be very similar to the air-infused superhydrophobic surface, $\theta_H = 2.3^\circ \pm 1.3$, $4.1^\circ \pm 1.0$, and $2.4^\circ \pm 1.1$ for the viscosity ratio of μ_{ratio} = 0.06, 0.43, and 1.2, respectively. However, the advancing contact angles of water on the lubricant-infused surfaces were measured to be significantly lower than the air-infused case; $\theta_A = 102.4^\circ \pm 1.1$, $101.8^\circ \pm 0.9$, and $100.5^\circ \pm 0.7$ for the viscosity ratio of μ_{ratio} = 0.06, 0.43, and 1.2, respectively. The difference in advancing contact angle between the lubricant-infused surfaces and the superhydrophobic surface is due to the reduction in the interfacial tension as one replaces the air trapped within the superhydrophobic surface with silicone oil. For a superhydrophobic surface in Cassie state, $\theta_{Cassie} = \cos^{-1}\left(-1+\phi_S\left(1+\cos\theta\right)\right)$.[6] Here, ϕ_S is the fraction of the surface contact with the drop that is solid and θ is the contact angle made between the water and a smooth surface. For an impregnated lubricant-infused surface, $\theta_{LIS,i} = \cos^{-1}\left[(\gamma_{OA}-\gamma_{WO})/(\gamma_{OA}+\gamma_{WO})+\phi_S\left(1+\cos\theta\right)\right]$, where γ_{OA} is the interfacial tension between the oil and air, γ_{WO} is the interfacial tension between the water and oil, and γ_{WA} is the interfacial tension between the water and air. For a fully encapsulated lubricant-infused surface, the equilibrium contact angle of water is given by $\theta_{LIS,e} = \cos^{-1}\left[\left(\gamma_{OA}-\gamma_{WO}\right)/\left(\gamma_{WO}+\gamma_{OA}\right)\right]$.[57] As we will show in the results and discussion section, the difference in advancing and receding contact angle between the air-infused surface and lubricant-infused surfaces has a significant effect on the droplet impact dynamics.

The droplet impact velocity, U_0, was varied from 0.7m/s to 1.9m/s by changing the height from which the droplet was released. The resulting Weber number at impact, $We = \rho_w U_0{}^2 D_0 / \sigma_w$, thus ranged from $25 < We < 172$. Here, ρ_w is the density of the droplet, U_0 is the drop impact velocity, D_0 is the initial diameter of the droplet before impact, and σ_w is the surface tension of the droplet. The spreading and retraction dynamics of the droplets on each surface were recorded by a high speed camera (Phantom V4.2) with a frame rate of 2200Hz. A series of images were imported into the program ImageJ, and the evolution of the droplet diameter, spreading and retraction velocities and the dynamic contact angle were measured as a function of time after impact. The frame containing the first contact of the droplets on the surfaces ($t \cong 0$ms), is shown in the first column of Figure 30. This time is only as precise as the time between frames (~ 0.46 ms) and as seen in Figure 30, the first observed instance of impact is different for each measurement. In order to more accurately quantify the exact impact time for later analysis, the distance between the center of the droplet and the testing surface was measured and, in combination with the impact velocity, used to calculate the exact time of impact for each experiment. In this way, the resolution of the impact time was reduced by a factor of nearly ten to 0.06ms for the *We*=132 case, and even better for lower weber numbers. The droplet impact tests on each surface were conducted a minimum of three times at several different positions along the surface to improve the confidence in the repeatability of these experiments. From these measurements, a maximum uncertainty in the maximum droplet diameter, $D_{\max}$, was calculated to be 0.15mm, which is 4.6% of the initial droplet size (D_0=3.27mm) while the maximum uncertainty of the droplet spreading and retraction velocities was calculated to be 0.022m/s, which is 1.4% of the impact velocity (U_0=1.62m/s) at *We*=132.

6.3 Results and Discussion

In Figure 30, a series of time-resolved images of spreading and retraction dynamics of droplets on the smooth, air-infused, and lubricant-infused PTFE surfaces are shown. Here, we provide two different Weber number cases, *We*=52 and *We*=132. The smooth PFTE surface (SM) can be considered a zero viscosity ratio experiment, $\mu_{rat} = 0$, while the air-infused superhydrophobic PTFE surface (SHS) represents the highest viscosity ratio case tested, $\mu_{rat} = 300$. Note that for the lubricant-infused PTFE surfaces (LIS), the number following ‘LIS’ indicates the viscosity of the silicone oil used.

As can be seen in Figure 30, the droplet impact dynamics are qualitatively similar on all surfaces. Upon impact, the droplets deform to a pancake shape, reach a maximum diameter/deformation, and then retract to form a Worthington jet. The details of the dynamics of spreading and retraction of the droplets were found to depend on the nature of the surface, rough or smooth, and the viscosity of the infused silicone oil. We will begin by discussing the dependence of the impact dynamics on the viscosity ratio of the three lubricant-infused surfaces before comparing the LIS results to the droplet impact on smooth and superhydrophobic PTFE surfaces. At all Weber numbers tested, including the two presented in Figure 30, the maximum spreading diameter of the droplet was found to increase with decreasing viscosity of the infused silicone oil layer. This can be observed directly from the third column of images in Figure 30, which was very close to the instant the droplet reached its maximum. This increase in maximum droplet diameter is a direct result of the reduced shear stress and large slip length that has been observed for the flow over lubricant-infused surfaces in the past [55, 121, 123]. As the viscosity of the silicone oil was decreased, the shear stress between the spreading droplet and the oil layer infused within the roughened PTFE surface were reduced. As a result, the reduction in energy dissipation during the droplet impact and subsequent spreading increased the maximum diameter of the droplet with decreasing oil viscosity. Note that the maximum spreading diameter observed for the highest viscosity silicone oil tested, LIS 100, was in fact very close to the measurement for droplet impacts on the smooth PTFE surface. This is likely because the viscosity ratio between the droplet and the lubricant infused in the LIS 100 surface was quite small and could be thought of as essentially zero, $\mu_{rat} = 0.06$. As a result, little drag reduction is expected in this case during the spreading phase. Interestingly, the maximum diameter at the lowest viscosity lubricant-infused surface, LIS 5, did not consistently follow the trends of the superhydrophobic, air-infused case. We will discuss this observation in more detail later in the paper.

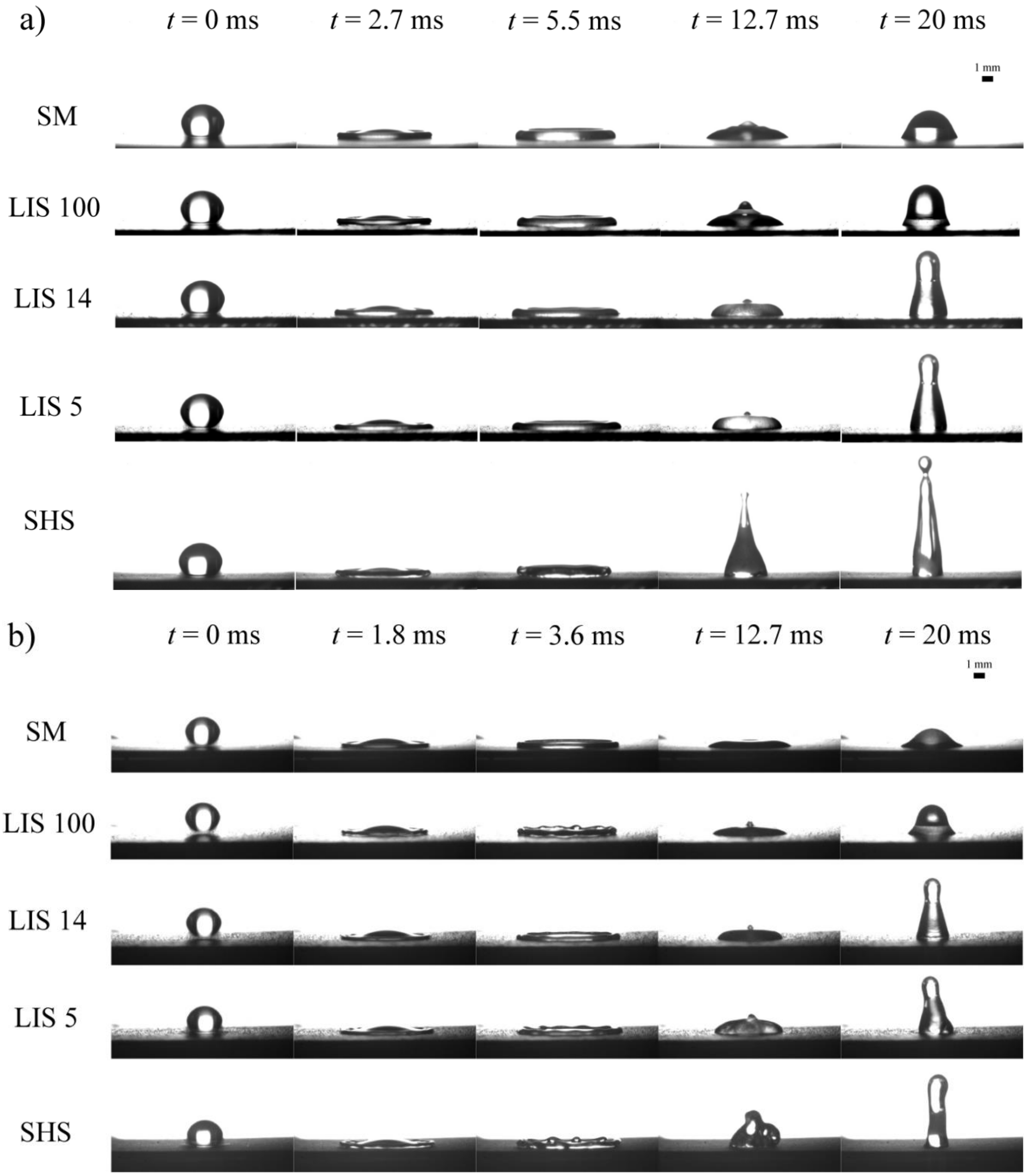
a)
t = 0 ms
t = 2.7 ms
t = 5.5 ms
t = 12.7 ms
t = 20 ms
1 mm
SM
LIS 100
LIS 14
LIS 5
SHS
b)
t = 0 ms
t = 1.8 ms
t = 3.6 ms
t = 12.7 ms
t = 20 ms
1 mm
SM
LIS 100
LIS 14
LIS 5
SHS

Figure 30: Time evolution of an aqueous glycerin drop (μ=6cP) impacting on a series of test surfaces at Weber numbers of (a) *We*=52 and (b) *We*=132. The surfaces include: SM-smooth, SHS-superhydrophobic air-infused, LIS- lubricant-infused. For the lubricant-infused surface, the viscosity of the silicone oil in cP is included following LIS.

The differences in the droplet impact dynamics were examined more quantitatively by tracking the time evolution of the drop diameter as it spreads on each surface from the high speed images. In order to remove the influence of a drop size variation, each measurement was non-dimensionalized by the initial drop size. The results for low and high Weber number, *We*=52 and *We*=132, respectively, are presented in Figure 31a and 31b as a function of time. As seen in Figure 31a and 31b, the maximal deformation of the droplet was found to increase from $D_{\max}/D_0 = 2.29$ to $D_{\max}/D_0 = 2.51$ and from $D_{\max}/D_0 = 2.85$ to $D_{\max}/D_0 = 3.02$, respectively, as the viscosity of the silicone oil was decreased. As discussed previously, the reduction in shear stress at the oil-water interface with decreasing oil viscosity likely causes the increase in the diameter of the impacting droplets. The reduction in viscous dissipation during the spreading phase can also be observed in the spreading velocities. The spreading velocities were calculated from the droplet diameter data in Figure 31 and are presented in Figure 32. As seen in Figure 32a and 31b, the spreading velocities are initially close to the impact velocity (U_o=1.0 m/s at *We*=52 and U_o=1.6 m/s at *We*=132) during the first stage of the impact. The spreading velocities then decreases over time as kinetic energy is converted to potential energy through interface deformation and is dissipated due to the shear at the oil-water interface. During the spreading phase, the droplet spreading velocity on the LIS 5 was consistently larger than the LIS 100. This was more obvious at *We*=52 as shown in Figure 32a. No significant differences in spreading velocity were observed between the LIS 5 and LIS 14 cases. In order to make Figure 32 more readable, we have therefore chosen to present the data for just LIS 5.

Note that both the spreading diameter and velocity of the LIS 100 case approaches the results from the smooth PTFE surface. This is a direct result of the large lubricant viscosity. It is also in agreement with the observation in the literature for $\mu_{ratio} \ll 1$ [57].

As was observed from the images in Figure 30a, at the lower Weber numbers tested, the droplets impacting on the LIS 5 surface were found to spread further than the air-infused superhydrophobic surface (SHS). This is surprising given that viscosity ratio between the droplet and the air is 250 times larger than for the LIS 5 surface. This clearly does not follow the trend observed for the three lubricant-infused surfaces which show a clear trend of the maximum diameter of the droplet and the spreading velocity which grows with increasing viscosity ratio or equivalently decreasing lubricant viscosity. In fact, at We=52, the droplets impacting the LIS 5 surface spread nearly 10% further than the superhydrophobic surface. At the same Weber number, the peak spreading velocities are nearly 60% faster on the LIS 5 compared to the superhydrophobic surface. Interestingly, both of those trends reverse at a Weber number of We=132. These observations point to two important differences between superhydrophobic and liquid-infused surfaces. First, their advancing contact angles are very different, $\theta_A = 150^\circ$ for SHS and $\theta_A = 101^\circ$ for LIS 5. Due to its larger contact angle, we will show that deformation of the impacting droplet requires 54% more capillary energy for the same deformation. Second, even though the energy dissipation associated with droplet spreading is less for the superhydrophobic surfaces compared to the liquid-infused surfaces, there is additional energy dissipation for the superhydrophobic case associated with the dynamics of the Cassie to Wenzel transition beneath the impacting droplet. This dissipation mechanism does not exist for any of the LIS cases as the oil is incompressible and able to withstand the large pressures produced at impact. These differences appear to become less significant at larger impact velocities as the reduction in energy dissipation during droplet spreading on the superhydrophobic surfaces appears to dominate the spreading dynamics beyond impact Weber numbers of approximately, $We>100$.

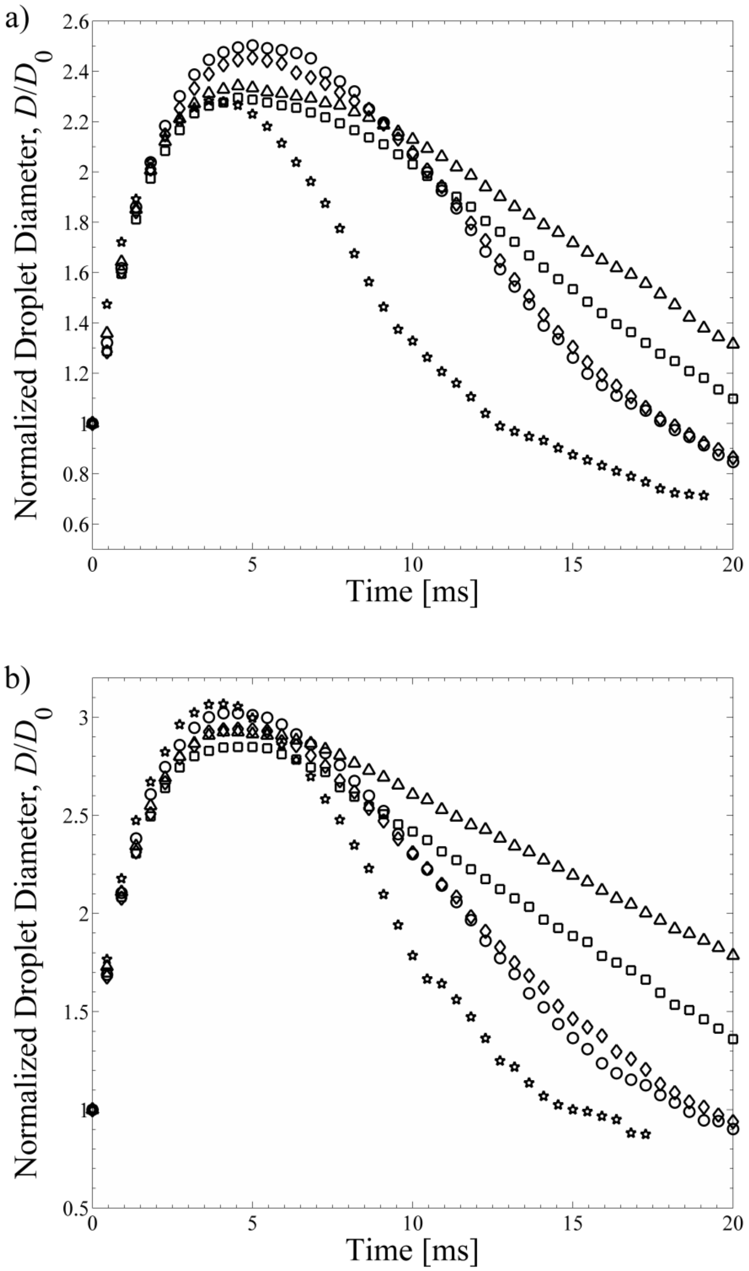

Figure 31: Time evolution of the diameter of the impacting drop normalized by the initial drop diameter at a Webber number of (a) *We*=52 and (b) *We*=132. The experimental data include: lubricant-infused roughened PTFE surfaces with 5cP silicone oil (circle), 14cP silicone oil (diamond), and 100cP silicone oil (square) as well as smooth PTFE surface (triangle) and air-infused superhydrophobic PTFE surface (star).

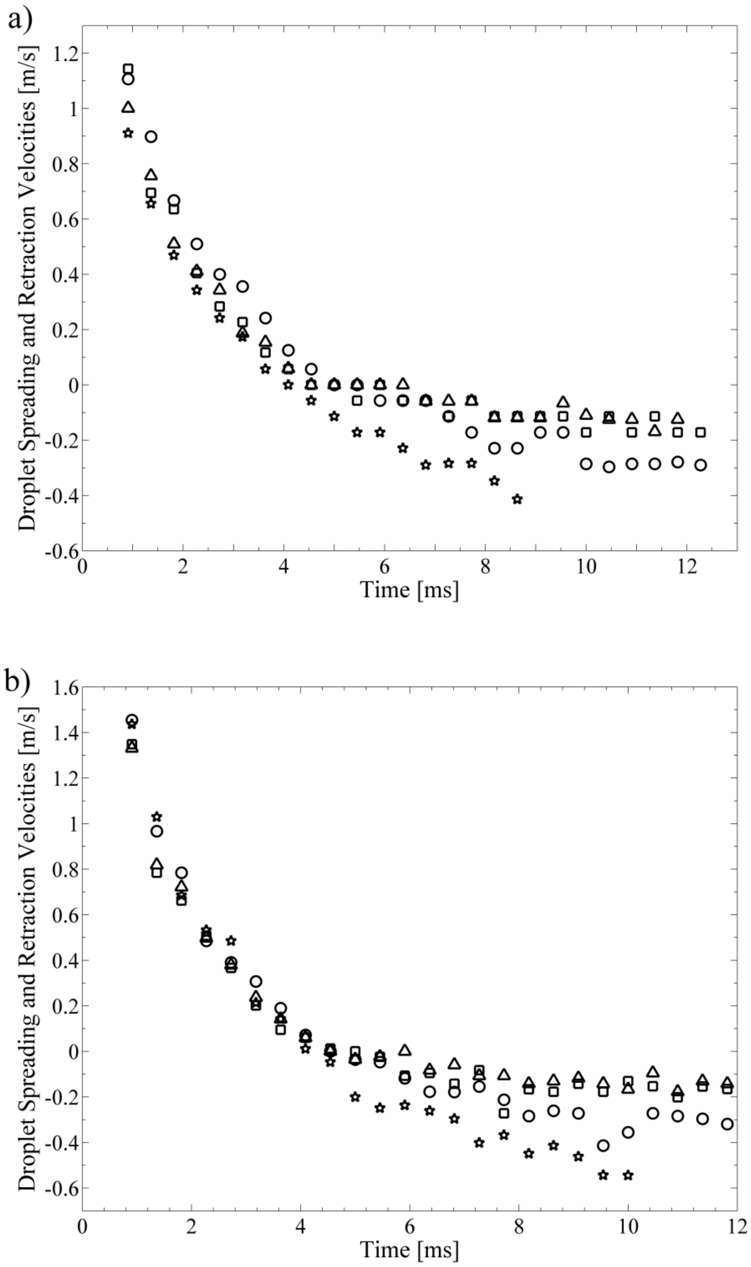

Figure 32: Time evolution of the spreading (+ve) and retraction (-ve) velocities of droplet impacts on a number of different surfaces at a Weber number of (a) *We*=52 and (b) *We*=132. The experimental data include: lubricant-infused roughened PTFE surfaces with 5cP silicone oil (circle) and 100cP silicone oil (square) as well as smooth PTFE surface (triangle) and air-infused superhydrophobic PTFE surface (star).

In order to better understand the differences in the maximum spreading diameter between superhydrophobic and lubricant-infused surfaces, we considered the energy balance of an impacting droplet. In the calculations that follow, the shape of the droplet was assumed to be spherical before impact and was approximated as a flattened disk after impact. This second assumption is only truly valid for a highly deformed drop near the point of the maximum spreading as seen in Figure 30. The initial kinetic energy, KE_1, and surface energy, SE_1, of the spherical droplet are given by

$$KE_1 = \frac{1}{12}\pi\rho_w D_0^3 U_0^2 , \tag{16}$$

$$SE_1 = \pi D_0^2 \sigma_w . \tag{17}$$

The kinetic energy, KE_2, and surface energy, SE_2, of the disk-like droplet after the impact are given by [124]

$$KE_2 = \frac{1}{24}\pi\rho_w D^3 U_S^2 , \tag{18}$$

$$SE_2 = \frac{\pi}{4} D^2 \sigma_w (1-\cos\theta_A) . \tag{19}$$

Here, D is instantaneous droplet diameter, U_s is the instantaneous droplet spreading velocity, and θ_A is static advancing contact angle. The kinetic energy of the spreading droplet after impact, KE_2, was calculated from a radial velocity profile calculated from a lubrication analysis. The droplet velocity was found to increase linearly with radial position from a value of zero at the center of the spreading drop, to a maximum of U_S at the spreading contact line. The kinetic energy in Equation 18 was calculated by integrating $1/2\,\rho U^2(r)$ over the entire volume of the droplet. In the absence of any energy dissipation, we can set the sum of the kinetic plus interfacial energy before impact equal to its sum following impact, $(KE_1 + SE_1) = (KE_2 + SE_2)$. In this limit, the maximum spreading diameter can be calculated by setting the velocity of the spreading drop to zero resulting in

$$\frac{D_{\max}}{D_0} = \left(\frac{\rho_w D_0 U_0^{\,2}}{3\sigma(1-\cos\theta_A)} + \frac{4}{(1-\cos\theta_A)} \right)^{1/2} = \left(\frac{We}{3(1-\cos\theta_A)} + \frac{4}{(1-\cos\theta_A)} \right)^{1/2}. \quad (20)$$

Equation 20 demonstrates that for two drops impacting a surface at the same Weber number, the maximum spreading diameter will be a function of the wettability of the surface and specifically the static advancing contact angle between the droplet and the interface. Thus, a non-wetting drop will not spread as far as a wetting drop because more energy is required to form the liquid solid interface beneath the spreading drop. The factor of $(1-\cos\theta_A)$ in Equation 20 partially explains why for the low Weber number experiments in Figure 31, droplets impacting the superhydrophobic surface did not spread as far as droplets impacting on the lubricant-infused surface or the smooth surface. However, to fully understand the difference between superhydrophobic and lubricant-infused surfaces, and to match the observed scaling of the maximum diameter with impact Weber number, we must also consider energy dissipation.[124, 125] Equation 20 results in a scaling for the maximum droplet diameter that scales with Weber number to the one half power, $D_{\max} / D_0 \sim We^{1/2}$, however, Clanet et al. [125] demonstrated that, due to dissipation upon impact, a scaling of $D_{\max} / D_0 \sim We^{1/4}$ is expected for low viscosity liquids.[125] We will return to this scaling later in the text. Until then, we will measure the energy dissipation directly from the data in Figures 2 and 3.

Using energy conservation, the total accumulated energy dissipation at any time, *DE*, can be expressed as the difference between the instantaneous kinetic and interfacial energy and directly measured from the results of the drop impact experiments.

$$DE = (KE_1 - KE_2) + (SE_1 - SE_2) = \frac{\pi\rho_w D_0^{3}(2U_0^{2} - U_s^{2})}{24} + \frac{\pi\sigma_w[4D_0^{2} - D^2(1-\cos\theta_A)]}{4}\,. \quad (21)$$

The energy dissipation in Equation 21 includes both the energy losses accumulated during droplet spreading as well as the energy dissipated during droplet impact. The calculated dissipation energy on the LIS 5, SHS, and SM surfaces is shown in Figure 33 as a function of time and Weber number. The energy dissipated during the impact was determined by extrapolating the dissipation energy to the time of impact, *t*=0, using a linear fit to the initial data in Figure 33. The energy dissipated during impact was calculated to be 2.2, 2.8, and 3.3μJ for the SM, LIS 5 and SHS surfaces, respectively, at a Weber number of *We*=52. At a Weber number of *We*=132, the energy dissipated at impact was found to increase to 7.1, 5.1, and 6.3μJ for the SM, LIS 5 and SHS surfaces, respectively. The energy dissipated at impact for the superhydrophobic surface was consistently about 20% larger than the LIS 5 over all Weber numbers tested. This suggests that the Cassie to Wenzel transition under the impacting droplet is a major source of additional energy dissipation during impact. However, it is interesting to note that even though the energy dissipation during impact was found to roughly double for the LIS and SHS surfaces as the Weber number was increased from *We*=52 to *We*=132, the total energy dissipated over the entire spreading time was found to increase by almost a factor of three. Thus, with increasing Weber number, the dissipation upon impact appears to play a diminishing role in the overall spreading dynamics.

The dissipation rate on each surface can also be studied by either taking the derivative of the data in Figure 33 with time or simply visualizing the slope of the data. The dissipation rate directly related to the viscous losses associated with the droplet spreading on a solid, air-infused or lubricant-infused surface. At lower Weber number, as seen in Figure 33a, the initial dissipation rate on the superhydrophobic surface was slightly smaller than the dissipation rate on LIS 5 and a full 40% smaller than the dissipation rate on the smooth surface. Similar observations were found for all Weber numbers tested. These observations are a direct result of the slip velocity and the associated reduction of viscous stress at the air-water and oil-water interface experienced during spreading [24, 123]. The slip length is known to decrease with increasing viscosity of the lubricant.

Due to the energy dissipated at impact and the additional viscous losses during the spreading of the droplet, the initial droplet kinetic energy is not completely transformed to the surface energy [125]. During retraction of a non-wetting droplet, these losses can result in an incomplete or partial rebound of the droplet. The viscous losses reduce the kinetic energy available to drive droplet ejection. For the case of the superhydrophobic surface, the wetting transition from Cassie to Wenzel beneath the impacting drop can also greatly enhance adhesion during the final stages of Worthington jet formation making complete rebound less likely. By measuring the adhesion area on the test surfaces during Worthington jet formation, the amount of surface driven into the Wenzel state by the high pressures at impact can be estimated. For the Weber number of *We*=52, the adhesion area was found to be $A_{C-W} = 3.3 \pm 0.1\,\mathrm{mm}^2$ or roughly one third the projected area of the impacting drop, while for *We*=132, $A_{C-W} = 3.3 \pm 0.2$ mm^2. Interestingly, no significant difference in the adhesion area was observed with increasing drop impact velocity suggesting that the area under the drop that transitions from the Cassie to the Wenzel state during impact is not strongly dependent on impact speed.

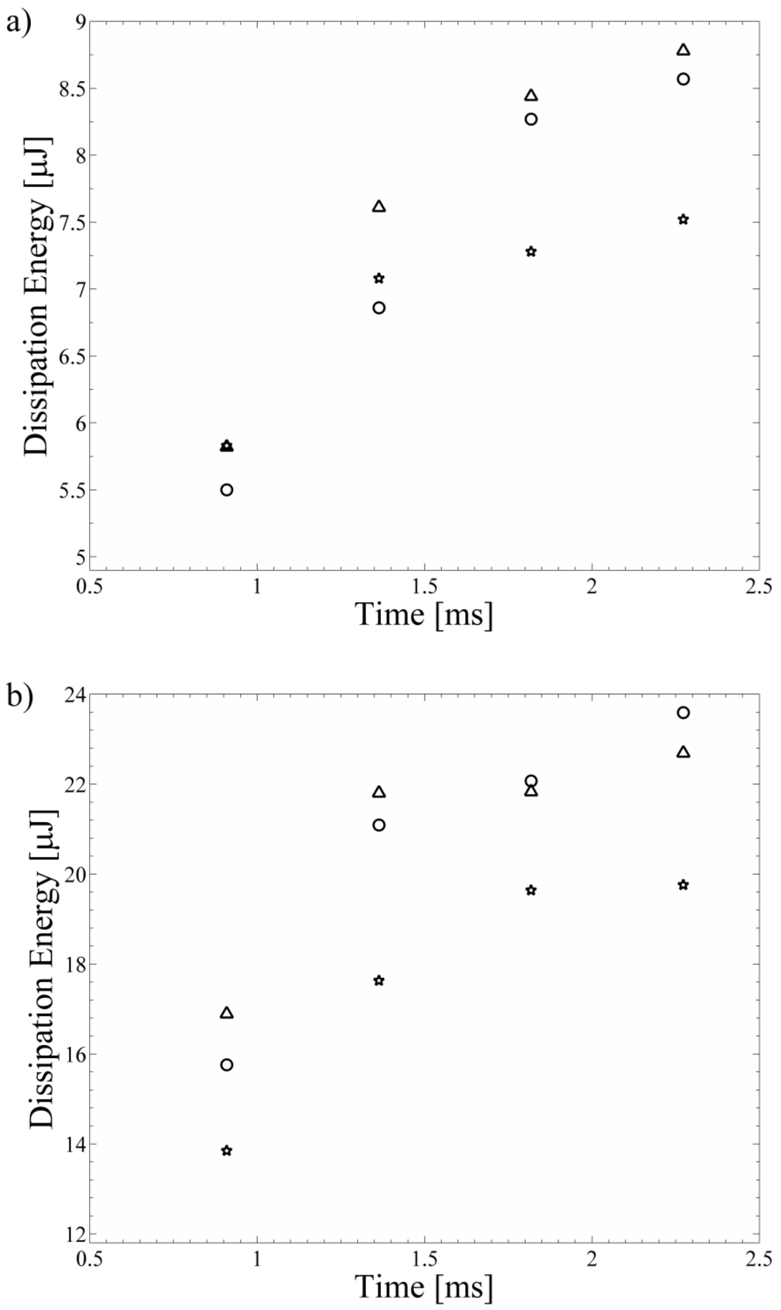

Figure 33: Energy dissipation as a function of time for droplet impacts at a Webber number of (a) *We*=52 and (b) *We*=132. The experimental data include impacts on: lubricant-infused roughened PTFE surfaces with 5cP silicone oil (circle), smooth PTFE surfaces (triangle) and air-infused superhydrophobic PTFE surfaces (star).

An additional observation from Figure 31 is that the droplets appear to pause for a short time at their maximum diameter before retracting. Here, we define the time that the droplet pauses at its maximum diameter before retracting as its time delay. To quantify the time delay on each surface, the time difference between when the drop reaches 90% of its maximum diameter during spreading and subsequently during retraction was measured and plotted in Figure 34. The first observation from Figure 34 is that the superhydrophobic surface exhibits almost no pause at all with a delay time of only 4.5ms that was found to be independent of impact Weber number. The second observation from Figure 34 is that the time delay is strongly dependent on the viscosity of the infused oil layer. The time delay decreases as the viscosity of the lubricants oil decreases, with the time delay doubling from 4.5 to 9ms from the superhydrophobic to smooth case. The maximum uncertainty of the time delay was measured to be 0.5ms on the SM and SHS surface while it was measured to be 0.4ms on the LIS surfaces. As we will show, this pause at maximum deformation is directly related to the dynamic contact angle hysteresis between the glycerin and water solution and each of the surfaces tested. Both the advancing and receding dynamic contact angles of the impacting droplets on each of the five test surfaces were measured from the captured images using ImageJ. The results are plotted as a function of time in Figure 35a. The dynamic contact angle data were also replotted against the instantaneous spreading or retraction velocity of the droplet in Figure 35b. To eliminate the effect of changing surface tension or fluid viscosity, the data in Figure 35b is recast as the dimensionless capillary number, $Ca = \mu U / \sigma$, as is the norm in dynamic contact angle studies. Note that, wherever possible, the dynamic contact angles measured at the same velocity were averaged in Figure 35b to improve the quality of the data and reduce the scatter. However, in some instances, especially for contact angles near 90°, due to the limited resolution of the images, the contact angles could not be measured with any great confidence. This is the case for the advancing contact angle on LIS 5 and as a result, only three data could be included in Figure 35. The maximum uncertainty of the dynamic contact angles for all other measurements was found to be $\pm 3.7^\circ$.

As seen in Figure 35a and 35b, the advancing contact angles on the air-infused superhydrophobic surface remain constant at $\theta_A = 145^\circ$ independent of capillary number. This observation coincides with the result of dynamic contact angles measured by the drop impact test [126] and by a force wetting technique [119]. It also indicates that the kinetic energy of the impacting droplet on the air-infused surface is transformed into surface energy with no significant viscous dissipation from the surface [125]. Conversely, the advancing contact angles on smooth and lubricant-infused surfaces decreased over time, or equivalently increased with increasing capillary number. This is the expected result for smooth surfaces where the advancing contact angle is known to increase with increasing velocity due to either hydrodynamic forces acting near the moving contact line [62, 86] or due to molecular adsorption and desorption processes at the moving contact line [62, 83]. In the case of the hydrodynamic Cox-Voinov-Tanner laws, $\theta_A{}^3 \propto Ca$ [71-73]. The advancing contact angles on the SM, LIS 14, and LIS 100 surfaces were found to follow the Cox-Voinov-Tanner laws in our experiment as shown in the inset of Figure 35b. Although it appears that the Cox-Voinov-Tanner law can predict the reaction in dynamic advancing contact angle for the low viscosity ratio lubricant-infused surfaces, the range of capillary numbers presented in Figure 35 is not sufficient as only one order of magnitude of capillary number data is spanned. As a result, the accuracy of the measurements is not sufficient for us to make a conclusive statement about the capillary number dependence of the data here. Unfortunately, this is especially true for the LIS 5 surface which appears to behave more like the superhydrophobic surface with little to no dependence of contact angle on capillary number. Although these measurements represent the first dynamic wetting measurements on lubricant infused surfaces, forced wetting experiments, like those presented in Kim et al. [119] are needed to fully understand the dynamic wetting process on lubricant-infused surfaces.

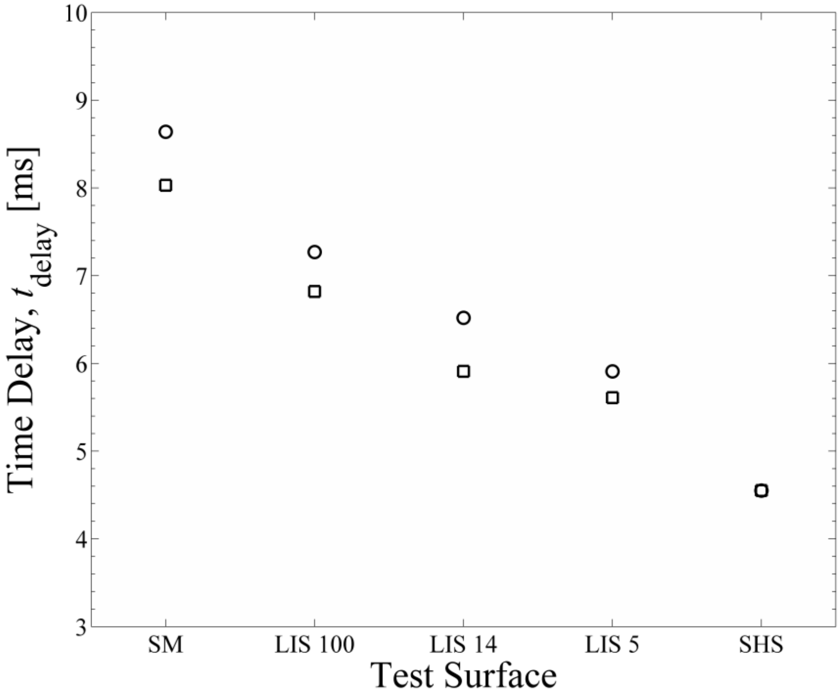

Figure 34: Time delay of impacting droplets at maximum spreading diameters. Data represents difference between the time to achieve 90% D_{max} during spreading and the time to reach 90% D_{max} during retraction of droplet from D_{max}. The data includes impacts on different test surfaces at impact Weber numbers of We=52 (circle) and We=132 (square).

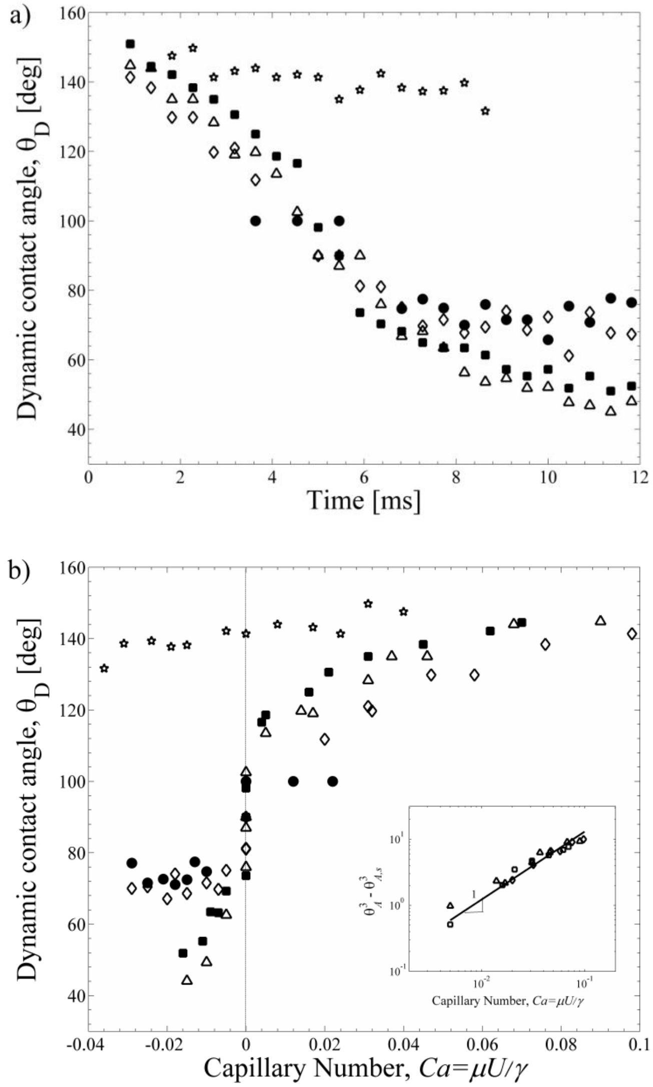

Figure 35: Dynamic contact angle measured during droplet impact on a number of different surfaces as a function of (a) time after impact and (b) the instantaneous capillary number during spreading (positive) and retraction (negative) at a Weber number of *We*=52. The experimental data include: lubricant-infused roughened PTFE surfaces with 5cP silicone oil (filled circle), 14cP silicone oil (diamond), and 100cP silicone oil (filled square) as well as smooth PTFE surface (triangle) and air-infused roughened PTFE surface (star).

It is clear from Figure 30 that the type of surface, smooth or rough, and the viscosity of the air and silicone oil infused in the surface roughness not only affects the spreading dynamics, but can also affect the retraction dynamics of the droplet. From the diameter evolution with time in Figure 31 and the velocities calculated in Figure 32, it can be observed that the retraction rate of the impacting droplets increase with decreasing viscosity of the infused silicone oil. The retraction rate of the highest viscosity silicone oil LIS 100 was found to approach the retraction rate of the droplet on the smooth PTFE surface. At these large lubricant viscosities, there is little difference between the shear stress generated between a drop spreading on a smooth surface and the lubricant-infused surface. In fact, the slip length is known to decrease linearly with increasing lubricant viscosity until it becomes too small to even measure [55]. As the viscosity of the oil is reduced to 5mPas and the slip length increased, the retraction rate on the lubricant-infused surface was found to increase about by a factor of two, approaching that of the superhydrophobic air-infused surface even though the viscosity ratios are still quite different, $\mu_{rat} = 1.2$ compared to $\mu_{rat} = 300$. However, even though the retraction rate of the least viscous silicone oil case, LIS 5, was similar to that of the superhydrophobic surface, as mentioned previously, the onset of retraction after reaching maximum spread diameter was delayed.

The delayed retraction dynamics on the LIS 5 can be best understood by inspecting the relationship between the droplet retraction velocity in Figure 32 and the dynamic receding contact angles in Figure 35. Here, we only focus on the lower Weber number case, *We*=52. On the superhydrophobic air-infused surface, the dynamic receding contact angles maintained a constant value of $\theta_R = 140^\circ$ even as the receding capillary number was increased by over an order of magnitude to *Ca*=0.04. The resulting dynamic contact angle hysteresis is very small, $\theta_H = 5^\circ$. As a result, once the droplet had reached its maximum diameter, very little time and interfacial energy was needed to deform the contact line from its dynamic advancing contact angle to its dynamic receding contact angle. On the LIS 5, however, the dynamic receding contact angle was found to remain nearly constant at $\theta_R = 73^\circ$ independent of capillary number for the velocities observed. This is significantly smaller than the static receding contact angle, $\theta_{R,s} = 98.1^\circ$. Thus, even though the lubricant-infused surfaces have little static contact angle hysteresis, the dynamic contact angle hysteresis for the LIS 5 is more than $\theta_H \geq 25^\circ$. This observation reflects the viscous energy dissipation during flow which deforms the interface of the droplet during spreading. It is the need for the droplet to transform from the dynamic advancing to receding contact angle after the maximal deformation of the droplet is reached that is responsible for the delay in the onset of droplet retraction. With increasing lubricant viscosity, an increasing in the dynamic advancing contact angle and a decrease in the dynamic receding contact angle was observed at a given capillary number. These dynamic contact angle measurements clearly show the effect that slip can have on the wetting dynamics in much the same way that has been observed for superhydrophobic surfaces [119].

Finally, a common way in the literature to study the effects of different parameters on the droplet impact dynamics is to investigate changes to the maximum spreading diameter. In our previous discussion, we focused on just two Weber numbers, *We*=52 and *We*=132. In Figure 36, a comparison of the non-dimensional maximum spreading diameter of the droplet after impact is shown for each surface tested for a wide range of Weber numbers between 20 < *We* < 200. Note that, in order to remove the effect of contact angle from maximum diameter comparison in Figure 36, Equation 20 clearly indicates that the maximum spreading diameter must be multiplied by $(1-\cos\theta_A)^{1/2}$. Normalized in this way, the droplet spreading on the superhydrophobic surfaces is found to far exceed the maximum droplet spreading diameter measured on either the smooth or the lubricant-infused surfaces for all the Weber numbers tested. This observation is consistent with the trends in the energy dissipation data in Figure 33. In all cases, the maximum spreading diameter was found to increase with increasing Weber number and, on the lubricant-infused surfaces, to increase with decreasing oil viscosity. As has been seen in the previous literature, the maximum spreading on the superhydrophobic surface was found to scale with $D_{\max}/D_0 \sim We^{1/4}$.[125] To achieve the scaling, Clanet et al. hypothesized that the shape of the drop was a direct result of the enhanced gravity the drop experienced as it impacted the substrate and decelerated. For low viscosity fluids, the shock of impact was found to result in a diameter growth that had a stronger dependence on impact velocity than high viscosity fluids $D_{\max}/D_0 \sim U_0^{1/2}$ versus $D_{\max}/D_0 \sim U_0^{1/5}$.[125] To arrive at the observed scaling, we start with the observation of Clanet et al. that a strong recirculation was observed in the spreading drop near the three phase contact line.[125] Thus, rather than assuming all the volume of the drop is dissipating energy, including fluid at the center of the drop where the shear rate is minimal, we only consider the fluid within a torus of minor radius diameter *h*/2 and major diameter $D_{\max}/2$ where the recirculation dominates and the shear rates are largest. The resulting energy dissipation scales like

$$DE \approx \Phi t_f V = \mu \left(\frac{2U_o}{h} \right)^2 \frac{D_{\max}}{U_o} \frac{\pi^2}{4} h^2 D_{\max} = \mu \pi^2 U_o D_{\max}^2 \tag{22}$$

Here Φ is the viscous dissipation function, t_f is the time of the experiment, V is the volume of the drop over which the viscous dissipation is occurring and volume conservation is used to equate final to initial drop geometries, $hD_{\max}^2 = 2/3\,D_0^3$, substituting into Equation 21 we arrive at

$$\frac{D_{\max}}{D_0} = \left(\frac{\dfrac{\rho_w D_0 U_0{}^2}{12} + \sigma_w}{\mu \pi U_o + \dfrac{\sigma_w (1 - \cos\theta_A)}{4}} \right)^{1/2} = \left(\frac{Re + \dfrac{12}{Ca}}{12\pi + \dfrac{3(1 - \cos\theta_A)}{Ca}} \right)^{1/2} \tag{23}$$

which gives the observed scaling of $D_{\max} / D_0 \sim U_0{}^{1/2}$ in the limit of moderate to large capillary numbers. This analysis can be extended to lubricant-infused surfaces.

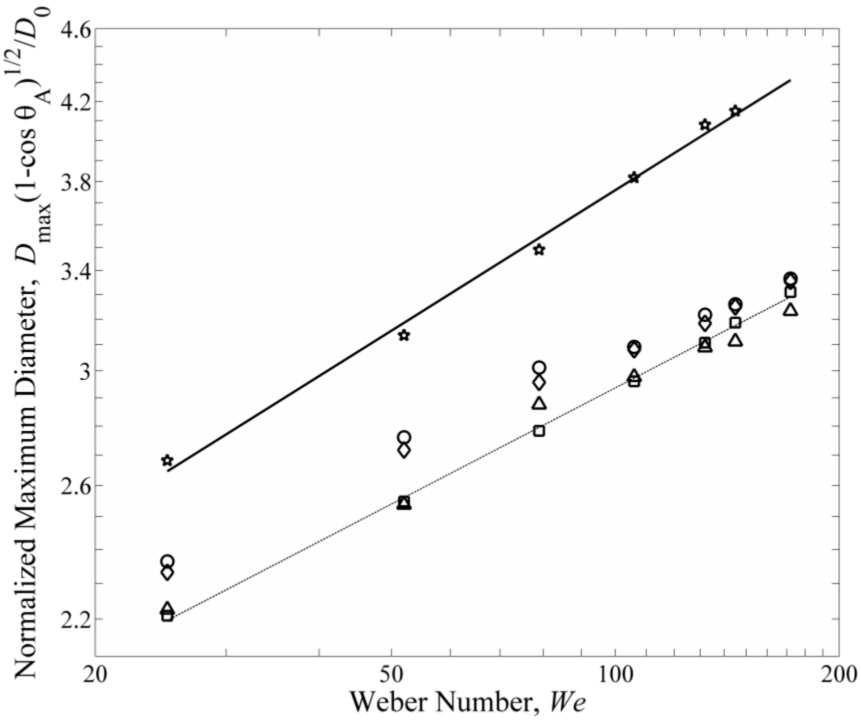

Figure 36: A log-log plot of maximum spreading diameter of the impacting aqueous glycerin drop normalized by the initial drop diameter as a function of Weber number. The experimental data include results for: lubricant-infused roughened PTFE surfaces with 5cP silicone oil (circle), 14cP silicone oil (diamond), and 100cP silicone oil (square) as well as a smooth PTFE surface (triangle) and a superhydrophobic air-infused roughened PTFE surface (star). The solid line of the air-infused case (star) indicates a scaling of $D_{max}/D_0 \sim We^{1/4}$ from theory while the dotted line of LIS 100 case (square) indicates a scaling of $D_{max}/D_0 \sim We^{1/5}$.

For LIS, the viscous energy dissipation to account for the oil layer on the surface can be estimated as $DE \approx \mu_w \pi^2 \left(U_0 - U_I\right) D^2{}_{\max}$. Here, U_I is interfacial velocity at the oil-water interface. The interfacial velocity can be calculated to be $U_I = \left(t\mu_w / \left(h\mu_0 + t\mu_w\right)\right) U_0$ by matching the shear stress in the oil phase to the shear stress in the water phase at the oil-water interface. Here *t* is the oil film thickness. By equating the initial kinetic and surface energy to the final surface and dissipation energy, $KE_1 + SE_1 = SE_2 + DE$, it can be shown that the maximum spreading diameter depends on droplet geometry, viscosity ratio, Reynolds number, and capillary number

$$\frac{D_{\max}}{D_0} = \left(\frac{Re + \dfrac{12}{Ca}}{12\pi\left[1 + \left(\dfrac{t}{h}\right)\left(\dfrac{\mu_w}{\mu_o}\right)\right]^{-1} + \dfrac{3(1-\cos\theta_A)}{Ca}} \right)^{1/2} \tag{24}$$

Note that we obtain the same scaling with velocity or Weber number found by Clanet et al. [57, 125], but with an expression that is modified by the viscosity ratio. Although this does not exactly match the experimentally observed scaling of $We^{1/5}$ or $U^{2/5}$, it does allow us to better understand the dependence of maximum spreading diameter on the infused oil viscosity. Unfortunately, at this moment, it is unclear why the maximum spreading diameter on the lubricant-infused surfaces scales differently. In order to fit the scaling analysis in Equation 24 to the data in Figure 36, the oil film thickness was assumed to be similar order of RMS surface roughness, *t* =14μm [33], and the thickness of the maximum spreading droplet, *h,* is calculated from the captured image. With this assumption, the pre-factor becomes approximately *t*/*h* ~ 0.12. To test the scaling, the data in Figure 36 was replotted as $[D_{\max} / D_0] / \left[1 + 0.12\mu_{ratio}\right]^{0.5}$ representing the limit when capillary number is large and presented in Figure 37. All the lubricant-infused surface data were found to collapse to within 5% onto a master curve. This scaling also explains why previous studies where the viscosity ratio was much less than one, $\mu_{ratio} \ll 1$, observed little to no change in the maximum spreading diameter of the impacting droplet [57, 122]. For those experiments, $\left(t / h\right)\left(\mu_w / \mu_o\right) \ll 1$, and, as a result, the effect of the infused oil layer can be ignored in Equation 24.

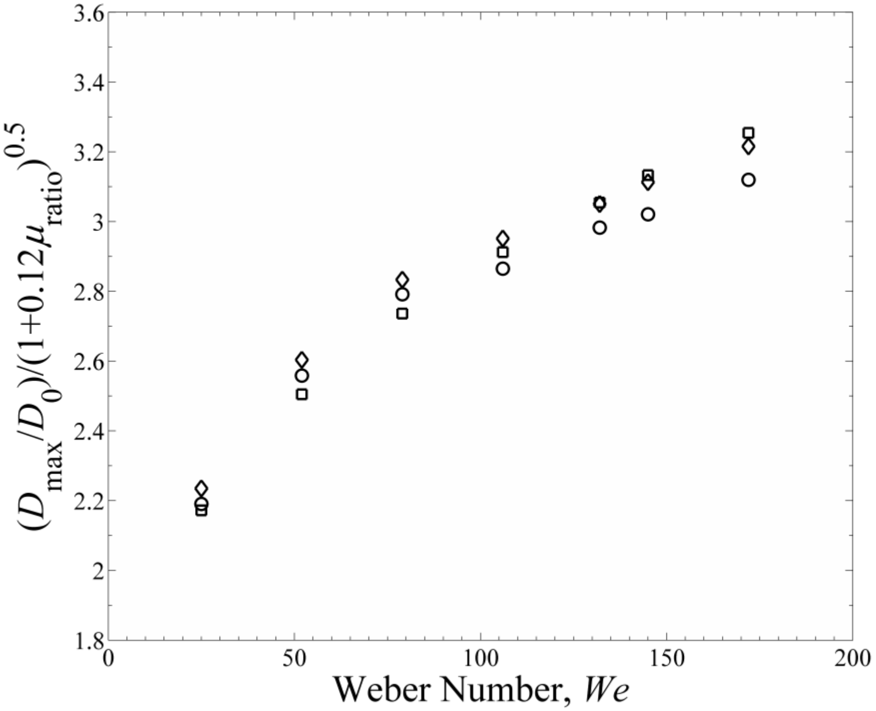

Figure 37: A scaling analysis for the maximum diameter of the aqueous glycerin drop normalized by the initial drop diameter as a function of Weber number. The experimental data include sanded lubricant-infused PTFE surfaces with 5cP silicone oil (circle), 14cP silicone oil (diamond), and 100cP silicone oil (square). All the data collapse with the selection of *t*/*h*=0.12.

6.4 Conclusions

The spreading and retraction dynamics on lubricant-infused PTFE surfaces were investigated through high speed imaging. The lubricant-infused PTFE surfaces were prepared by sanding the smooth PTFE surface with 240-grit sandpapers and infusing the silicone oils into the micro-structures of the surface. The viscosity of infused silicone oil was varied to investigate the effect of the viscosity ratio between the impinging droplet and the infused lubricant layer. The evolution of the droplet diameter, droplet spreading and retraction velocities and the dynamic contact angles were measured as a function of time after impact.

The maximum spreading diameter of the droplet on lubricant-infused surfaces was found to increase with decreasing viscosity of the infused silicone oil. Furthermore, the droplet spreading velocities became larger as the oil viscosity was reduced. These increases in the maximum droplet diameter and the droplet spreading velocities resulted from the presence of a finite slip length and the reduction in shear stress at the oil-water interface on lubricant-infused surfaces. The results for the largest oil viscosity tested were indistinguishable from experiments performed on a smooth PTFE surface, showing the importance of increasing the viscosity ratio between the droplet and the infused oil phase to a value as large as possible. These differences with oil viscosity were not observed in previous studies because the oil viscosity was large and the resulting viscosity ratio was much less one, $\mu_w / \mu_o \ll 1$, in all cases [57, 122]. This point is reinforced by a scaling analysis which was able to collapse the maximum diameter data onto a master curve when it was replotted as $\frac{D_{\max}}{D_0} = \left[1 + \left(\frac{t}{h}\right)\left(\frac{\mu_w}{\mu_o}\right)\right]^{1/2} Oh^{-1/2} We^{1/4}$.

Interestingly, significant and perhaps non-intuitive differences were observed in the maximum droplet diameter between the least viscous silicone oil case, LIS 5, and the air-infused superhydrophobic surface, SHS. At the lower Weber numbers tested, the maximum droplet diameter on the LIS 5 was found to be larger than that of the SHS even though the viscosity of the oil infused into the surface features of the LIS 5 was 250 times larger than the air infused into the surface features of the SHS case. This was shown to be due, in part, to the larger advancing contact angle on the superhydrophobic surface. However, it was also shown that a significant amount of energy was dissipated during the impact of a droplet on the SHS due to a wetting transition from the superhydrophobic Cassie state to the fully-wetted Wenzel state induced by the large pressures produced beneath the drop. The presence of the incompressible oil in the lubricant-infused surface was found to mitigate these losses while still producing slip at the oil-water interface thus resulting in a larger fraction of the initial kinetic energy available to deform the droplet to a greater maximum droplet diameter. As the Weber number was increased, the energy dissipation at impact was found to grow more slowly with Weber number than the energy dissipation during spreading. As a result, at We=100, the maximum spreading droplet diameter on the superhydrophobic surface was found to surpass the lubricant-infused surfaces.

The retraction rate of the droplet on lubricant-infused surfaces was also found to increase with decreasing lubricant viscosity. The retraction rate on the LIS 5 approached that of the SHS, however, a significant difference in the time between reaching maximum diameter and beginning of the retraction was observed between the LIS 5 and the SHS. Once the droplet reached the maximum deformation, the motion of the droplet was observed to pause as the contact angles decreased from the dynamic advancing to the dynamic receding contact angle. Because the dynamic contact angle hysteresis on the SHS was extremely low, $\theta_H = 5^\circ$, the observed delay time was quite small, t_{delay} < 5ms. However, even though the static contact angle hysteresis on the lubricant-infused surfaces were all similar to the SHS and less than $\theta_H < 4^\circ$, the contact angle hysteresis observed during spreading were all found to be much larger than the static case, $\theta_H > 25^\circ$. As a result, an increase in contact angle hysteresis and delay time was observed with increasing oil viscosity. Variation in contact angle with spreading velocity is known to occur due to viscous losses near the moving contact line.

Using the data from the droplet impact experiments, the first ever measurements of the dynamic advancing and dynamic receding contact angle were made for liquids spreading on lubricant-infused surfaces. The advancing contact angles on the smooth surface and both the LIS 14 and LIS 100 surfaces were found to increase with increasing capillary number. Furthermore, the advancing contact angles on the surfaces were all found to follow the expected Cox-Voinov-Tanner laws, $\theta_A^3 \propto Ca$. However, the onset of growth in the contact angle was delayed as the viscosity of the lubricant was decreased. The dynamic advancing contact angle on the LIS 5 surface did not follow the expected scaling laws, but instead showed little to no growth in the contact angle with increasing capillary number. This behavior was similar to the observations for droplet spreading on superhydrophobic surfaces and is known to be a result of the large slip length and reduced shear stress near the moving contact line [119]. Similar observations were made for the dynamic receding contact angle which was found to decrease with an increasingly negative capillary number. Note, however, that the receding angle appeared to be more sensitive to lubricant viscosity than the advancing angle. These differences are the driving force behind the increase in observed dynamic contact angle hysteresis with increasing oil viscosity. Although these measurements are an important beginning, forced wetting experiments over a wider range of capillary numbers are needed to fully understand the dynamic wetting process on lubricant-infused surfaces.

CHAPTER 7

CONCLUSIONS AND CONTRIBUTIONS

The preceding chapters have discussed the dynamic wetting and drag reduction on the air-infused and liquid-infused superhydrophobic surfaces. The first dynamic contact angle measurements on the superhydrophobic surfaces were conducted by using a force wetting technique. The presence of slip on the superhydrophobic surfaces made a significant impact on the dynamic contact angle measurements. The advancing contact angles were found to be constant with increasing capillary number up to $Ca = 0.2$. However, the receding contact angles were decreased with increasing capillary number. The weaker dependence of the dynamic receding contact angles on contact line speed, ${\theta_{R,s}}^3 - {\theta_R}^3 \propto Ca^{1/3}$, are still not understood physically. This result is in contrast to the predictions of the hydrodynamic model which predicts ${\theta_D}^3 - {\theta_{D,s}}^3 \propto Ca$ and molecular interaction models which predict ${\theta_D}^2 - {\theta_{D,s}}^2 \propto Ca$. The results can, however, be fit by Petrov and Petrov's combined hydrodynamic-molecular model with the appropriate choice of parameters. These results were published in *Physics of Fluids* [119]. With the same measurement technique, dynamic contact angles of the viscoelastic fluids were also measured as a function of capillary number. Both dynamic advancing and receding contact angles were found to scale like ${\theta_D}^3 - {\theta_{D,s}}^3 \propto Ca^2$ when Weissenberg number was greater than one, which is significantly deviated from the scaling for the Newtonian solution. These results were understood through the development of a new model which takes into account the role of shear thinning and elasticity. The results were published in

Journal of Non-Newtonian Fluid Mechanics [127]. In the next chapter, we have discussed the role of the interface shape on laminar drag reduction. Both the geometry of the air-water interface and the slip along the air-water interface was found to affect the drag reducing properties of the superhydrophobic surfaces. Slip was present at all interface shapes. The increase or decrease in the flow cross-sectional area by the geometry of the interface played an important role in the drag reduction with increasing interface intrusion into the flow. It increased drag until the beneficial effects of slip were eliminated. This result is now prepared for publication [128].

Research into the liquid-infused surfaces clearly demonstrated that the reduction in shear stress at the oil-water interface was attained by increasing the viscosity ratio. In the microchannel experiments, the drag reduction and slip length were found to increase with increasing viscosity ratio between the water and oil phase. In addition, we demonstrated that the depletion of the lubricant with flow was a serious problem for lubricant-infused surfaces. Randomly rough superhydrophobic surfaces were found to delay depletion due to the added pathways for re-circulation of the lubricant in the three-dimensional patterned surface and the existence of deep reservoir pockets distributed across the surface. These results were published in *Experiments in Fluid* [123]. Finally, in the study of the drop impact dynamics on the liquid-infused surfaces, the increase in the viscosity ratio was shown to increase the spreading rate of the droplet following impact, the maximum spreading diameter, the retraction velocity after the droplet reached its maximum diameter, and reduced the energy dissipation rate during the entire process. Significant differences were also observed between liquid-infused superhydrophobic surfaces and air-infused superhydrophobic surfaces during droplet impact. This study is now in the process of revision in *Langmuir* [129].

BIBLIOGRAPHY

[1] T. Young, An Essay on the Cohesion of Fluids, Phil. Trans. Roy. Soc. London, 95 (1805) 65-87.

[2] P.G. de Gennes, F. Brochard-Wyart, D. Quéré, Capillarity and wetting phenomena: drops, bubbles, pearls, waves, Springer, New York, 2004.

[3] D. Quere, Wetting and roughness, Annu. Rev. Mater. Res., 38 (2008) 71-99.

[4] S. EG, Z. WA, Upper limits to the contact angles of liquids on solids. In Contact Angle, Wettability and Adhesion: Advances in Chemistry Series, Am. Chem. Soc., 43 (1964) 145-157.

[5] R.N. Wenzel, Resistance of solid surfaces to wetting by water, Ind. Eng. Chem., 28 (1936) 988-994.

[6] A.B.D. Cassie, S. Baxter, Wettability of porous surfaces, Trans. Faraday Soc., 40 (1944) 546-551.

[7] A. Lafuma, D. Quere, Superhydrophobic states, Nature Materials, 2 (2003) 457-460.

[8] W. Barthlott, C. Neinhuis, Purity of the sacred lotus, or escape from contamination in biological surfaces, Planta, 202 (1997) 1-8.

[9] E.A. Hebets, R.F. Chapman, Surviving the flood: plastron respiration in the non-tracheatearthropod Phrynus marginemaculatus (Amblypygi: Arachnida), J. Insect Physiology, 46 (2000) 13-19.

[10] D.L. Hu, B. Chan, J.W.M. Bush, The hydrodynamics of water strider locomotion, Nature, 424 (2003) 663-666.

[11] T. Nørgaard, M. Dacke, Fog-basking behaviour and water collection efficiency in Namib Desert Darkling beetles, Frontiers in Zoology, 7 (2010) 23.

[12] N.J. Shirtcliffe, G. McHale, M.I. Newton, C.C. Perry, F.B. Pyatt, Plastron properties of a superhydrophobic surface, Appl. Phys. Lett., 89 (2006) 104106.

[13] N.J. Shirtcliffe, F.B. Pyatt, M.I. Newton, G. McHale, A lichen protected by a super-hydrophobic and breathable structure, J. Plant Physiology, 163 (2006) 1193-1197.

[14] Y. Zheng, X. Gao, L. Jiang, Directional adhesion of superhydrophobic butterfly wings, Soft Matter, 3 (2007) 178-182.

[15] J.P. Rothstein, Slip on Superhydrophobic Surfaces, Annu. Rev. Fluid Mech., 42 (2010) 89-109.

[16] Y. Xue, P. Lv, H. Lin, H. Duan, Underwater Superhydrophobicity: Stability, Design and Regulation, and Applications, Applied Mechanics Reviews, 68 (2016) 030803-030801.

[17] R. Furstner, W. Barthlott, Wetting and Self-Cleaning Properties of Artificial Superhydrophobic Surfaces, Langmuir, 21 (2005) 956-961.

[18] J. Ou, J.B. Perot, J.P. Rothstein, Laminar drag reduction in microchannels using ultrahydrophobic surfaces, Phys. Fluids, 16 (2004) 4635-4660.

[19] J. Ou, J.P. Rothstein, Direct velocity measurements of the flow past drag-reducing ultrahydrophobic surfaces, Phys. Fluids, 17 (2005) 103606.

[20] R. Daniello, N.E. Waterhouse, J.P. Rothstein, Turbulent drag reduction using superhydrophobic surfaces, Phys. Fluids, 21 (2009) 085103.

[21] S. Srinivasan, W. Choi, K.-C. Park, S.S. Chhatre, R.E. Cohen, G.H. McKinley, Drag reduction for viscous laminar flow on spray-coated non-wetting surfaces, Soft Matter, 9 (2013) 5691–5702.

[22] K. Watanabe, Y. Udagawa, H. Udagawa, Drag reduction of Newtonian fluid in a circular pipe with highly water-repellent wall, J. Fluid Mech., 381 (1999) 225-238.

[23] R. Truesdell, A. Mammoli, P. Vorobieff, P. van Swol, C.J. Brinker, Drag reduction on a patterened superhydrophobic surface, Phys. Rev. Lett., 97 (2006) 044504.

[24] D. Song, R. Daniello, J.P. Rothstein, Drag reduction using superhydrophobic sanded Teflon surfaces, Experiments in Fluids, 55 (2014) 1783.

[25] G. McHale, N.J. Shirtcliffe, C.R. Evans, M.I. Newton, Terminal velocity and drag reduction measurements on superhydrophobic spheres, App. Phys. Lett., 94 (2009) 064104.

[26] J. Genzer, K. Efimenko, Recent developments in superhydrophobic surfaces and their relevance to marine fouling: a review, Biofouling: The Journal of Bioadhesion and Biofilm Research, 22 (2006).

[27] H. Zhang, R. Lamb, J. Lewis, Engineering nanoscale roughness on hydrophobic surface-preliminary assessment of fouling behavior, Science and Technology of Advanced Materials, 6 (2005) 236-239.

[28] S. Farhadi, M. Farzaneh, S.A. Kulinich, Anti-icing performance of superhydrophobic surfaces, Appl. Surf. Sci., 257 (2011) 6264-6269.

[29] L. Cao, A.K. Jones, V.K. Sikka, J. Wu, D. Gao, Anti-Icing Superhydrophobic Coatings, Langmuir, 25 (2009) 12444-12448.

[30] Y.Y. Yan, N. Gao, W. Barthlott, Mimicking natural superhydrophobic surfaces and grasping the wetting process: A review on recent progress in preparing superhydrophobic surfaces, Advances in Colloid and Interface Science, 169 (2011) 80-105.

[31] D. Oner, T.J. McCarthy, Ultrahydrophobic surfaces: Effects of topography length scales on wettability, Langmuir, 16 (2000) 7777-7782.

[32] L. Gao, T.J. McCarthy, A perfectly hydrophobic surface (theta(A)/theta(R)=180 degrees/180 degrees), Journal of the American Chemical Society, 128 (2006) 9052-9053.

[33] M. Nilsson, R. Daniello, J.P. Rothstein, A novel and inexpensive technique for creating superhydrophobic surfaces using Teflon and sandpaper, J. Phys. D: Appl. Phys., 43 (2010) 045301.

[34] X.-M. Li, D. Reinhoudt, M. Crego-Calama, What do we need for a superhydrophobic surface? A review on the recent progress in the preparation of superhydrophobic surfaces, Chemical Society Reviews, 36 (2007) 1350-1368.

[35] J. Feng, M. Tuominen, J.P. Rothstein, Hierarchical superhydrophobic surfaces fabricated by dual-scale electron-beam lithography with well-ordered secondary nano-structures, Adv. Func. Mat., 21 (2011) 3715-3722.

[36] D. Jucius, V. Grigaliunas, M. Mikolajunas, P. Narmontas, Hot embossing of PTFE: Towards superhydrophobic surfaces, Applied Surface Science, 257 (2010) 2353-2360.

[37] T. Liu, C.-J. Kim, Turning a surface superrepellent even to completely wetting liquids, Science, 346 (2014) 1096-1100.

[38] S. Srinivasan, J.A. Kleingartner, J.B. Gilbert, R.E. Cohen, A.J.B. Milne, G.H. McKinley, Sustainable drag reduction in turbulent Talyor-Couette flows by depositing sprayable superhydrophobic surfaces, Physical review letters, 114 (2015) 014501.

[39] S. Moghtadernejad, M. Tembely, M. Jadidi, N. Esmail, A. Dolatabadi, Shear driven droplet shedding and coalescence on a superhydrophobic surface, Physics of Fluids, 27 (2015) 032106.

[40] G. Whitesides, A.D. Stroock, Flexible methods for microfluidics, Phys. Today, 54 (2001) 42-48.

[41] N. Kim, H. Kim, H. Park, An experimental study on the effects of rough hydrophobic surfaces on the flow around a circular cylinder, Physics of Fluids, 27 (2015) 085113.

[42] J.C. Maxwell, On Stresses in Rarified Gases Arising from Inequalities of Temperature, Phil. Trans. Roy. Soc. London, 170 (1879) 231-256.

[43] D.M. Tolstoi, Molecular theory for slippage of liquids over solid surfaces (in Russian), Doklady Akad. Nauk SSSR, 85 (1952) 1089–1092.

[44] P. Tsai, A.M. Peters, C. Pirat, M. Wessling, R.G.H. Lammertink, D. Lohse, Quantifying effective slip length over micropatterned hydrophobic surfaces, Phys. Fluids, 21 (2009) 112002.

[45] E. Karatay, A.S. Haase, C.W. Visser, C. Sun, D. Lohse, P.A. Tsai, R.G.H. Lammertink, Control of slippage with tunable bubble mattresses, PNAS, 110 (2013) 8422-8426.

[46] S. Gogte, P. Vorobieff, R. Truesdell, A. Mammoli, F. van Swol, P. Shah, C.J. Brinker, Effective slip on textured superhydrophobic surfaces, Phys. Fluids, 17 (2005) 051701.

[47] M. Srinivasarao, G.C. Berry, Rheo-optical studies on aligned nematic solutions of a rodlike polymer, J Rheol, 35 (1991) 379-397.

[48] C.H. Choi, C.J. Kim, Large slip of aqueous liquid flow over a nanoengineered superhydrophobic surface, Phys. Rev. Lett., 96 (2006) 066001.

[49] T.-S. Wong, S.H. Kang, S.K.Y. Tang, E.J. Smythe, B.D. Hatton, A. Grinthal, J. Aizenberg, Bioinspired Self-repairing slippery surfaces with pressure-stable omniphoicity, Nature, 477 (2011) 443-447.

[50] L. Bocquet, E. Lauga, A smooth future?, Nature Materials 10 (2013) 334–337.

[51] A.K. Epstein, T.-S. Wong, R.A. Belisle, E.M. Boggs, J. Aizenberg, Liquid-infused structured surfaces with exceptional anti-biofouling performance, Proc. Natl. Acad. Sci., 109 (2012) 13182-13187.

[52] P. Kim, T.-S. Wong, J. Alvarenga, M.J. Kreder, W.E. Adorno-Martinez, J. Aizenberg, Liquid-Infused Nanostructured Surfaces with Extreme Anti-Ice and Anti-Frost Performance, ACS Nano, 6 (2012) 6569 -6577

[53] A. Lafuma, D. Quere, Slippery pre-suffused surfaces, Europhysics Letters, 96 (2011) 56001.

[54] J.D. Smith, R. Dhiman, S. Anand, E. Reza-Garduno, R.E. Cohen, G.H. McKinley, K.K. Varanasi, Droplet mobility on lubricant-impregnated surfaces, Soft Matter, 9 (2013) 1772-1780.

[55] B.R. Solomon, K.S. Khalil, K.K. Varanasi, Drag Reduction using Lubricant-Impregnated Surfaces in Viscous Laminar Flow, Langmuir, 30 (2014) 10970-10976.

[56] S.B. Subramanyam, K. Rykaczewski, K.K. Varanasi, Ice Adhesion on Lubricant-Impregnated Textured Surfaces, Langmuir, 29 (2013) 13414-13418.

[57] C. Lee, H. Kim, Y. Nam, Drop Impact Dynamics on Oil-Infused Nanostructured Surfaces, Langmuir, 30 (2014) 8400-8407.

[58] M. Reyssat, A. Pepin, F. Marty, Y. Chen, D. Quere, Bouncing transitions on microtextured materials, Europhys. Lett., 74 (2006) 306-312.

[59] D. Richard, D. Quere, Bouncing water drops, Europhys. Lett., 50 (2000) 769-775.

[60] M. Nilsson, J.P. Rothstein, The effect of contact angle hysteresis on droplet coalescence and mixing, J. Colloid and Interface Sci., 363 (2011) 646-654.

[61] M. Nilsson, J.P. Rothstein, Using sharp transition in contact angle hysteresis to move and deflect droplets on a superhydrophobic surface, Phys. Fluids, 24 (2012) 062001.

[62] J.C. Berg, Wettability, Marcel Dekker, Inc., New York, 1993.

[63] R. Hoffman, A study of the advancing interface. I. Interface shape is liquid-gas systems, J. Colloid Interface Sci., 50 (1975) 228-241.

[64] E.B. Dussan, On the spreading of liquids on solid surfaces: static and dynamic contact lines, Annu. Rev. Fluid Mech., 11 (1979) 371-400.

[65] R.E. Johnson, R.H. Dettre, D.A. Brandeth, Dynamic Contact Angles and Contact Angle Hysteresis, J. Colloid and Interface Sci., 62 (1977) 205-212.

[66] G. Strom, M. Fredriksson, P. Stenius, B. Radoev, Kinetics of Steady-State Wetting, J. Colloid and Interface Sci., 134 (1990) 107-116.

[67] T.D. Blake, K.J. Ruschak, A maximum speed of wetting, Nature, 282 (1979) 489-491.

[68] R. Burley, R.P.S. Jolly, Entrainment of air into liquids by a high speed continous solid surface, Chemical Engineering Science, 39 (1984) 1357-1372.

[69] J.G. Petrov, J. Ralston, M. Schneemilch, R.A. Hayes, Dynamics of Partial Wetting and Dewetting in Well-Defined Systems, J. Phys. Chem., 107 (2003) 1634-1645.

[70] C. Huh, L.E. Scriven, Hydrodynamic model of steady movement of a solid/liquid/fluid contact line, J. Colloid and Interface Sci., 35 (1971) 85-101.

[71] O.V. Voinov, Hydrodynamics of wetting, Fluid Dynamics, 11 (1976) 714-721.

[72] L.H. Tanner, The spreading of silicone oil drop on horizontal surfaces, J. Phys. D: Appl. Phys., 12 (1979) 1473-1484.

[73] R.G. Cox, The dynamics of the spreading of liquids on a solid surface. Part1. Viscous flow, Journal of Fluid Mechanics, 168 (1986) 169-194.

[74] J.H. Snoeijer, B. Andreotti, Moving Contact Lines: Scales, Regimes, and Dynamical Transitions, Annu. Rev. Fluid Mech., 45 (2013) 269-292.

[75] J. Eggers, H.A. Stone, Charateristic lengths at moving contact lines for a perfectly wetting fluid: The influence of speed on the dynamic contact angle, J. Fluid Mech., 505 (2004).

[76] L.M. Hocking, Rival contact-angle models and the spreading of drops, J. Fluid Mech., 239 (1992) 671-681.

[77] J. Eggers, Existence of receding and advancing contact linew, Phys. Fluids, 17 (2005) 082106.

[78] C.G. Ngan, E.B. Dussan V., On the nature of the dynamic contact angle: an experimental study, J. Fluid Mech., 118 (1982) 27-40.

[79] J.E. Seebergh, J.C. Berg, Dynamic wetting in the low capillary number regime, Chemical Engineering Science, 47 (1992) 4455-4464.

[80] J.H. Snoeijer, Free-surface flows with large slopes: Beyond lubrication theory, Phys. Fluids, 18 (2006) 021701.

[81] S.F. Kistler, Hydrodynamics of wetting, in: J.C. Berg (Ed.) Wettability, Marcel Dekker, New York,, 1993, pp. 311.

[82] M. Bracke, F.D. Voeght, P. Joos, The kinetics of wetting: The dynamic contact angle, Prog. Colloid Polym. Sci, 79 (1989).

[83] T.D. Blake, J.M. Haynes, Kinetics of liquid/liquid displacement, J. Colloid and Interface Sci., 30 (1969) 421-423.

[84] M. Schneemilch, R.A. Hayes, J.G. Petrov, J. Ralston, Dynamic wetting and dewetting of a low-energy surface by pure liquids, Langmuir, 14 (1998) 7047-7051.

[85] T.D. Blake, Y.D. Shikhmurzaev, Dynamic wetting by liquids of different viscosity, J. Colloid and Interface Sci., 253 (2002) 196-202.

[86] T.D. Blake, The physics of moving wetting lines, J. Colloid and Interface Sci., 299 (2006) 1-13.

[87] P. Muralidhar, N. Ferrer, R. Daniello, J.P. Rothstein, Influence of Slip on the Flow Past Superhydrophobic Circular Cylinders, J. Fluid Mech., 680 (2011) 459-476.

[88] P. Petrov, I. Petrov, A combined molecular-hydrodynamic approach to wetting kinetics, Langmuir, 8 (1992) 1762-1767.

[89] J.W. Krumpfer, T.J. McCarthy, Dip-coating crystallization on a superhydrophobic surfaces: A Million mounted crystals in a 1 cm2 array, J. Am. Chem. Soc., 133 (2011) 5764.

[90] P.G. de Gennes, Wetting: Statics and Dynamics, Rev. Mod. Phys., 57 (1985) 827-863.

[91] Y. Wei, E. Rame, L.M. Walker, S. Garoff, Dynamic wetting with viscous Newtonian and non-Newtonian fluids, J. Phys. Condens. Mat., 21 (2009) 464126.

[92] Y. Wei, G.K. Seevaratnam, S. Garoff, E. Rame, L.M. Walker, Dynamic wetting of Boger Fluids, J. Colloid and Interface Sci., 313 (2009) 274-280.

[93] W. Rose, R.W. Heins, Moving interfaces and contact angle rate-dependency, Journal of Colloid and Interface Science, 17 (1962) 39-48.

[94] B. Legait, P. Sourieau, Effect of geometry on advancing contact angles in fine capillaries, J. Colloid and Interface Sci., 107 (1985) 14-20.

[95] M.W. Johnson, D. Segalman, Model for viscoelastic fluid behavior which allows non-affine deformation, J. Non-Newt. Fluid Mech., 2 (1977) 255-270.

[96] G.K. Seevaratnam, Y. Suo, E. Ramé, L.M. Walker, S. Garoff, Dynamic wetting of shear thinning fluids, Phys. Fluids, 19 (2007) 012103.

[97] A. Carre, F. Eustache, Spreading kinetics of shear-thinning fluids in wetting and dewetting modes, Langmuir, 16 (2000) 2936-2941.

[98] Z.P. Liang, X.-D. Wang, D.-J. Lee, X.-F. Peng, A. Su, Spreading dynamics of power-law fluid droplets, Journal of Physics: Condensed Matter, 21 (2009) 464117.

[99] A.K. Sankaran, J.P. Rothstein, The Effect of Viscoelasticity on Liquid Transfer during Gravure Printing, J. Non-Newtonian Fluid Mech., 175-176 (2012) 64-75.

[100] S. Khandavalli, J.P. Rothstein, Extensional rheology of shear-thickening fumed silica nanoparticles dispersed in an aqueous polyethylene oxide solution, J. Rheol., 58 (2014) 411-431.

[101] C.M. White, M.G. Mungal, Mechanics and Prediction of Turbulent Drag Reduction with Polymer Additives, Annu. Rev. Fluid Mech., 40 (2008) 235-256.

[102] B.R. Elbing, E.S. Winkel, K.A. Lay, S.L. Ceccio, D.R. Dowling, M. Perlin, Bubble-induced skin-friction drag reduction and the abrupt transition to air-layer drag reduction, J. Fluid Mech., 612 (2008) 201-236.

[103] W.C. Sanders, E.S. Winkel, D.R. Dowling, M. Perlin, S.L. Ceccio, Bubble friction drag reduction in a high-reynolds-number flat-plate turbulent boundary layer, J. Fluid Mech., 552 (2006) 353-380.

[104] A. Steinberger, C. Cottin-Bizonne, P. Kleimann, E. Charlaix, High friction on a bubble mattress, Nature Mater., 6 (2007) 665-668.

[105] A.M.J. Davis, E. Lauga, Geometric transition in friction for flow over a bubble mattress, Phys. Fluids, 21 (2009) 011701.

[106] M. Sbragaglia, A. Prosperetti, A note on the effective slip properties for microchannel flows with ultrahydrophobic surfaces, Phys. Fluids, 19 (2007) 043603

[107] S. Richardson, On the no-slip boundary condition, J. Fluid Mech., 59 (1973) 707-719.

[108] M.K. Mulligan, J.P. Rothstein, The Effect of Confinement-Induced Shear on Drop Deformation and Breakup in Microfluidic Extensional Flows, Physics of Fluids, 23 (2011) 022004.

[109] R. Daniello, P. Muralidhar, N. Carron, M. Greene, J.P. Rothstein, Influence of slip on vortex induced motion of a superhydrophobic cylinder, J. Fluid Struct., 42 (2013) 358-368.

[110] E. Lauga, H.A. Stone, Effective slip in pressure-driven Stokes flow, Journal of Fluid Mechanics, 489 (2003) 55-77.

[111] I. Jacobi, J.S. Wexler, M.A. Samaha, J.K. Shang, B.J. Rosenberg, M. Hultmark, H.A. Stone, Stratified thin-film flow in a rheometer, Physics of Fluids, 27 (2015) 052102.

[112] I. Jacobi, J.S. Wexler, H.A. Stone, Overflow cascades in liquid-infused substrates, Physics of Fluids, 27 (2015) 082101.

[113] J.S. Wexler, A. Grosskopf, M. Chow, Y. Fan, I. Jacobi, H.A. Stone, Robust liquid-infused surfaces through patterned wettability, Soft Matter, 11 (2015) 5023-5029.

[114] J.S. Wexler, I. Jacobi, H.A. Stone, Shear-Driven Failure of Liquid-Infused Surfaces, Physical Review Letters, 114 (2015).

[115] I.N. Milosevic, E.K. Longmire, Pinch-off modes and satellite formation in liquid/liquid jet systems, International Journal of Multiphase Flow, 28 (2002) 1853-1869.

[116] C. Ybert, C. Barentin, C. Cottin-Bizonne, P. Joseph, L. Bocquet, Achieving large slip with superhydrophobic surfaces: Scaling laws for generic geometries, Physics of Fluids, 19 (2007) 123601.

[117] X. Gao, L. Jiang, Water-repellent legs of water striders, Nature, 432 (2004) 36.

[118] J.W.M. Bush, D.L. Hu, M. Prakash, The Integument of Water-walking Arthropods: Form and Function, Adv. Insect Physiology, 34 (2008) 117-192.

[119] J.-H. Kim, H.P. Kavehpour, J.P. Rothstein, Dynamic contact angle measurements on superhydrophobic surfaces, Physics of Fluids, 27 (2015).

[120] D. Quere, Non-sticking drops, Reports on Progress in Physics, 68 (2005) 2495-2532.

[121] B.J. Rosenberg, T.V. Buren, M.K. Fu, A.J. Smits, Turbulent drag reduction over air- and liquid-impregnated surfaces, Physics of Fluids, 28 (2016) 015103.

[122] C. Hao, J. Li, Y. Liu, X. Zhou, Y. Liu, R. Liu, L. Che, W. Zhou, D. Sun, L. Li, L. Xu, Z. Wang, Superhydrophobic-like tunable droplet bouncing on slippery liquid interfaces, Nature Communication, 6 (2015).

[123] J.-H. Kim, J.P. Rothstein, Delayed lubricant depletion on liquid-infused randomly rough surfaces, Experiments in Fluids, 57 (2016) 81.

[124] M. Pasandideh-Fard, Y.M. Qiao, S. Chandra, J. Mostaghimi, Capillary effects during droplet impact on a solid surface, Physics of Fluids, 8 (1996) 650-659.

[125] C. Clanet, C. Beguin, D. Richard, D. Quere, Maximal deformation of an impacting drop, Journal of Fluid Mechanics, 517 (2004) 199-208.

[126] I.S. Bayer, C.M. Megaridis, Contact angle dynamics in droplets impacting on flat surfaces with different wetting characteristics, Journal of Fluid Mechanics, 558 (2006) 415-449.

[127] J.-H. Kim, J.P. Rothstein, Dynamic contact angle measurements of viscoelastic fluids, Journal of Non-Newtonian Fluid Mechanics, 225 (2015) 54-61.

[128] J.-H. Kim, J.P. Rothstein, Role of interface shape on the laminar flow through an array of superhydrophobic pillars, In preparation.

[129] J.-H. Kim, J.P. Rothstein, Droplet impact dynamics on lubricant-infused superhydrophobic surfaces: The role of viscosity ratio, Langmuir, (In revision).